The Investigation of an Inboard-Winglet Application to a Roadable Aircraft

Nanyaporn Intaratep

Thesis submitted to the Faculty of the
Virginia Polytechnic Institute and State University
In partial fulfillment of the requirements for the degree of

Master of Science In Aerospace Engineering

James F. Marchman, III, Chair
William J. Devenport
Joseph A. Schetz

May 31, 2002
Blacksburg, Virginia

Keywords: Inboard winglet, Propeller-induced flow, Roadable aircraft, Aerodynamics, Conceptual design

The Investigation of an Inboard-Winglet Application to a Roadable Aircraft

Nanyaporn Intaratep

(Abstract)

The inboard-winglet concept was examined for its flow characteristics by testing for pressure coefficients over the wing and winglet surface in the Virginia Tech Stability Wind Tunnel over a range of freestream velocity and angle of attack. The results were analytically applied to calculate aircraft performance of a roadable aircraft, Pegasus II, which used the inboard-winglet concept in its design. The results proved that this concept has the potential to increase a wing lift coefficient at the right combination of thrust setting and freestream velocity better than a conventional wing-propeller arrangement. The lift coefficient inside the winglet channel was approximated as 2D in behavior. It is also shown that the winglets produce thrust at a positive-lift wing configuration. In the Pegasus II, the vertical stabilizers act like inboard winglets and produce a thrust component from its resultant force, giving 5.2% improvement in its effective aspect ratio and resulting in an induced-drag decrease. With an application of the new wing concept, the Pegasus II performance is comparable to other general aviation aircraft.

Acknowledgement

This work was partially supported by NASA Langley Research Center, Personal Air Vehicle Evaluation Project, through NASA Grant NAG-1-001100.

The author greatly appreciates a precious guidance, support and patient from Dr. James F. Marchman, III during these 2 years. Very special thanks to mother and friends.

Table of Contents

List of Figures

List of Tables

Nomenclature

A	Propeller disk area (ft^2)
AR	Geometric aspect ratio
AR_e	Effective aspect ratio
b	Wing span (ft)
b	Y-intercept
c	Chord length
c_p	Specific fuel consumption (lb/(hp.hr))
C_a	Section axial force coefficient
C_d	Section drag coefficient
C_{D0}	Parasite drag coefficient
$C_{D,mp}$	Drag coefficient at minimum power
C_l	Section lift coefficient
C_{l_α}	Section lift curve slop (per radian)
C_L^*	Power-off lift coefficient
$C_{L,A}$	Approached lift coefficient
$C_{L\max}$	Maximum lift coefficient
$C_{L\max,i}$	Inboard maximum lift coefficient
$C_{L\max,o}$	Outboard maximum lift coefficient
$C_{L,mp}$	Lift coefficient at minimum power
$C_{L,TO}$	Takeoff lift coefficient
C_n	Normal force coefficient
$C_{p,l}$	Lower-surface pressure coefficient
$C_{p,u}$	Upper-surface pressure coefficient
d	Section drag

d	Fuselage width (ft)
D	Drag (lbs)
e	Oswald efficiency factor
E	Endurance (hrs)
F	Fuselage lift factor, $F = 1.07\left(1+\frac{d}{b}\right)^2$
g	Acceleration of gravity (ft/s^2)
h_{cr}	Cruise altitude (ft)
h_{SL}	Sea level altitude (ft)
h_{TR}	Transition altitude (ft)
K	Induce drag factor
K'	Correction for non-linear effects
l	Section lift
L	Lift (lbs)
(L/D)	Lift to drag ratio at climb angle
m	Slope
M_{ff}	Ratio of takeoff gross weight to empty weight
n_{FL}	Flare load factor
N_n	Nose-gear normal force (lbs)
P_A	Power available (ft.lb/s)
P_R	Power require (ft.lb/s)
r	Distance from a vortex center
R	Range (mph)
R_{FL}	Flare radius (rad)
R_{TR}	Transition radius (rad)
$RoC_{\max}$	Max rate of climb (fpm)
S	Wing area (ft^2)
S_{CL}	Climb takeoff distance (ft)

$S_{\exp}$	Exposed wing area (ft^2)
S_i	Inboard wing area (ft^2)
S_{LA}	Landing air distance (ft)
S_{LR}	Rotation landing distance (ft)
S_{LNGR}	Nose-wheel-ground-run landing distance (ft)
S_{NGR}	Nose-wheel-ground-run takeoff distance (ft)
S_o	Outboard wing area (ft^2)
S_R	Rotation takeoff distance (ft)
S_{TR}	Transition takeoff distance (ft)
t	Section thrust
T	Thrust (lbs)
T_c	Thrust coefficient
$TOGW$	Takeoff gross weight (lbs)
v	Induced velocity
v_w	Spanwise velocity
V	Freestream velocity
$V(r)$	Relative velocity
V_A	Approached velocity (mph)
V_{CL}	Climb velocity (mph)
V_{FL}	Flare velocity (ft/s)
V_{mp}	Velocity at minimum power (mph)
V_s	Stall velocity (ft/s)
V_{TD}	Touch down velocity (ft/s)
V_{TO}	Takeoff velocity (ft/s)
V_∞	Freestream velocity
W_f	Required fuel weight (lbs)
$W_{f,actual}$	Actual-used fuel weight (lbs)

$W_{fi1,2...8}$	Fuel fraction of each phase (final/initial)
α	Angle of attack
$\alpha(r)$	Angle between relative velocity and freestream velocity
$\alpha_l(r)$	Relative angle of attack
α_{0L}	Zero-lift angle of attack
α_{stall}	3-D stall angle of attack
β	$\sqrt{1-M^2}$
$\gamma(r)$	Twist angle
γ_A	Flare angle (rad)
Γ	Circulation
δ	Uncertainty
δ_f	Flap deflected angle (deg)
$\Delta C_{l\max}$	Change in $C_{l\max}$ with δ_f flap deflection
Δy	Leading edges shape parameter
η	Lower-surface lift fraction
η	$\frac{dC_l}{d\alpha}\frac{\beta}{2\pi}$, $\frac{dC_l}{d\alpha}$ = 2-D lift curve slope
η_p	Propeller efficiency
θ_{CL}	Climb angle (rad)
Λ_t	Sweep of wing at maximum thickness (deg)
μ	Ground fiction coefficient
μ_{break}	Ground fiction coefficient with break
ρ	Density (slug/ft^3)
ρ_∞	Freestream density
σ	Density ratio (relative to density at sea level)

Chapter 1

Introduction

There is a demand for a more convenient solution to the problem people now face in commercial air travel. For many decades, various combinations of air and ground vehicles by many enthusiastic inventors have been proposed and put into use by the public but problems still exist. Currently, so-called roadable aircraft, flying car, or dual-mode vehicles are being seriously discussed as one alternative of personal air vehicles that is suitable to middle range travel needs. These can provide a faster choice for travelers when compared to commercial airline services, since their door-to-door travel capability can eliminate the time usually wasted at congested hub airports. A capability for short takeoff and landing (STOL) in the vehicle provides more options, giving an opportunity for it to operate in small private airports instead of crowded regional airports. However, the competing demand of automobile and aircraft design cause problems in a conventional design aspect, requiring an application of adapted technologies.

A notable limitation of the roadable aircraft design is the wingspan. For an automobile, a width restriction is officially provided in highway regulations such as the DOT in the United States and UK Construction and Use Regulations in the United Kingdom. To fit airplane-like vehicles into highway width, their wings must either have a very low aspect ratio, or must be capable of folding, retracting, or detaching in some way. Accordingly, wing planforms of these vehicles usually have limited wing area and/or low aspect ratio, causing a high lift constraint and severe induced drag penalty to the vehicles. Thus, it is necessary for them to employ lift augmentation and drag deduction techniques for requirements in their takeoff and landing performance.

One of interesting STOL concepts, the Custer channel wing (Figure 1.1), was developed as a power-augmented lift device when a propeller near a trailing edge induces a circulation around a wing giving an increase in its lift coefficient. The concept works best at a static condition while its potential decreases as a freestream velocity increases. Therefore

it is an appropriate choice for short takeoff performance because of a very low speed at that condition and there is no need for addition moving parts, apart from the propeller. Nevertheless, there are problems with the concept in its landing ability and construction complexity.

Modified from the STOL Custer Channel Wing concept, an inboard-winglet concept was initially presented in a design of a roadable aircraft, named Pegasus (Figure 1.2), as a part of its inboard box-wing concept. Vertical structures on a wing upper surface (vertical stabilizers in the Pegasus), working similar to winglets yet located inboard, along side of a propeller, integrate with a wing to form a rectangular channel with the high-mounting pusher propeller at its trailing edge. Resembling a circular channel, this rectangular one produces power-augmented lift when the propeller induces a flow between them. Moreover, the winglets have a potential to generate an additional forward force component, thrust, using the energy, generated by strong vortices at the junctions between the inboard and outboard sections of the wing. The inboard winglet concept is also less complicated in construction than the channel wing.

By examining spanwise and chordwise pressure distributions over the wing and winglet surfaces of a wind tunnel testing model, the research was focused on flow characteristics of the inboard-winglet wing concept to understand its behavior at various speeds and angles of attack. Experimental results were used to evaluate an application of the concept to the modified version of the Pegasus roadable aircraft, Pegasus II. Its estimated performance was compared to 3 other general aviation aircraft, both single and dual mode vehicles, to study its advantages and disadvantages and the sensitivity of the concept based on the creditability of existing designs.

This investigation should provide a better understanding in the inboard-winglet concept and its application to the roadable aircraft. It also indicates possible study areas for further research.

Figure 1.1 The Custer Channel Wing concept

Figure 1.2 View of the Pegasus in flight (Gassler, et.al, 2000)

Chapter 2

Literature Review

2.1 Roadable Aircraft History

Starting as early as the development of the Wright Flyer, the idea of creating a multi-purposed aircraft spread among ambitious inventors. Often, in today s crowded traffic situations, drivers wish to grow wings on their cars and save time by flying to their destination. On the other hand, pilots stuck at the airport because of weather conditions wish that they could drive their airplanes on a road. To a certain degree, the merging of aircraft and automobile has always been a challenging aspiration in general aviation. Even Henry Ford once said in 1940, Mark my word: A combination airplane and motor car is coming. You may smile. But it will come (LeCompte, 1999).

In 1945, inspired by a difficult personal experience, Robert Fulton Jr. flied a patent for the prototype of a 2-seated flying car, *Airphibian*. Its configuration in the flying mode resembled a regular general aviation aircraft but with a different landing gear design. It had 4 wheels instead of typical 3. On the ground the wing and empennage assembly and the propeller were detached, leaving only what was similar to a small city car. The conversion time from plane to car mode was only 5 minutes. It employed steering wheel and pedals for control in both flying and driving mode. The pedals controlled the rudders during flight and became clutch and brake in the driving mode. The cruise performance was 50 miles per hour on the road and 120 miles per hour in the sky. With years of development and more than 100,000 miles logged, Fulton s design was the first combined aircraft and automobile vehicle certified for production by FAA in 1950. Figure 2.1 shows an advertising poster for the *Airphibian* when Fulton s company started a production process for it. Nevertheless, the company was shut down due to financial problems.

Figure 2.1 Airphibian as in flying and roadable configurations (LeCompte, 1999)

Another roadable aircraft certified by the FAA was Moulton Taylor s *Aerocar*. Created in 1959, Taylor formed his idea after seeing Fulton s impressive *Airphibian* transformed to a car and driven off, unable to carry its wing and tail members with it. His design solved Fulton s problem by constituting the demounted flight components as a trailer towed behind the car. The drawings in flying and roadable mode are shown in Figure 2.2. The tail portion is connected to the vehicle body with an upward slope. Also, the propeller and thrust axis is inclined. These creations enable the rear wheels to serve as the landing wheels. Thus he applied the concept of a front wheel drive system, rarely used at that time, to the design. Unconnected high wings secure to a fuselage by latch elements and have a supporting strut connected to the tail portion. Besides the front-wheel drive system, another innovative approach found in Taylor s *Aerocar* was the use of fiberglass composite material for the vehicle s surface. Attracting considerable commercial interest, Taylor s design was considered to be the most reasonable roadable aircraft design of its time.

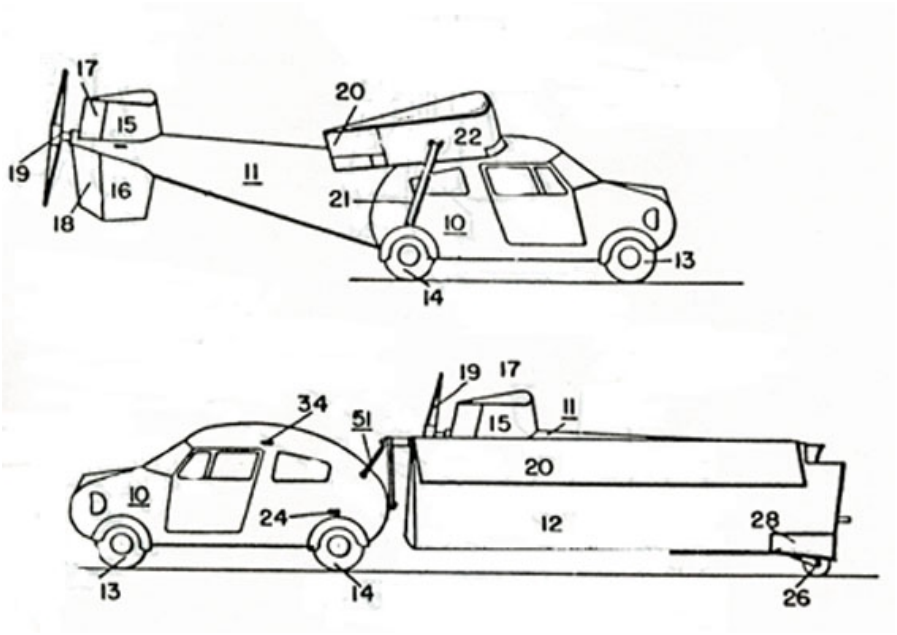

Figure 2.2 Drawing of Aerocar as in flying and roadable configurations (Stiles, 1994)

Stiles mentioned that up to 1994, there were more than 70 patents for roadable aircraft concepts in the United States alone (Stiles, 1994). They varied from sophisticated designs to homebuilt, from car-like to airplane-like, and from propeller-driven to jet propulsion. It is undoubtedly still debatable among roadable aircraft inventors which approach would provide the most beneficial solution for the design. However, with recent advances in technology, the solutions to the roadable aircraft problem, without having to detach and stow the wing, should be closer at hand.

2.2 Wing Design for Roadable Aircraft

When considering a conventional-type of roadable aircraft, a notable complexity in transforming an airplane to a car occurs from dimension restrictions. To provide an optimal use on ground, the vehicle must fit in a standard public road and parking space. This issue raises a concern for the wing design of the roadable aircraft since the shorter the wing span,

the poorer the aerodynamic characteristics. In earlier years, designs favored demounting an automobile body and a flight assembly as represented in Fulton s *Airphibian* and Taylor s *Aerocar*. The wings were fundamentally designed in a conventional way, with joints and mechanisms to attach it to the body and break it apart for stowage. There was also an idea of using composite material structures to keep weight down, providing a conveniently manual conversion from the automotive vehicles to the fixed-wing aircrafts. Since the wing designs were not limited by a span restriction, there would rarely be disadvantages in the aerodynamic characteristics of the designs.

In later development, more complicated designs were effectively presented as a result of advanced technologies and increasing human factor concerns. They mostly gave up the original demounting concept. Flight components (wings, tails, etc.) have been eliminated or designed to stow within the vehicle body in a driving mode for both appearance and user convenience. Solutions to the wing span restriction varied depending on performance requirements in a design. Sahr (Stiles, 1994) introduced the telescoping wing concept when he filed a patent for his roadable aircraft, Advanced Flying Automobile (AFA), in 1988. Figure 2.3 shows the components of his wing design that are able to extend and retract telescopically with 6 short wing segments per wing. Between the wings is a central housing separated into halves for stowing each side of the retracted segments. Front and rear tubular spars are divided into 6 alternate fixed and rotatable sections corresponding to the wing segments with the rotatable one at the root. The inner one overlaps the outer one for telescoping purposes. Having ball bearings between overlap portions and rotatable sections provides control of the extension or retraction direction. The wing extended span is 28.9 ft^2, giving a reasonable aspect ratio of 5.9. The central housing is placed on the top of the cabin. A finite element structural analysis of the preliminary design, a functionality test of a half scale model and performance estimations when applying the concept to the AFA established the possibility of designing a roadable aircraft with this concept. However, it may be advisable to consider a further study on structure integrity. (Czajkowski, et.al., 1997)

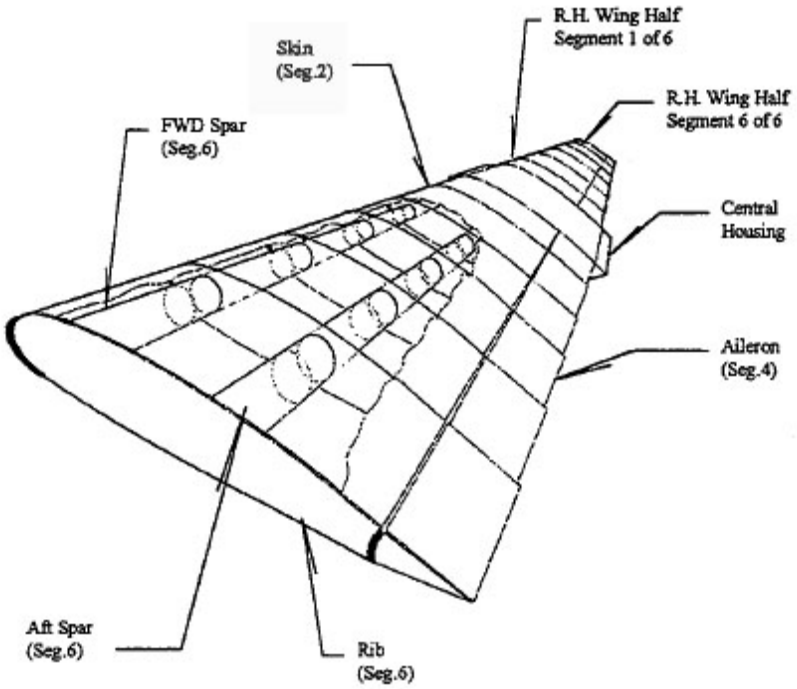

Figure 2.3 Telescopic wing in extended configuration (Czajkowski, et al., 1997)

Another approach for wing stowage with presumably fewer structure integrity problems is a folding wing design. Developed by Aeromaster Innovation Inc. in 1993, Synergy is a roadable aircraft with cockpit-actuated wing folding as shown in Figure 2.4. The preliminary design shows that a conversion can be completed hydraulically in seconds. For the wing conversion, each side of the wing is longitudinally pitched up to unlock, then folded forward to a position that places the wing planforms parallel to the vehicle sides. In driving mode, the wing position was designed for clear visibility for the driver. The planform stays far enough away from the vehicle body for users to comfortably enter it while still giving a practical roadable width of 7.5 ft. Performance estimations with this 28.7 ft wing span and 7.83 aspect ratio provided impressive results.

Another folding wing concept was found in the design of the LaBiche Aerospace, FSC-1 vehicle. With a wing span of 32.13 ft, the two sides of the wing are folded in half and stowed in the compartment underneath the cabin when the vehicle is on the ground. The design also has a canard, working as a control and lifting surface to improve aerodynamic

capabilities of the vehicle. The canard is retracted into the compartment in front of the passenger cabin. Therefore the span and planform of both wing and canard are restricted by the vehicle s dimensions. Since the takeoff gross weight of the FSC-1 is approximately 3600 lbs, the vehicle has a stall speed higher than the 61 knots FAR requirements. Thus the restriction in wing area could cause some problems for the aircraft performance. Figure 2.5 shows the wing folding of the FSC-1.

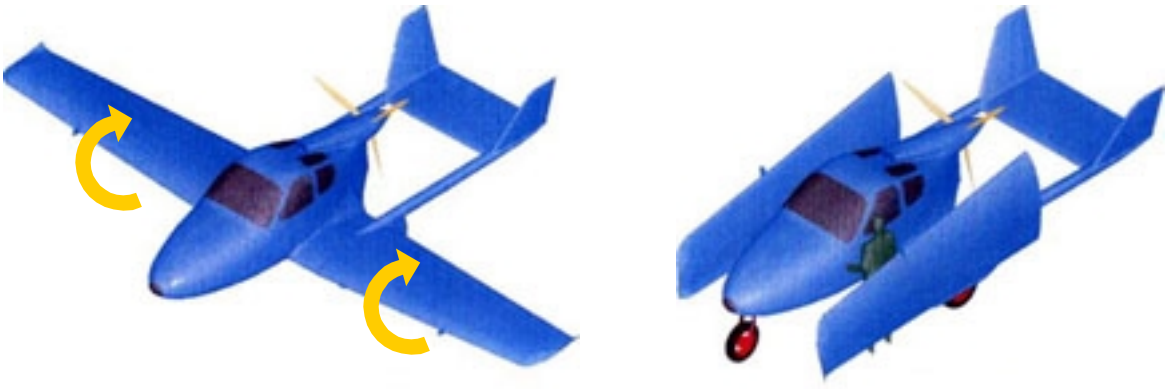

a) Flying mode b) Driving mode

Figure 2.4 Synergy configuration in flying and driving mode

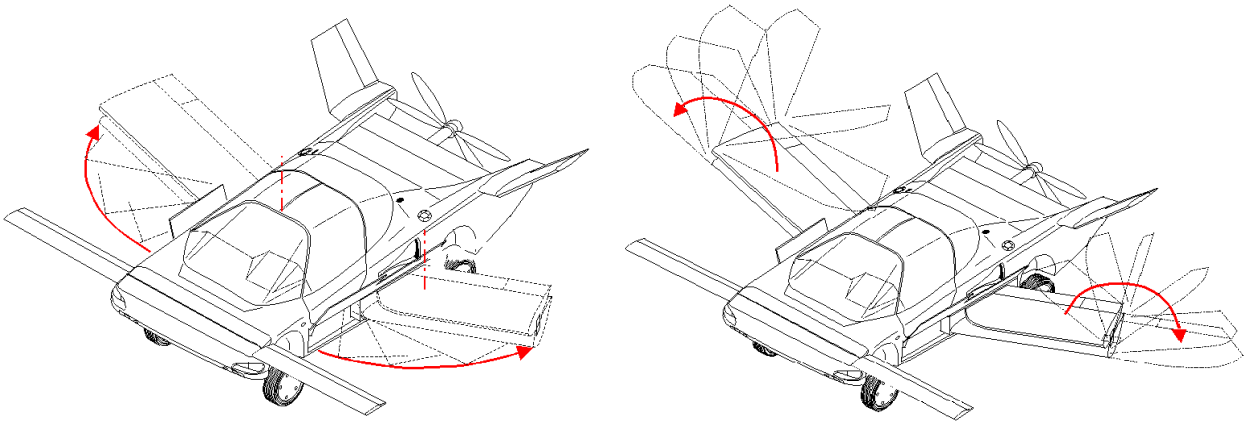

Figure 2.5 FSC-1 wing folding approach

2.3 Channel Wing Concept

Modified to be an inboard-winglet wing concept in this investigation, the Custer channel wing concept was developed and flight tested in an twin-engine experimental airplane, CCW-1, by William Custer in 1942 (Blick, 1988). The Custer channel wing as shown in Figure 2.6 is a conventional, rectangular, straight wing with a half-cylindrical duct shaped around a pusher propeller. Locating near the rear of the wing, the propeller induces a flow velocity over wing upper surface creating a change in pressure distribution on the surface. The result is a possible power augmented lift device for STOL performance due to its high lift potential in the low speed region.

This concept gained sufficient interest from the NACA and the military for them to conduct some experiments in the 1940 s and 1950 s. Young (1944) concluded from the test for the lift measurement of 1/3-scale powered model of Custer channel wing in the Five-Foot Wind Tunnel, that an increase in channel lift coefficient, ΔC_L, varies linearly with thrust coefficient, T_c, indicating the same characteristic as found in conventional wing-propeller arrangements. However, the channel wing concept tended to provide a more effective lift increment as a result of a ducting effect on the propeller inflow and propeller tip vortices. Young (1947) later conducted wind tunnel tests for a series of various Custer channel wing configurations. By having 2 different channel lengths, 43 and 17.5 inches, the tests indicated that the short channel is preferred to the long channel because of the greater potential in thrust and lift. For a study by the NACA, the Custer channel wing airplane model was tested in the Langley Full-Scaled Wind Tunnel, examining the lift characteristics at static conditions. According to Pasamanick (1953), the resultant force on the model, equaling to 88 percent of static thrust and having 23-degree upward inclination to the propeller axis, could manage to lift an airplane that has a weight magnitude less than the force and climb at an angle higher than 67 degree with certain tail configuration.

It was not until 1980 s that a theoretical prediction of Custer s channel wing lift and drag coefficient was presented. Blick (1988) assumed that the entire power-on lift of the channel wing is a combination of the upper surface lift due to propeller-induced flow with no ducted effect, the lower surface lift at freestream conditions, the flat plate lift from the induced flow, the planar wing portion of lift without the propeller effect and the lift due to

vectored thrust. The drag coefficient is estimated by adding a channel induced drag, caused by extra lift in the channel, to the drag polar. The experimental data showed a fair correlation to the theory with slight underestimation. It also demonstrated another benefit of the channel wing; that it is likely to stall at a higher angle of attack than a conventional wing.

Gunther s (1998) application of the modified Blick theory for comparison with the wind tunnel lift coefficient data for a 3 feet span channel wing model indicated that the prediction did not match the experimental data very well. This is possibly caused by poor lift coefficient data using in the prediction. The power-off channel wing barely produced the predicted pressure distribution until it reached large angles of attack. With the propeller, the chordwise pressure distribution inside the channel decreased as the power increased. The overall spanwise pressure distribution decreased as well. This showed the effect of the channel propeller to the planar portion of the wing. Grissom and Henry (2000) conducted later experiments on aerodynamic characteristics of a channel wing model and a modified channel wing model consisting of an inboard-winglet wing, or the scoop wing. With the power on, the channel wing could gain a lift to drag ratio nearly as good as the 2-D wing while the inboard-winglet wing could reach slightly lower values. However, an attempt to decrease a gap between the winglet and the propeller tips by creating fillets proved to produce excessive drag, reducing the lift to drag ratio.

Figure 2.6 Custer CCW-5 prototype at the Mid Atlantic Air Museum (Scott, 2002)

Chapter 3

Experimental and Theoretical Techniques

3.1 Wind Tunnel Testing

Wind tunnel testing of the inboard-winglet concept helps provide further insight into characteristics of flow induced by a pusher propeller in a winglet channel. This experiment demonstrated the concept by using a simplified wing-model. Measurements of pressure patterns inside the channel were made rather than measurements of aerodynamic coefficients. Pressure distributions over the wing upper-surface and winglet surface were observed and compared to an identical wing model without inboard winglets. To evaluate the influence of the propeller, the test was divided into 2 stages, with and without propeller-induced flow. Tests were conducted in the Virginia Tech Stability Wind Tunnel to acquire pressure distribution measurements, using a scannivalve system, for diverse freestream velocities and angles of attack. The details of the equipment, needed facilities, and procedure are described below.

3.1.1 Pressure Model

This model, initially constructed at Kasatsart University, is an assembly of several aluminum sub-components with the surface formed as the required wing shapes (Figure 3.1). For the purpose of the experiment it can be combined into 2 configurations, a conventional plain wing and an inboard-winglet wing. In the former, the core section of the model is a 30 x 10 inches straight rectangular wing. An NACA0012 airfoil is the chosen wing cross-section for straightforward analysis since it cancels any unsymmetrical effect generally present in cambered airfoils and provides good flow quality at low speed. The airfoil section drawing and coordinates are shown in Figure 3.2 and Table 2.1, respectively.

The latter configuration is a combination of the main wing and 2 winglets. Two 10 inch-span winglets, with NACA0012 airfoil section, are mounted to the upper surface of the wing next to either side of propeller blade location, or 10 inches apart measured at winglet trailing edges, with a 5-degree diverging angle from the propeller centerline. This angle helps enhance the thrust to suppress additional drag causing by the extra structures as concluded by Grissom and Henry (Grissom and Henry, 2000). The aspect ratios of the main wing and inboard-winglet section are 3 and 1 respectively. For the mounting of the model to the tunnel turntable, a steel bar with rod-end was attached along the spanwise centerline on the bottom section of the model and adjusted as its leading edge was perpendicular to the freestream velocity (Figure 3.3).

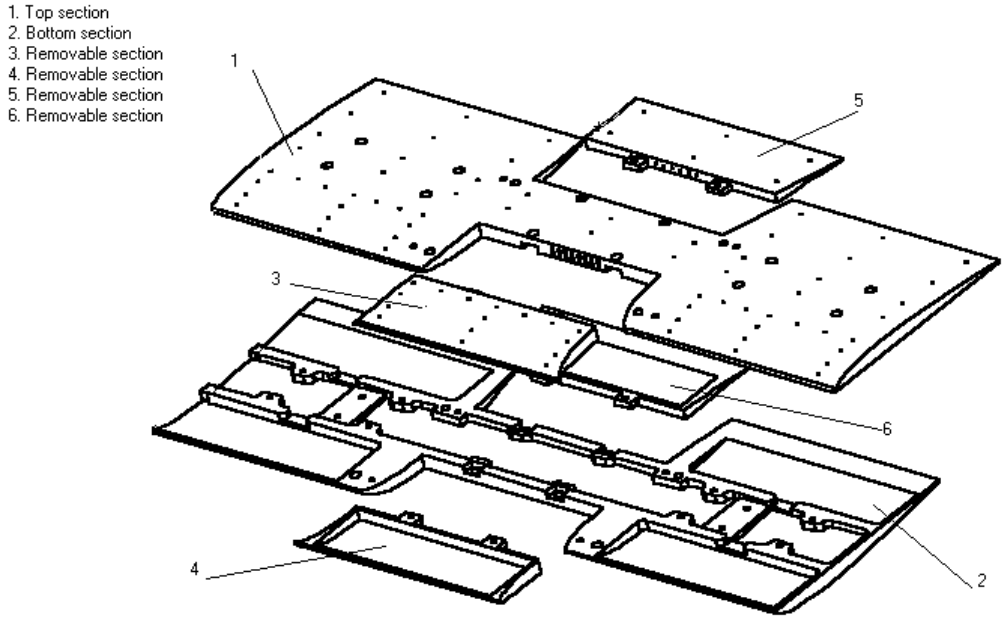

a) Main wing components

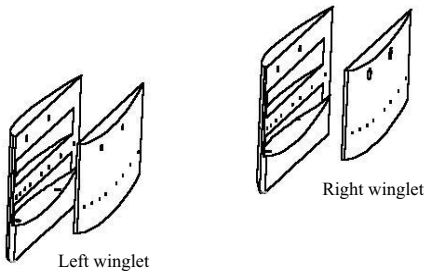

b) Winglet components (left and right)

Figure 3.1 Disassembly of pressure model of inboard-winglet concept (Durongphant, et.al., 2001)

Table 3.1 NACA0012 airfoil section coordinates (Jacobs, 1933)

x/c (%)	y/c (upper)	y/c (lower)
0	0	0
1.25	1.894	-1.894
2.5	2.615	-2.615
5	3.555	-3.555
7.5	4.200	-4.200
10	4.683	-4.683
15	5.345	-5.345
20	5.737	-5.737
25	5.941	-5.941
30	6.002	-6.002
40	5.803	-5.803
50	5.294	-5.294
60	4.563	-4.563
70	3.664	-3.664
80	2.623	-2.623
90	1.448	-1.448
95	0.807	-0.807
100	0.126	-0.126
L.E Rad: 1.58		

Figure 3.2 NACA0012 airfoil section

Figure 3.3 The pressure model in the wind tunnel

To analyze the flow characteristics induced by the propeller, 100 pressure taps were placed inside the upper surface of the wing and both sides of the winglets. Nine spanwise stations of 8 pressure taps were arranged chordwise over the 3 sections of the wing, 2 outboard wing sections and a section between winglets. Extra taps were added at the quarter chord to obtain a total of 15 spanwise taps for a more detailed observation. By mounting a set of pressure taps inside inner and outer surface of the winglets the pressure distribution due to flow around them could be investigated to determine the flow pattern caused by these extra structures. Copper and rubber capillary tubes were used for connecting surface pressure orifices to the scannivalve system. These were carefully laid inside slots machined between the top and bottom section to avoid blocking the tubes. Figure 3.4 shows dimension diagrams of the models and their pressure tap arrangement and Table 3.2 and 3.3 show measurement locations of each taps. The arrangements vary for each model as a result of the need to make the best use of limited scannivalve ports. The location used in the conventional wing were limited to those needed to compare this wing to the inboard-winglet concept, therefore fewer pressure taps were required.

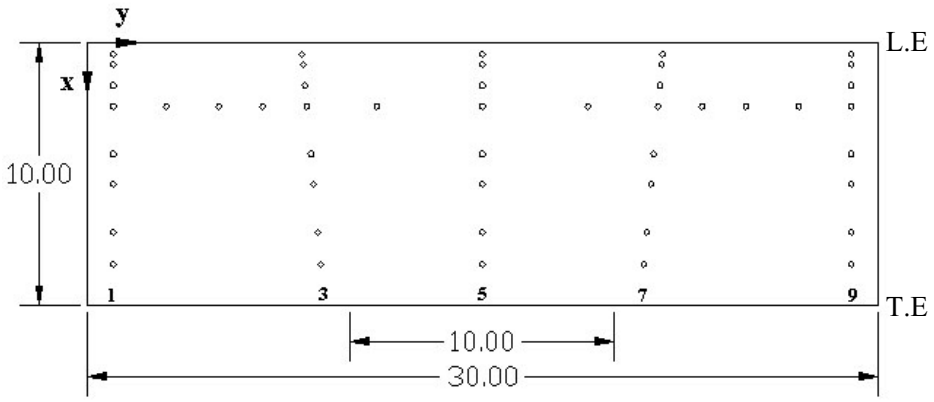

a) Conventional wing pressure taps

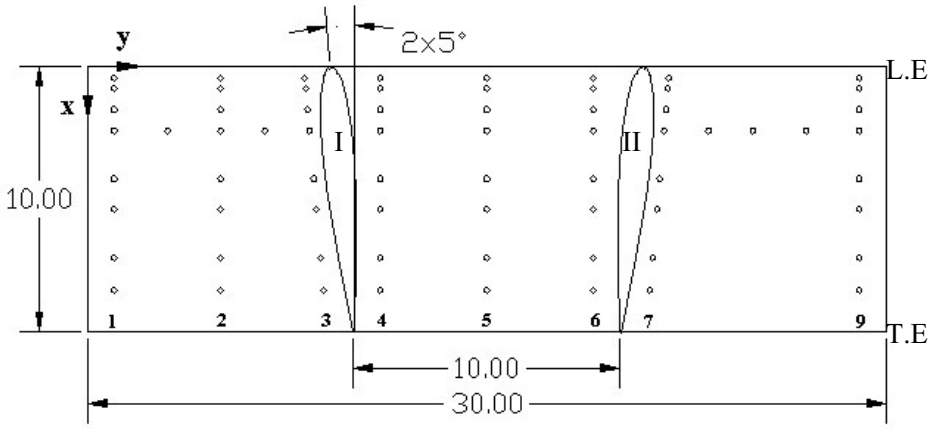

b) Inboard-winglet wing pressure taps

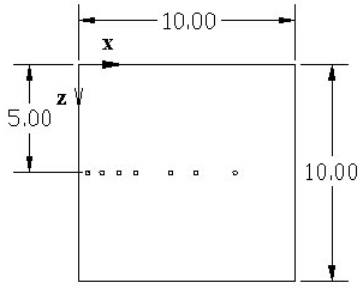

c) Winglet pressure taps

Figure 3.4 Pressure taps location and dimensions for various models

Table 3.2 Locations of chordwise pressure taps

Column	y/b	x/c							
		Pressure tap number							
		1	2	3	4	5	6	7	8
1	0.0333	0.0474	0.0844	0.1645	0.2447	0.4250	0.5403	0.7220	0.8450
2	0.1667	0.0474	0.0844	0.1645	0.2447	0.4250	0.5403	0.7220	0.8450
3	0.2780	0.0474	0.0844	0.1645	0.2447	0.4250	0.5403	0.7220	0.8450
4	0.3667	0.0474	0.0844	0.1645	0.2447	0.4250	0.5403	0.7220	0.8450
5	0.5000	0.0474	0.0844	0.1645	0.2447	0.4250	0.5403	0.7220	0.8450
6	0.6333	0.0474	0.0844	0.1645	0.2447	0.4250	0.5403	0.7220	0.8450
7	0.7220	0.0474	0.0844	0.1645	0.2447	0.4250	0.5403	0.7220	0.8450
9	0.9667	0.0474	0.0844	0.1645	0.2447	0.4250	0.5403	0.7220	0.8450
Winglet	0.5	0.0433	0.1080	0.1877	0.2642	0.4250	0.5403	0.7220	-

Table 3.3 Locations of spanwise pressure taps

Pressure tap number	x/c	y/c
1	0.2447	0.0333
2	0.2447	0.1000
3	0.2447	0.1667
4	0.2447	0.2223
5	0.2447	0.2780
6	0.2447	0.3667
7	0.2447	0.5000
8	0.2447	0.6333
9	0.2447	0.7220
10	0.2447	0.7777
11	0.2447	0.9000
12	0.2447	0.9667

3.1.2 Propeller and Drive System

According to the literature review, an essential advantage of the inboard-winglet concept is a utilization of the propeller to accelerate flow over the wing upper-surface giving

a higher lift coefficient. To investigate this issue, a simulation of propeller-induced flow inside the channel was accomplished by mounting an APC pusher propeller of 10-inch diameter and 7 pitches over the wing upper-surface. As shown in Figure 5, the propeller is directly driven by an Astro-40 Cobalt Motor wired to a variable DC power supply outside the wind tunnel. The power input is 8.5 amps for all velocity conditions as a result of the assumption that a constant power input provides a fairly constant thrust coefficient. To install the propeller and drive system to the model, a support structure, attached to the upper surface of the wing as shown in Figure 3.5, was built from a metal sheet and pipe by the Aerospace and Ocean Engineering Shop. A drawing of it is shown in Figure 3.6. It can be moved back and forth by screw slots at its base to adjust the chordwise position of the propeller. The best position of the propeller is when a gap between the blade tip and the model structure was minimized in order to reduce the effect of blade tip vortex for good flow quality inside the channel. Thus, in this experiment, the only setting position need is at the trailing edge of the wing. The hub-center lies at the same level as the winglets tip making the propeller half-shrouded. The base of the support could be bent to fit an airfoil curve to control excessive increase in drag. In addition, modeling clay was applied at sharp corners, edges or screw slots to produce a more streamlined channel contour.

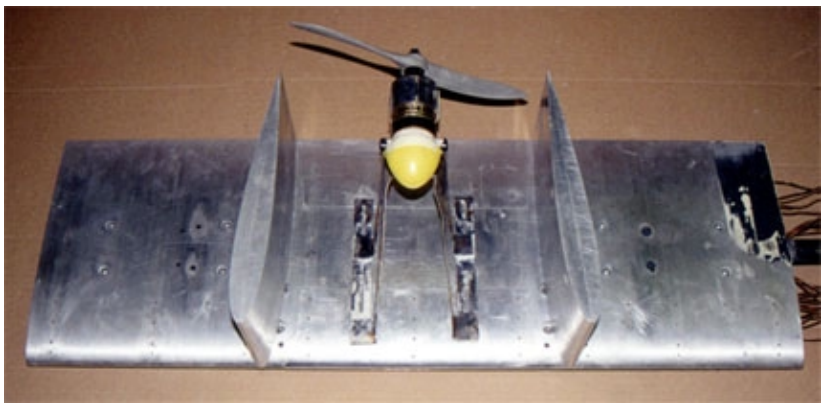

Figure 3.5 Propeller mounting inside the channel

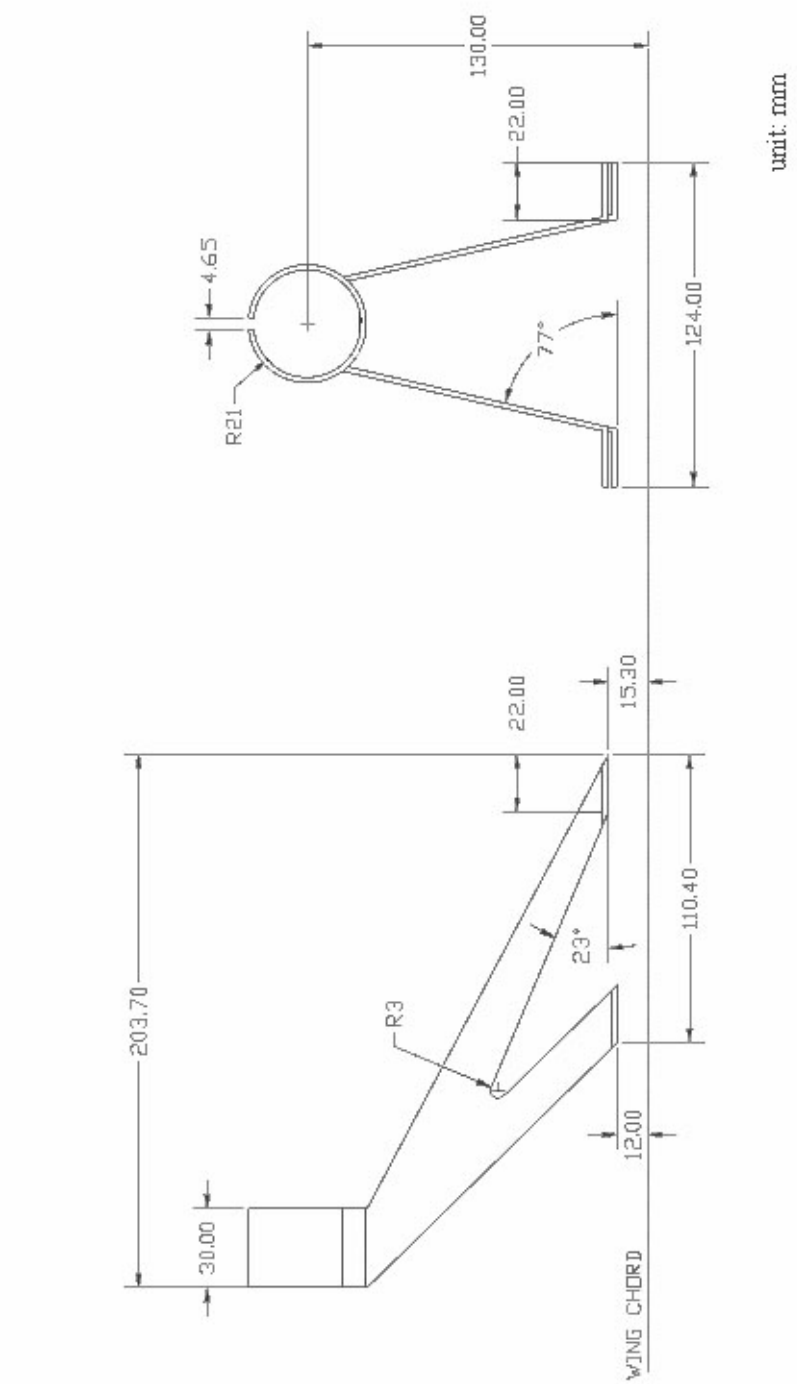

Figure 3.6 Drawing of a motor-support structure

3.1.3 Scannivalve System

A scannivalve system, consisting of an electromagnetic scanning system, 2 pressure transducers and a data acquisition system, was used to measure the pressure coefficient over the model s surface. The scannivalve CTLR2P/S2-S6 Scannivalve Corp can obtain data from 48 pressure taps with one sensor; however it is able to measure only one tap at a time. It was set to collect 2 kilosamples with the frequency of 1,000 Hz and then a stepping motor would switch to the next taps. Each pressure was read after 3 seconds of settling time until all 48 taps data were collected. Measuring pressure in a range from —2.5 to + 2.5 Pa, the first pressure transducer, a Honeywell Model DRAL520GN, was used to measure the difference between a freestream and local static pressure ($\Delta P_{measurement}$). Another sensor, for pressure in a range from 0 to 5 Pa, provided the measurement of dynamic pressure ($\Delta P_{reference}$). From the transducers, data were sent to a data translation DT2801-A A/D converter and an IBM/AT286 computer, which was programmed for data acquisition in QBASIC. The output would show 48 calculated pressure coefficients at corresponding locations with testing conditions. The diagram of the system is sketched in Figure 3.7.

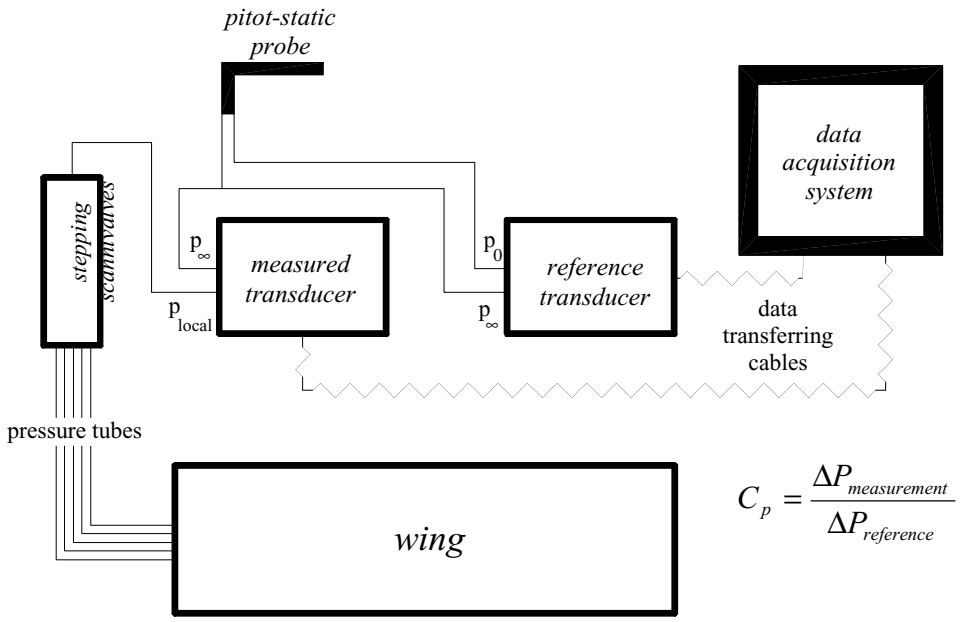

Figure 3.7 Diagram of the scanni valve system

3.1.4 Stability Wind Tunnel

These experiments were performed in the Virginia Tech Stability Wind Tunnel. It is a continuous, closed jet, single return, subsonic wind tunnel with a removable test section of 6 ft x 6 ft cross-section and 24 ft long, which can change to a round test section. Figure 3.8 shows a layout of the wind tunnel. The Plexiglas windows entirely cover one side of the test section that faces a control room. Therefore, it is easily to observe the model and any flow visualization inside from the operator s location. A 600 hp DC motor drives a 14 ft custom-manufactured propeller, giving a maximum speed up to 275 f/s with an approximate Reynolds Number of 1.66 x 10^6 per foot. The flow uniformity is very good as shown in Figure 3.9. The turbulence intensity is extremely low in the test section, in the order of 0.5% or less. The drive system for controlling the speed is a custom design Emerson VIP ES-6600 SCR Drive. A control console is set to vary the speed by reading the dynamic pressure from a Pitot-Static probe upstream of the model location. In the test section, the model support selected in this experiment is the tunnel s motor-driven turntable with a strut. The model was mounted vertically on the strain-gauged strut and rotated on the turntable to vary its angle of attack.

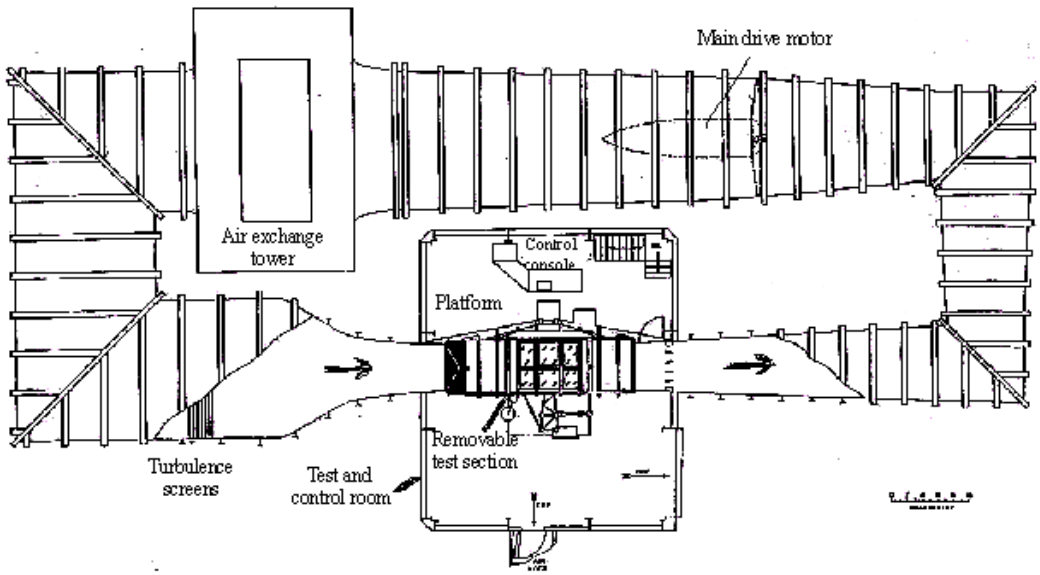

Figure 3.8 General layout of Virginia Tech Stability Wind Tunnel[1]

[1] http://www.aoe.vt.edu/aoe/physical/tunnel_descrip.htm

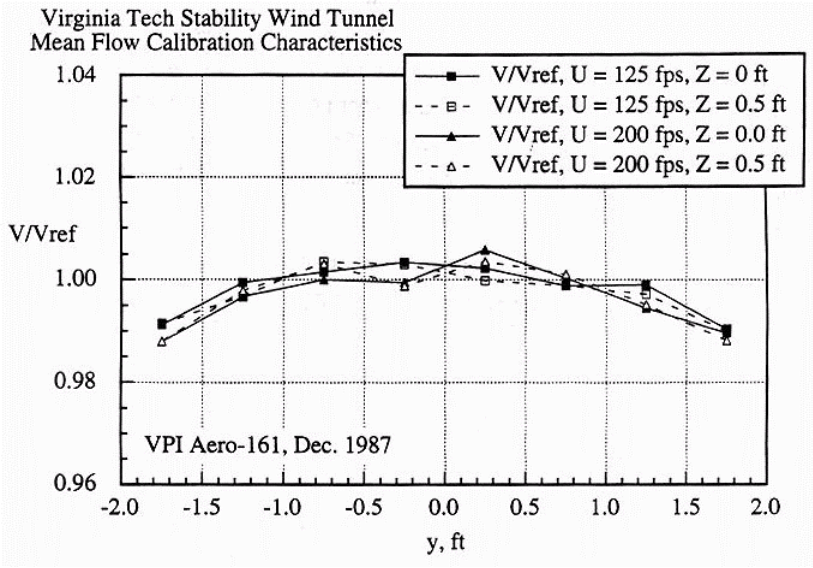

Figure 3.9 Flow characteristics at the model mounting station in the Stability tunnel[2]

3.1.5 Testing Conditions and Procedure

The experiment was conducted during spring and summer of 2001 during two wind tunnel entries, as it was more convenient to construct and prepare the models in this order. The first test used the model with no propeller with both conventional and inboard-winglet configuration to primarily investigate the change in flow characteristic caused by added winglets. In the second test, the wing with an operating propeller was used with constant power input in all test conditions including at zero freestream velocity. This enabled the simulation of induced flow effects. In both sets of tests, pressure distributions were measured on the wing upper surface at 4 angles of attack, -5, 0, 5, and 10 degree. Initially, there was an intention to study higher angles of attack since the results in the previous experiment indicated strange stall behavior (Grissom, 2000). However, the lack of rigidity and strength in the strut of the wing prevented that when the models started vibrating too much at angles of attack higher than 10 degrees when testing prior to a data collection. Additionally, freestream velocity variation, as measured in dynamic pressure of 0.1, 0.7, and 1.2 inches of water (approximate corresponding velocities in m/s and Re are shown in Table

[2] http://www.aoe.vt.edu/aoe/physical/tunnel_descrip.htm

3.4), were also studied to verify that there were no effects of Reynolds Number on the pressure distributions for these configurations. Prior to starting each wind tunnel test, all pressure taps were checked for leaks and blockage by pumping high-pressure air inside each tube. After setting up the model on the turntable inside the tunnel and connecting all instruments, the Scannivalve system was calibrated for accuracy in reading.

Table 3.4 Test velocities and corresponding Reynolds Numbers[3]

Dynamic pressure (in. of water)	Velocity (m/s)	Re
0.2	9.47	145879
0.7	17.71	272811
1.2	23.19	357227

[3] Average density of 1.11202 kg/m^3 and dynamic viscosity of 1.8336 x 10^{-5} kg/m.s

3.2 Resultant Force Approximation of the Experimental Model

Besides giving a physical analysis of flow over the inboard-winglet wing, the pressure coefficients from the experiment also enable a quantitative evaluation of a change in aerodynamic forces acting on the model. This evaluation helps indicate some comparable advantages or disadvantages of the inboard-winglet application better than an only pressure distribution analysis since aircraft performance estimation mostly deals with those forces. Moreover, some predictions, such as an increase in lift coefficient and an additional thrust due to the winglets, can be acquired from the experimental data in order to apply as data input of the Pegasus II s flight performance estimation.

An integration of a pressure distribution over an airfoil chord for both upper and lower surfaces is known to provide normal and axial force acting on an airfoil section when shear stress due to viscous effect is neglected. With x as a chordwise direction and y as a perpendicular one, both normal and axial force integral equations are given respectively as:

$$C_n = \frac{1}{c}\int_0^c (C_{p,l} - C_{p,u})\, dx \tag{3.1}$$

$$C_a = \frac{1}{c}\int_0^c (C_{p,u}\frac{dy_u}{dx} - C_{p,l}\frac{dy_l}{dx})\, dx \tag{3.2}$$

when the notation l is for the lower surface and u is for the upper surface

The known pressure coefficients from the experiment can be calculated for the normal and axial force by using a numerical integration of the above equations in the Trapezoidal approximating forms. Both surfaces are divided into small panels corresponding to a total of gaps between each pressure tap location. When n is a number of panels, the equations can be converted to:

$$C_n = \sum_{i=1}^{n}\left[(C_{p,l,i} - C_{p,u,i})\Delta\left(\frac{x_i}{c}\right)\right] \tag{3.3}$$

$$C_a = \sum_{i=1}^{n}\left[\left(C_{p,u,i}\frac{\Delta y_{u,i}}{\Delta x_i} - C_{p,u,i}\frac{\Delta y_{l,i}}{\Delta x_i}\right)\Delta\left(\frac{x_i}{c}\right)\right] \tag{3.4}$$

From the experimental data, there are 7 and 8 pressure measurement locations along a chord line on both sides of the winglets and the wing upper surface respectively. Figure 3.10 and 3.11 show the surface between each pressure taps was divided as a panel.

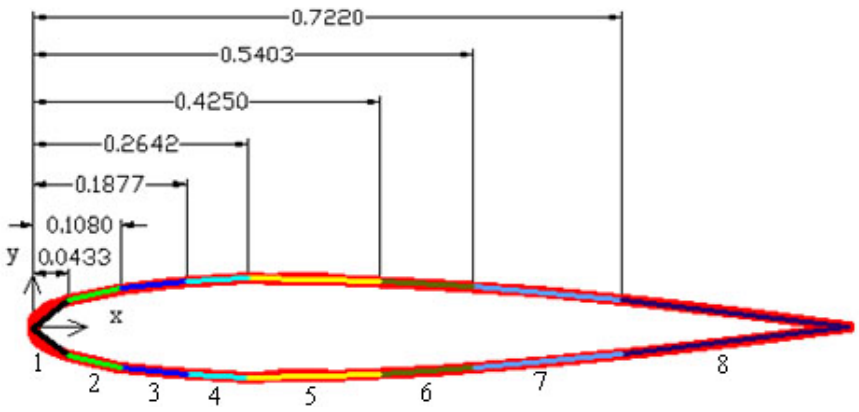

Figure 3.10 Winglet pressure tap positions in x/c and paneling

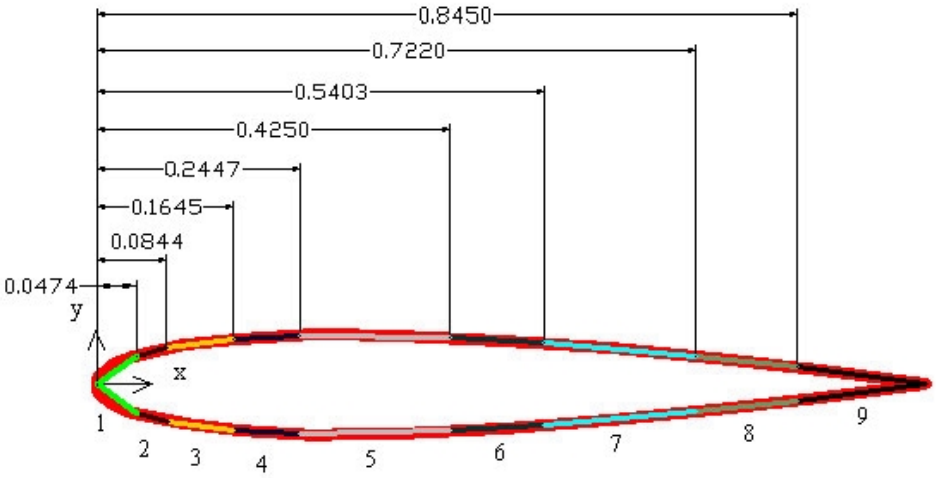

Figure 3.11 Wing pressure tap positions in x/c and paneling

By this arrangement, the experimental data have to be approximated for a finite pressure distribution over each panel since they are located at the panel boundary, using the first-order Lagrange interpolation and linear extrapolation:

$$C_p(x) = \frac{(x - x_1)}{(x_0 - x_1)} C_{p,0} + \frac{(x - x_0)}{(x_1 - x_0)} C_{p,1} \qquad (3.5)$$

The interpolated and extrapolated pressure coefficients would be applied to Eqn (3.3) and (3.4) in order to get the normal and axial force at a section of interest. Lift and drag coefficient can be acquired from:

$$C_d = C_n \sin\alpha + C_a \cos\alpha \tag{3.6}$$

$$C_l = C_n \cos\alpha - C_a \sin\alpha \tag{3.7}$$

A force diagram of Eqn. (3.6) and (3.7) is shown in Figure 3.12. For the section coordinate system of the winglet case, an angle of attack α between the chord line of the section and the freestream velocity is the 5-degree diverging angle. Also, a positive y direction is considered to point to an outboard side of the winglet while the common coordinate system is applied in the wing case.

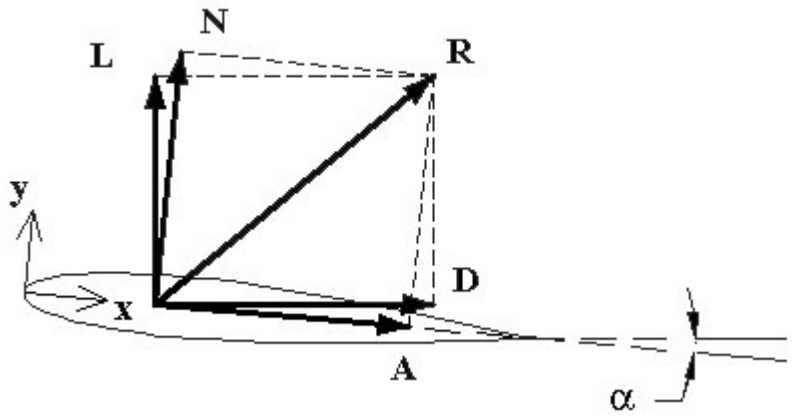

Figure 3.12 Diagram of resultant force component acting a wing section

3.3 Prediction of Lift Coefficient Augmentation from Experimental Data

Since a change in lift of an inboard-winglet wing is a result of induced flow over an upper surface where a propeller is installed, its variation can presumably be a function of thrust. To establish the relation between the input thrust and additional lift of the testing model, the actuator disk concept was applied to find an induced velocity over the wing upper surface. The physical flow passing through the propeller was represented as uniform, incompressible, irrotational flow passing through a thin actuator disk with an infinite number of blades and uniform load. As shown in Figure 3.13, the freestream conditions far in front of the disk are indicated as pressure, p, and velocity, V. The freestream velocity is continuously accelerated giving a velocity $V + v$ at the disk location and $V + v_1$ far behind the disk where static pressure is the same as the freestream condition. The incompressible Bernoulli s equation applies for the location in front and behind the disk; however, it does not cover the flow across the disk due to propeller-input energy causing a step increase pressure, Δp. The thrust is a total of pressure force over the disk area, A.

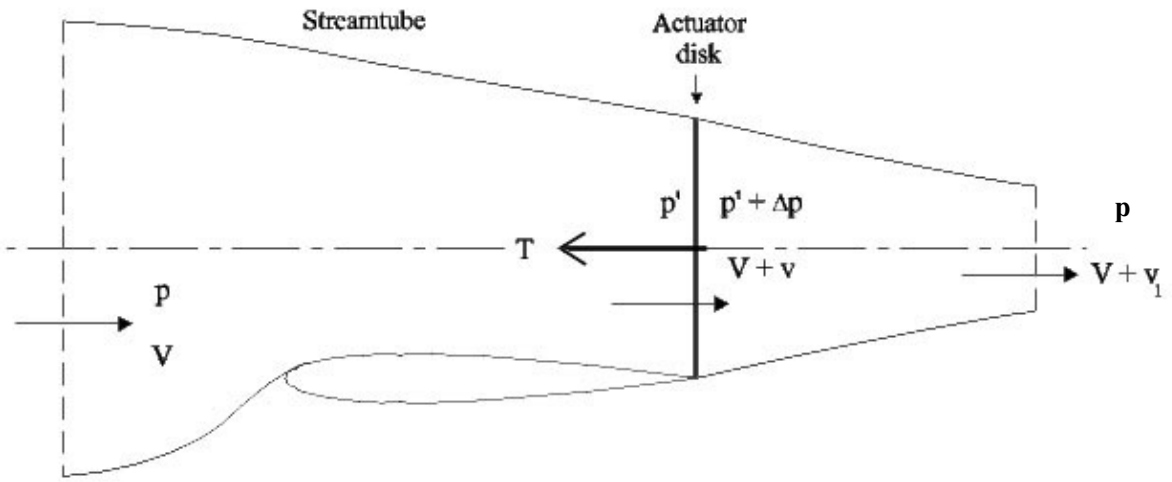

Figure 3.13 Streamtube of an induced flow pass an actuator disk

Since the Bernoulli equation applies only to a constant energy flow, stages of the flow ahead of the disk and behind the disk are considered separately.

$$p + 0.5\rho V^2 = p' + 0.5(V + v)^2 \quad \text{ahead the disk} \quad (3.8)$$

$$p + 0.5\rho (V + v_1)^2 = p' + \Delta p + 0.5(V + v)^2 \quad \text{behind the disk} \quad (3.9)$$

Thrust is calculated from a pressure different between the disk by subtracting Eqn. (3.8) and (3.9) from each other resulting in:

$$\Delta p = \rho\left(V + \frac{v_1}{2}\right)v_1 \quad (3.10)$$

$$T = A\Delta p = A\rho\left(V + \frac{v_1}{2}\right)v_1 \quad (3.11)$$

Momentum theory would indicate that the induced velocity far downstream is twice that at the disk.

$$\sum \vec{F} = T = \int_s \rho \vec{V}\left(\vec{V} \cdot d\vec{A}\right) = A\rho (V + v)v_1 \quad (3.12)$$

When Eqn. (3.11) and (3.12) are equated, it is seen that:

$$v_1 = 2v \quad (3.13)$$

Thus, for a given freestream velocity and thrust, the relation of induced velocity, v can be solved from Eqn. (3.11) and (3.13) as:

$$v = -\frac{V}{2} + \sqrt{\left(\frac{V}{2}\right)^2 + \frac{T}{2\rho A}} \quad (3.14)$$

(Roskam and Lan, 1997)

The ratio of induced and freestream velocity can be derived into the term of a thrust coefficient, $T_c = \dfrac{T}{q_\infty A}$, as the following:

$$\frac{v}{V} = -0.5 + 0.5\sqrt{1 + T_c} \quad (3.15)$$

For a freestream velocity, V, a chord length, c, and a section lift coefficient, C_l, an equation of 2D lift generated on the wing can be expressed as

$$l = \frac{1}{2}\rho V^2 c C_l \quad (3.16)$$

It is assumed that the wing chord is relatively small giving an unchanging induced flow over the wing upper surface. Therefore, the lift inside inboard-winglet channel is represented as:

$$l = \frac{1}{2}\rho\ V^2 c C_l \eta + \frac{1}{2}\rho\ (V+v)^2\, c C_l (1-\eta) \tag{3.17}$$

when η is a fraction of lift produced by the lower surface airfoil. It indicates that the lift is a combination of the lower surface lift of freestream velocity and the upper surface lift of propeller-induced velocity. This equation can be rearranged into a similar equation as Eqn. (3.16), showing a term of additional lift coefficient.

$$l = \frac{1}{2}\rho\ V^2 c \left[1 + (1-\eta)\left(2\cdot\left(\frac{v}{V}\right) + \left(\frac{v}{V}\right)^2\right)\right] C_l \tag{3.18}$$

The term $\left[(1-\eta)\left(2\cdot\left(\frac{v}{V}\right)+\left(\frac{v}{V}\right)^2\right)\right]$ indicates that an increase in a lift coefficient due to the input propulsive force varies to the ratio of induced and freestream velocity, which is a function of the thrust coefficient, T_c, at a specific lift fraction, η.

To apply the experimental data as a simple prediction for an increase in a lift coefficient in an actual flight performance due to an inboard-winglet application, pressure coefficients inside the winglet channel at the mid-section and 5 degree AOA were calculated for the lift coefficient by the procedure in section 3.2. Since it requires both upper and lower surface pressure coefficients which were not directly provided by the experimental data, a pressure distribution at the lower surface was assumed to be unaffected by the upper surface induced flow and the negative 5 degree AOA data of a conventional-wing at a power-off condition was applied as positive 5 degree AOA lower surface pressure coefficients instead. This assumption of unaffected lower surface flow characteristics needs to be verified in a further study. A thrust prediction of the experimental model, the same as that of an actual flight condition, was applied from so-called propeller performance charts using the data of a freestream velocity (V), a shaft horsepower (SHP), a propeller rpm (N), a number of blades (B) and an assumed blade activity factor (AF) and an integrated design lift coefficient (C_{L_i}) (Roskam, 1997). The variation in the lift coefficient and the thrust prediction of the experimental model would be used to estimate the lift coefficient of the Pegasus II at its thrust condition using the relation:

$$\frac{\Delta C_L}{C_L^*} = (1-\eta)\cdot\left(2\cdot\left(\frac{v}{V}\right)+\left(\frac{v}{V}\right)^2\right) \tag{3.19}$$

when $\frac{v}{V}$ is a function of T_c and an assumedly specific η was calculated from the experimental model mentioned above.

3.4 Pegasus II Design

To understand an application of the inboard-winglet concept to a real flight, a study model of a roadable aircraft was carefully evaluated. The roadable aircraft that uses the inboard-winglet concept to is the Pegasus designed by an AOE Senior Design team in 2000 for AGATE General Aviation Design Competition. Later in 2002, its modified version, Pegasus II, was developed to meet PAVE[4] requirements in a project sponsored by NASA. In the Pegasus II design, a maximum-width restriction for a road operation results in an unconventional wing design with the wing separated into 2 sections, an inboard wing and stowable outboard wings.

The main inboard section of 7-feet span, fitting the width restriction, and 8.5-feet chord is a rectangular untwisted wing using a GA(W)-1 airfoil as a wing section. Its main structure elements, being different from a conventional wing structure, enclose a box in which the outboard sections are stowed. This inboard section combined several concepts designed to help enhance vehicle performance, which suffered from the automobile width restrictions. Using a box-wing configuration, consisting of the inboard wing, horizontal stabilizer and vertical stabilizers/inboard winglets gives a needed improvement to a spanwise efficiency of the extremely low aspect ratio inboard wing. In addition to the box-wing configuration, the vertical stabilizers with an optimal twist act like winglets to provide a forward force component, giving a decrease in vehicle drag. The low aspect ratio of the wing becomes a great advantage in this situation since it sheds stronger vortices than a conventional planform wing at the winglet location. This enables the significant unique effect to a wing performance similar to a winglet at a wing tip. A propeller induced flow inside the box-wing enclosure also works similar to a channel wing concept when an increasing flow speed over a wing upper surface enhances a lift coefficient at low flight speed. Moreover, this configuration gives the propeller protection from accidental destruction, as it is located inside the enclosure of the structure. Furthermore, when employing an appropriate sound absorbing material on the inside surface of the box, there is a possibility that noise from the propeller and engine can be reduced during takeoff and landing. (Marchman, 2002)

[4] Personal air vehicle exploration, NASA LaRC

A major modification from the original Pegasus concept is the design of the outboard wing sections. A telescoping wing system used in the original design is questionable because of its extra weight and complexity as well as a possible lack of structure integrity. An application of the stowage outboard wings to the new design solves the problems mentioned in the telescoping wing concept since it relies only on 2 removable segments, each side of the outboard wing, employing a simple manual system for removal, stowage and attachment instead of a complete automation. Each segment attaches to an inboard wingtip by using a 1-foot span structure that fit into the box inside the inboard wing structure to transmit loads. For road operation, the outboard wing is manually pulled out, reversed in spanwise direction and inserted back into the inboard wing box. To do this, one outboard segment must be inserted upside-down. Since it must be fitted inside the inboard box, a semi-span of 5 feet and a chord of 5.2 feet were selected as dimensions for the outboard wing and a thinner 13-thick airfoil, GA(W)-2, were used as the airfoil section. Figure 3.14 shows drawings of the wing in both mode configurations. The significant saving in weight from less folding or use of a retracting mechanism can help provide improve vehicle performance even though the wingspan was extremely restricted. (Marchman, 2002)

Figure 3.15 is a three view drawing of the Pegasus II. It is a single engine, 4-wheel dual-mode vehicle. Its dimensions meet the 7 x 7 x 20 roadable limitation of the PAVE program. The vertical stabilizers located at the tip of the inboard wing have 5.14-feet span, 2.58-feet MAC, 3.68-feet root chord and 59-degree swept angle. A NACA 0008 airfoil is selected for the vertical section since an optimal thickness to chord ratio for a winglet is 8. For the horizontal stabilizer, a symmetrical NACA 0012 airfoil is used. Its planform has a span of 6.51 feet and a chord of 1.25 feet.

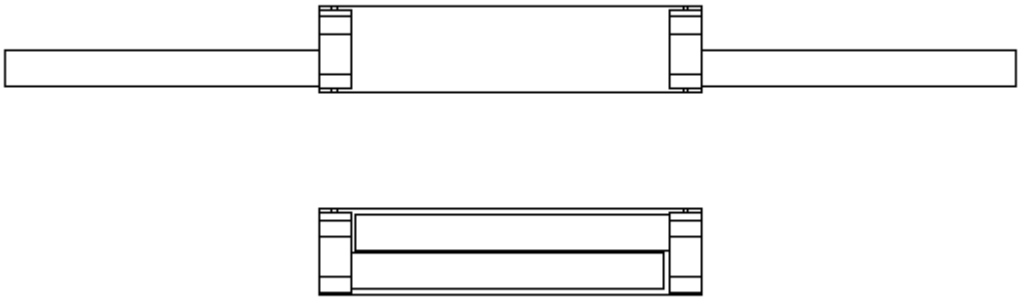

Front View

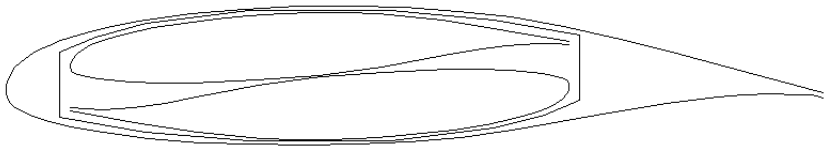

Side View

Figure 3.14 Outboard wing stowage concept

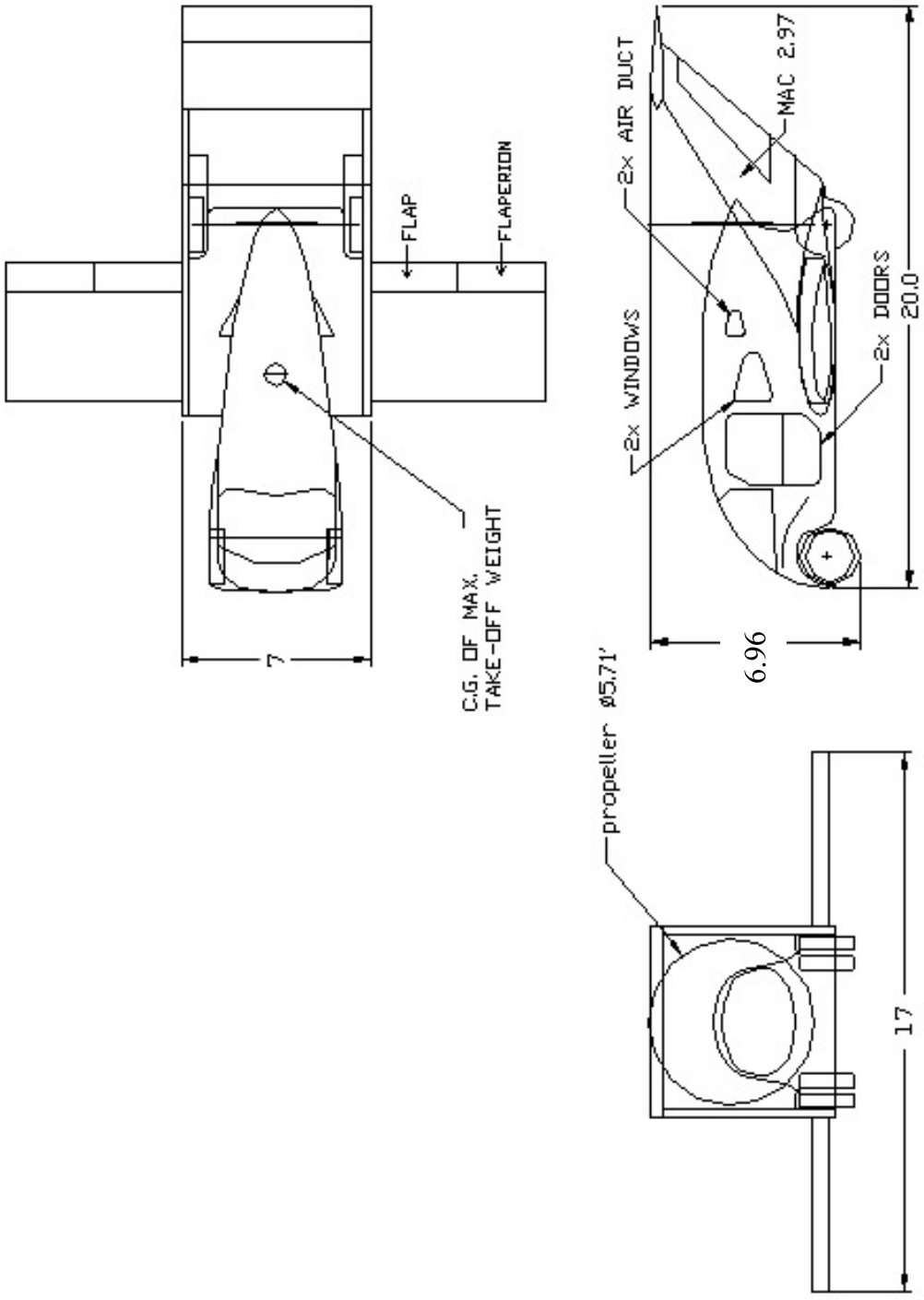

Figure 3.15 Pegasus II three-view drawing

3.5 Analytical Approximation of Thrust due to Inboard Winglets

A winglet is often used as a device to suppress a drag penalty of a fixed-wing aircraft since it does not only decrease the effect of spanwise flow between upper and lower wing surfaces, which influences a wing induced drag, but by using tip vortex energy, it also produces a forward component from its resultant force as an additional thrust. Basically, the stronger the vortices, i.e., a low aspect ratio wing, the more benefit the winglet can give (Raymer, 1989). Understanding the fundamental aerodynamics of the winglet helps indicate important factors for the analytical approximation of inboard-winglet thrust. An interaction of a wing-winglet flow field and a resultant force are demonstrated in Figure 3.16. In part a, besides having a downwash effect on itself, a wing also produces sidewash that, when combined to a freestream velocity, creates a forward aerodynamic force component on the winglet which is similar to a negative induced drag. A reverse effect also happens to the wing when the winglet s sidewash induces an upward component to the wing relative velocity, producing a resulting forward force component as showing in part b (Blackwell, 1976). To provide an advantage to overall wing performance, the negative induced drag of both wing and winglet, which depends on the aerodynamic load or circulation on the winglet, must overcome the combination of an induced and profile drag from this added winglet. Thus, the optimal design configuration of the winglet is only suitable for one selected flight condition.

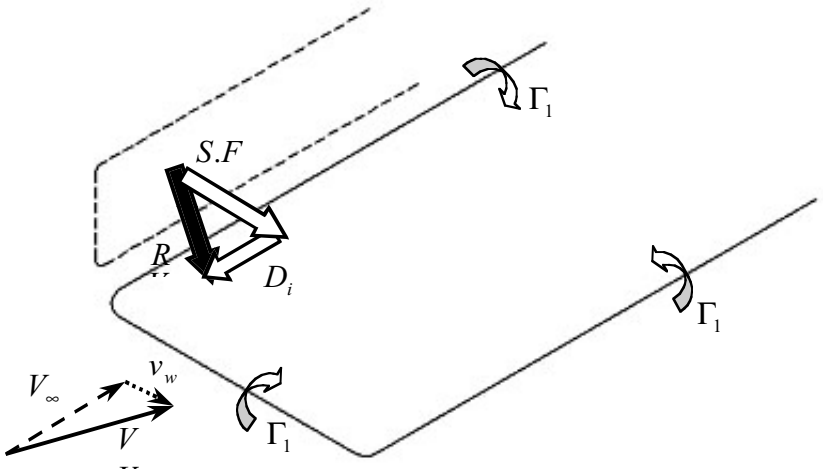

a) Wing induced winglet diagram

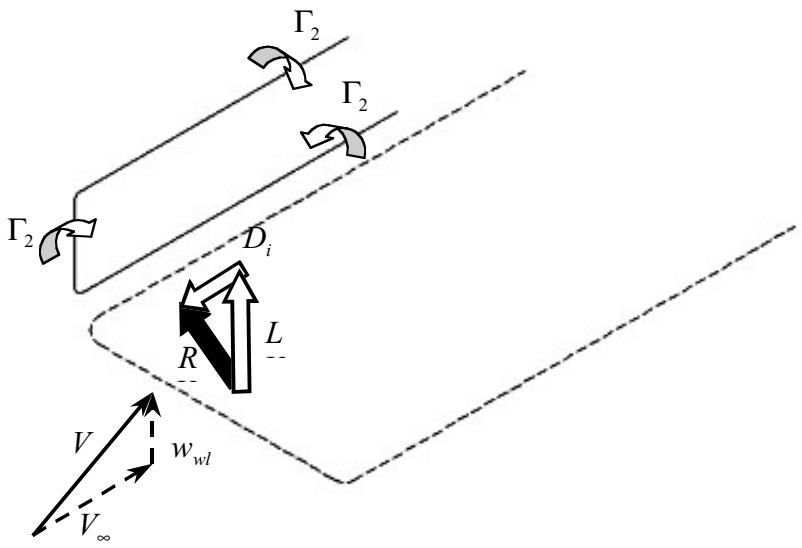

b) Wing induced winglet diagram

Figure 3.16 Diagrams of a wing-winglet interaction (Blackwell, 1976)

In the Pegasus II design, vertical stabilizers act like winglets for the inboard wing section. Trailing vortices, produced from a change in spanwise circulation at the junction of 2 wing parts, an inboard and outboard wing, induce the flow field for these inboard winglets to improve aircraft performance. Moreover, they simulate a similar flow field to a channel wing concept as a propeller between the winglets increases a flow velocity over a wing upper surface significantly in order to create an additional lift. The change of the inboard lift also strengthens the vortex circulation ($\Delta\Gamma$); as a result, providing a larger induced velocity (v_w) to enhance a winglet application. To analyze an approximate effect of the inboard winglet on the performance of the Pegasus II, the following approach was modified from the winglet analysis of the original Pegasus, developed by Will Anderson (Gassler, et.al, 2000). In his analysis for winglet optimal twists, the circulation change at the junction is assumed to be only a result of the change in section chords since the selected airfoil for an inboard and outboard wing are the same. There is no significant change in aerodynamic coefficients between the 2 sections since the three-dimensional effect barely makes a difference at the local point of interest. However, a modification was made in the Pegasus II wing design by having the inboard and outboard wing use different airfoils (see details in section 3.4).

To estimate the circulation at the junction, the 2-D lift of each wing section is expressed by Kutta-Joukowski theorem.

$$l = \rho_\infty V_\infty \Gamma \tag{3.20}$$

It also equals to the function of a section lift coefficient, a chord length and a dynamic pressure as known in basic aerodynamics.

$$l = \frac{1}{2}\rho_\infty V_\infty^{\,2} c C_l \tag{3.21}$$

The combination of Eqn (3.20) and (3.21) provides the circulation related to the lift coefficient and some other known characteristics. The vortex at the wing junction has its strength equal to the variation of the circulation between these 2 different wing sections with the notation of 1 for the inboard wing and 2 for the outboard wing.

$$\Delta\Gamma = \frac{1}{2} V_\infty \left(c_1 C_{l,1} - c_2 C_{l,2} \right) \tag{3.22}$$

From Eqn (3.22), the $\Delta\Gamma$ is a result of the variation in lift coefficients and chords. Whereas the difference in chords is constant through out the entire flight, the lift coefficient of inboard section, $C_{l,1}$, varies from the effect of propeller-induced flow. Currently, there is no analytical approximation for the lift coefficient of an inboard-winglet wing; thus the approximation at this point was converted from experimental data as shown in section 3.3. On the upper surface side, this vortex creates an inboard spanwise velocity over the wing as demonstrated in a vector diagram of Figure 3.17 which is given as a function of the distance from a vortex center, r .

$$v_w = \frac{\Delta\Gamma}{2\pi r} \tag{3.23}$$

Therefore, a relative velocity and an angle between it and the freestream velocity, from the vector combination of the freestream velocity, V_∞, and the spanwise velocity, v_w, also vary with the distance.

$$V(r) = \sqrt{V_\infty^2 + v_w(r)^2} \tag{3.24}$$

$$\alpha(r) = \tan^{-1}\left(\frac{v_w}{V_\infty} \right) \tag{3.25}$$

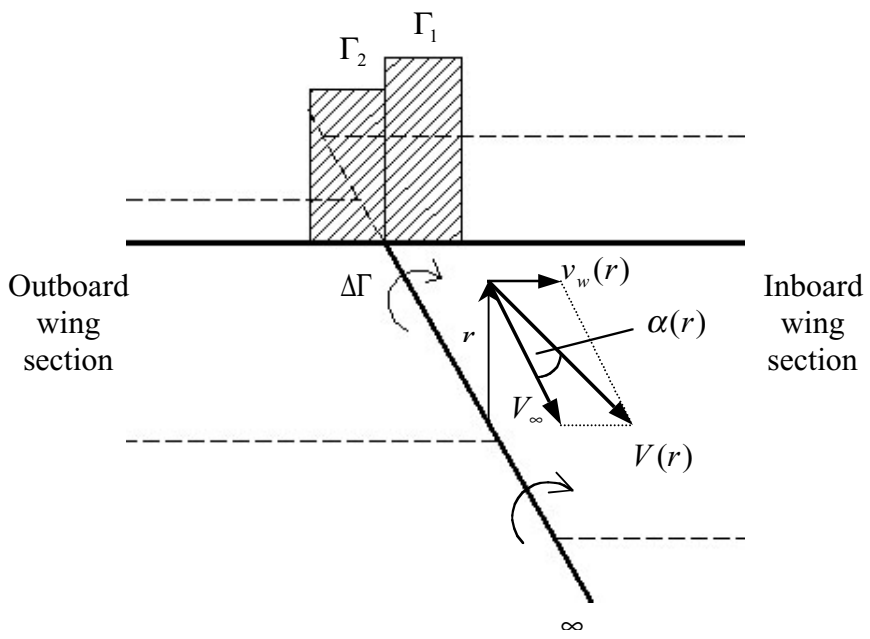

Figure 3.17 Diagram of a relative velocity due to a change in wing circulation

Aerodynamic forces acting on a winglet section also change relatively with an r station since they vary with a local angle of attack. To maximize thrust produced by the winglet with a known chord distribution and airfoil, it needs to have an optimal twist angle for every station to get the best advantage from a local angle of attack. For the Pegasus II s estimation, a winglet configuration was chosen to have the best performance at takeoff since it is vital to the study of the inboard winglet, which is mostly effective at the takeoff condition. Figure 3.18 shows a diagram of a relative velocity seen at a local station, r , of a winglet section. The local relative flow having an angle $\alpha(r)$ to a freestream direction provides a local angle of attack of $\alpha_l(r)$ for an airfoil section at that station. Therefore, the twist angle of the winglet is given by:

$$\gamma(r) = \alpha(r) - \alpha_l(r) \tag{3.26}$$

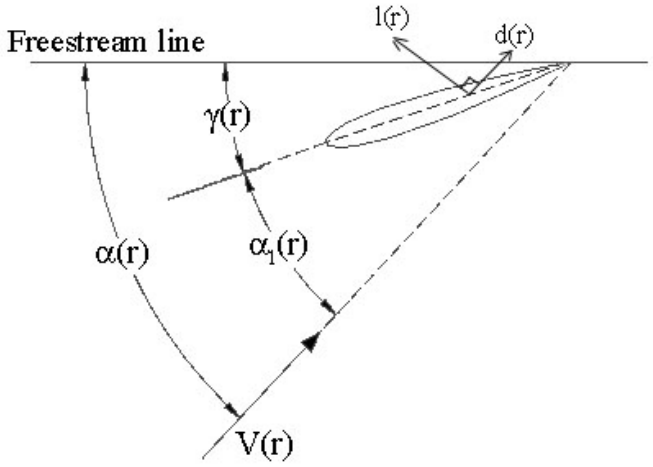

Figure 3.18 Diagram of lift and drag of a winglet cross-section at r station (Gassler, et.al, 2000)

To approximate an additional thrust due to the winglet, aerodynamic forces at each cross-section are evaluated to find a component parallel to the freestream. This means section lift, $l(r)$, and drag, $d(r)$, acting perpendicular and parallel to the relative velocity $V(r)$ respectively, define the thrust from the following relation:

$$\Delta t(r) = l(r)\sin(\alpha(r)) - d(r)\cos(\alpha(r)) \tag{3.27}$$

The delta term indicates that the thrust found from this approximation is only a rough approximation of a change the winglet can provide and is different from a real numerical value of the thrust.

An estimation of section lift and drag is assumed to have the same effect as the typical wing lift and drag calculations with $V(r)$ as their freestream velocity. The section lift can be evaluated from a lift coefficient as a function of an angle of attack,$\alpha_i(r)$:

$$l(r) = \frac{1}{2}\rho V(r)^2 c(r)[2\pi(\alpha_i(r))] \tag{3.28}$$

In this lift estimation, the 2D lift curve multiplied by the angle of attack is an approximation for the section lift coefficient, which from the thin airfoil theory is 2π since a great portion of the thrust is more likely generated by a larger local velocity magnitude and chord near the root of less 3D effect.

The section drag calculation is a conventional polar drag that is a combination of profile drag and induced drag. The profile drag coefficient is assumed constant for a small angle of attack and fixed dimensions of the winglet while the change in the induced drag significantly influences a winglet flow field. The equation is given by:

$$d(r) = \frac{1}{2}\rho V(r)^2 c(r) C_{d_0} + \frac{1}{2}\rho V(r)^2 c(r) \frac{[2\pi(\alpha_i(r))]^2}{\pi eAR} \tag{3.29}$$

Eqn (3.27) was numerically computed by varying the local angle of attack in order to acquire the maximize thrust for each section. The fact that the induced velocity from the trailing vortices is extremely high near the core creates an unrealistic effective angle of attack for the computation that would be restricted by a maximum angle of attack before stall of the airfoil section. After getting the best twist angle, the section thrust at the optimal twist angle was integrated to find the total additional thrust that would be use in the aircraft performance estimation.

3.6 Simplified Lift Coefficient Approximation for the Pegasus II

As mentioned in section 3.4, the Pegasus II wing design is a combination of several concepts put together for a better aircraft performance. The new wing concept applied 2 different airfoil sections, GA(W)-1 and GA(W)-2, to allow the outboard sections to be properly inserted in the inboard section and still have sufficient wing area. These 3 segments of wing, an inboard and 2 outboard wings, were integrated to produce a main lifting surface for the vehicle. Lift is also increased due to the added propeller-induced lift. In the conceptual design approach, the prediction of the wing lift coefficient is obtained by making 2 assumptions:

1. The lift distribution of the inboard section was considered to resemble that of a 2D airfoil due to the effect of vertical stabilizers at the tip of the section.
2. The lift distributions of the outboard wings were calculated by merging the 2 outboard section sides of wing and considering them to act as one continuous wing.

The equation employed to obtain average C_L max over the total wing is shown below:

$$C_{L\max} = \frac{S_i C_{L\max,i} + S_o C_{L\max,o}}{S} \tag{3.30}$$

where the notation i is for the inboard section and o is for the outboard section.

For the inboard section, the lift coefficient data is directly from the experimental data of the selected airfoil (McGhee and Geasley, 1980) without a variation from applying any high-lift device while for the outboard section, the calculation for the 3D lift coefficient with and without flap must be obtained from an approach as shown in Appendix A.

3.7 Performance Estimation of Comparator Aircraft and Sensitivity Study

Besides an analysis of the Pegasus II as a model for an inboard-winglet application, three different single-engine air vehicles were also selected as study models for a performance comparison, Cessna 182, Cirrus SR22 and LaBiche FSC-1. In a single-mode category, the Cessna 182, Skylane, is a choice of a common, well-known general aviation aircraft representing a conservative design, and the Cirrus SR22 was chosen to provide an alternative with a more advanced design to the comparison. In addition to the Pegasus II, another duel-mode vehicle, the LaBiche FSC-1, was examined because of its difference, a more automobile-like design. At the beginning, these comparator models were carefully estimated for characteristics and configurations as shown in Appendix B, based on published data and conceptual designs. After that, they were reevaluated for their performance in meeting the PAVE requirements following a general aviation mission profile in Figure 3.19, which is divided into 8 phases:

1. Engine start and warm-up
2. Taxi
3. Takeoff
4. Climb and accelerate to cruise altitude
5. Cruise for 400 nm
6. Loiter for 45 min
7. Decent
8. Landing, taxi and shutdown

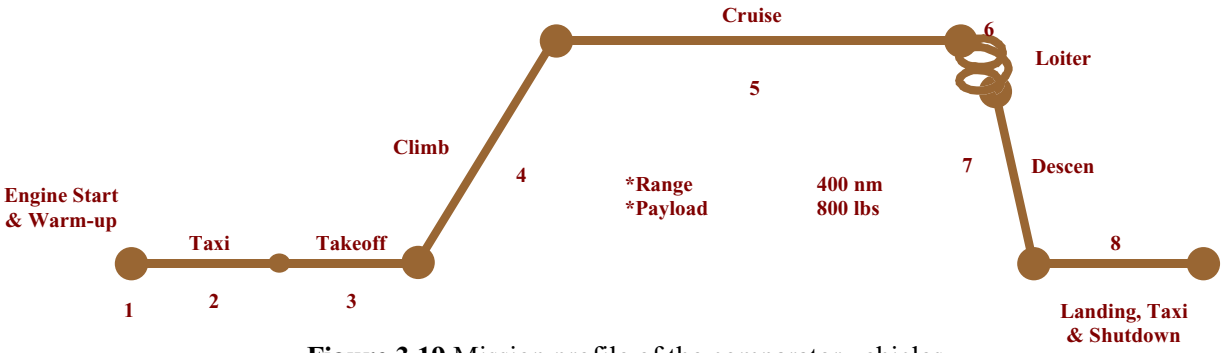

Figure 3.19 Mission profile of the comparator vehicles

In the case of the Pegasus II, The reevaluation also included approximations in channel lift and thrust due to a winglet application as shown in the previous sections. There is also a sensitivity study comparing to the Cirrus Sr22. For these 4 study models, a comparison was carefully made for these following issues: takeoff and landing distance, cruise and stall speed, and service and absolute ceiling. All performance estimations were calculated using a takeoff weight based on fuel needs for the 400-nm range requirement.

3.7.1 Takeoff Gross Weight and Fuel Weight Estimation

It is important to estimate the fuel used in the mission before starting to evaluate the performance of a vehicle. The estimation of mission fuel weight was based on the fuel-fraction method for propeller-driven airplane (Roskam, 1997), which is known as:

$$M_{ff} = W_{fi1} x W_{fi2} x W_{fi3} x W_{fi4} x W_{fi5} x W_{fi6} x W_{fi7} x W_{fi8} \tag{3.31}$$

where the notation numbers (1,2, ,8) are referred to the phases in the mission profile. Each phase has the ratio of final and initial vehicle weight in its period, W_{fi}, that when multiplied together, provide the total ratio of the final and initial weight. Equations of motion and statistical data are used to define a phase s fuel-fraction. In phase 1, 2, 3, 7, and 8 (W_{fi1}, W_{fi2}, W_{fi3}, W_{fi7}, W_{fi8}), assumptions of these phase weight ratio for a single-engine general aviation are 0.995, 0.997, 0.998, 0.993 and 0.993 respectively. These approximations are chiefly based on judgment while the rest are results of performance calculations.

Phase 4: Climb and accelerate (W_{fi4})

This fuel fraction was estimated from the time needed to climb with maximum rate of climb to cruise altitude in the endurance equation for propeller-driven airplanes. Also, there is an assumption that an engine is operated at the maximum constant power rating. The endurance equation is given as:

$$E = 375\left(\frac{1}{V}\right)\left(\frac{\eta_p}{c_p}\right)\left(\frac{L}{D}\right)\ln\left(W_{if4}\right) \tag{3.32}$$

The endurance equation indicates that a time to climb at a maximum rate of climb is needed to find the fuel fraction while V is set constant at takeoff velocity, usually assumed to be 1.2 times stall velocity. To gain the maximum rate of climb, an airplane must fly at the minimum power required condition. From a parabolic drag assumption, aerodynamic coefficients for this state are calculated from known parasite drag, C_{d0}, and induced drag factor, K.

$$C_{L,mp} = \sqrt{\frac{3C_{D0}}{K}} \tag{3.33}$$

$$C_{D,mp} = 4C_{D0} \tag{3.34}$$

The climb rate is assumed to be constant through out the phase, which is acquired from the maximum rate of climb equation. After that, a time to climb of the vehicle is approximated from a distance (height) divided by a velocity (rate of climb).

$$RoC_{\max} = 33000\left[\left\{\frac{\eta_p \sigma}{(TOGW/P)}\right\} - \left\{\frac{(TOGW/S)^{0.5}}{19\left(C_{L,mp}{}^{1.5}/C_{D,mp}\right)\sigma^{0.5}}\right\}\right] \tag{3.35}$$

$$E_{CL} = \frac{h_{cr} - h_{SL}}{RoC_{\max}} \tag{3.36}$$

Phase 5: Cruise (W_{fi5})

To determine a minimum fuel use in 400-nm cruise, Breguet s range equation, Eqn. (3.37), is evaluated at the minimum drag condition, which occurs when parasite drag equals to induced drag, to provide a higher lift to drag ratio for a propeller-driven airplane.

$$R = 375\left(\frac{\eta_p}{c_p}\right)\left(\frac{L}{D}\right)_{\max} \ln\left(W_{if5}\right) \tag{3.37}$$

$$(L/D)_{\max} = \frac{1}{2\sqrt{C_{D0}K}} \tag{3.38}$$

Phase 6: Loiter (W_{fi6})

According to FAR part 23, 45-minute loitering must be reserved for a single-engine airplane. To get the least amount of fuel use, Eqn (3.32) is applied at minimum power required condition. The velocity at that condition is obtained from:

$$V_{mp} = 0.68 \cdot \sqrt{\frac{2 \cdot TOGW}{\rho \ SC_{L,mp}}} \tag{3.39}$$

After calculating all fuel fractions and applying them to Eqn. (3.34), an actual-used fuel weight is given as:

$$W_{f,actual} = (1 - M_{ff})TOGW \tag{3.40}$$

A total fuel required for this mission have to include 5% reserve and 1% trapped fuel into the approximation.

$$W_f = 1.06 W_{f,actual} \tag{3.41}$$

Since the takeoff gross weight is relatively unknown at the beginning of this approximation, the fuel fraction estimation was reevaluated until a calculated fuel weight corresponded to the input takeoff gross weight from a summation of empty weight, payload and fuel weight. The resulting fuel weight and takeoff gross weights are essential for the performance calculations

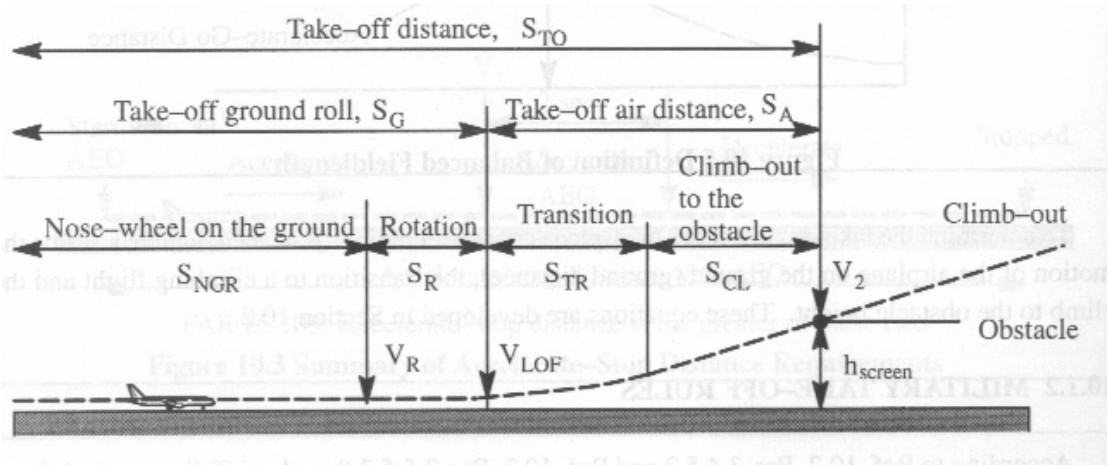

Figure 3.20 Geometry of Takeoff distances (Roskam and Lan, 1997)

3.7.2 Takeoff Distance[5]

After getting the takeoff gross weight, aircraft performance was evaluated starting with a takeoff distance. The distance is divided into 4 parts as shown in Figure 3.20: nose-wheel on ground, rotation, transition and climb to the obstacle. Velocities must be found for every phase. In general, an airplane accelerates to a takeoff velocity (V_{TO}), approximated to be 120% of a stall velocity (V_s) at its takeoff configuration and then rotates to an angle of attack that provides a takeoff lift coefficient ($C_{L,TO}$), which equals 80% of a maximum lift coefficient ($C_{L\max}$). At this point, the airplane starts to lift off the runway and transitions to a climbing angle until it reaches desired altitude.

$$V_{TO} = 1.2 \cdot V_s \tag{3.42}$$

$$C_{L,TO} = 0.8 \cdot C_{L\max} \tag{3.43}$$

For a ground roll distance, S_{NGR} and S_R, there are several approaches to estimate the acceleration on the ground of these vehicles. According to a force diagram of the airplane during the ground roll, 5 forces dominate a ground roll distance calculation, lift, drag, thrust, weight, and friction, and these vary with a velocity. Therefore, in this case, it is assumed that

[5] (Roskam and Chuan-Tau, 1997) and (Nicolai, 1975)

overall accelerating velocities are approximately equal to a constant 70% of V_{TO}. The calculation of those forces is based on an assumption of no aerodynamic ground effects. A ground friction coefficient (μ) of 0.025 for concrete and macadam was used to find the friction force. The distance when nose-wheel on the ground is indicated as:

$$S_{NGR} = \frac{1.44 \cdot (TOGW / S)_{TO}}{g\rho\, C_{L\max}\left[\frac{T-D}{TOGW} - \mu\left(1 - \frac{L}{TOGW}\right)\right]} \tag{3.44}$$

For a general aviation airplane, a rotation distance is usually assumed to have a constant takeoff velocity for 1 second.

$$S_R = V_{TO} \tag{3.45}$$

For a transition distance, an airplane completely lifts off a ground and gradually changes to a climb angle by a constant-velocity arc (θ_{CL}) of a radius (R_{TR}) in Eqn. (3.46), (3.47) and (3.48) whereas a load factor of an airplane is assumed to be 1.15.

$$R_{TR} = \frac{V_{TO}^2}{0.15g} \tag{3.46}$$

$$\theta_{CL} = \sin^{-1}\left(\frac{T-D}{TOGW}\right) \tag{3.47}$$

$$S_{TR} = R_{TR} \cdot \sin(\theta_{CL}) \tag{3.48}$$

$$h_{TR} = R_{TR}\left[1 - \cos(\theta_{CL})\right] \tag{3.49}$$

A field length definition of FAR part 23 includes a distance to clear an obstacle 50 ft above the ground. If the transition height in Eqn (3.49) is less than that, the airplane climb distance to over 50 ft must be considered as indicated in Eqn. (3.50).

$$S_{CL} = \frac{50 - h_{TR}}{\tan(\theta_{CL})} \tag{3.50}$$

However, if the transition height already exceeded the restriction, the takeoff distance is considered up to the point where the airplane reaches 50 ft height above the ground in transition mode. The total takeoff distance covers both the takeoff ground roll and the air distance when the takeoff ground roll is a summation of S_{NGR} and S_R.

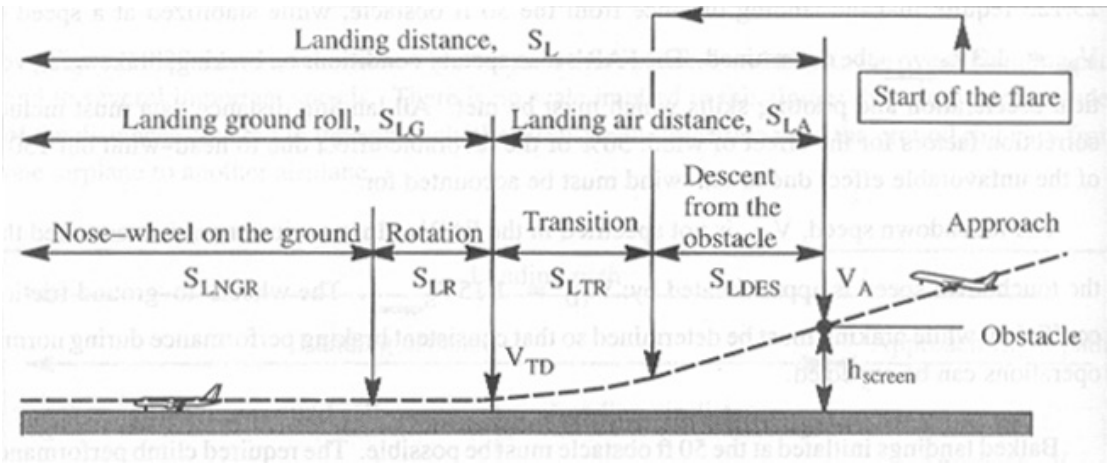

Figure 3.21 Geometry of Landing Distances (Roskam and Lan, 1997)

3.7.3 Landing Distance[6]

Similar to the takeoff distance, a landing distance from FAR part 23 is considered to be from the point when the airplane is clear a 50 ft obstacle until it comes to a complete stop (Figure 3.21). An approached speed (V_A) is required to be 130% of stall speed (V_s) in the landing configuration while an approach lift coefficient ($C_{L,A}$) is defined by V_A.

$$V_A = 1.3 \cdot V_s \tag{3.51}$$

$$C_{L,A} = \frac{C_{L\max}}{1.69} \tag{3.52}$$

With an idle thrust assumption, a flare angle (γ_A) is determined from Eqn. (3.53) at an approaching wing angle. To find the flare radius in Eqn. (3.54), an approximation of a flare velocity (V_{FL}) is 95% of V_A and a load factor is 1.08 due to a steep flight path angle. They were applied to a calculation of a landing air distance, combining 2 phases, approaching and flaring, as indicated in Eqn. (3.55).

$$\gamma_A = \sin^{-1}\left(-\frac{T}{TOGW} + \frac{L}{D}\right) \tag{3.53}$$

[6] (Roskam and Chuan-Tau, 1997)

$$R_{FL} = \frac{V_{FL}^2}{g(n_{FL} - 1)} \tag{3.54}$$

$$S_{LA} = \frac{50}{\tan(\gamma_A)} + R_{FL}\,\frac{\gamma_A}{2} \tag{3.55}$$

The touch down velocity (V_{TD}) must be 1.15 V_s by FAR requirements. After that the airplane rotates to a level position. An assumption of a rotation time is 1 second.

$$V_{TD} = 1.15 \cdot V_s \tag{3.56}$$

$$S_{LR} = V_{TD} \tag{3.57}$$

With a brake located at the main gear, ground friction coefficients were assumed to be 0.4 at the main gear and 0.025 at a nose gear. An approximation of a weight ratio at the nose gear is 0.08. A nose-wheel on ground landing distance is calculated by the following equation as:

$$S_{LNGR} = \left\{\frac{TOGW/S}{g\rho\,(C_D - \mu_{break} C_L)}\right\} \ln\left[1 + \frac{(V_{TO})^2\,\rho\,(C_D - \mu_{break} C_L)}{2 \cdot \frac{TOGW}{S}\left\{\left(\mu_{break} - \frac{T}{TOGW}\right) - \frac{N_n}{TOGW}(\mu_{break} - \mu)\right\}}\right] \tag{3.58}$$

Thus, a landing ground roll is obtained from adding the rotation to the nose-wheel on ground distance. A total landing distance is a summation of the landing ground roll to the air distance.

3.7.4 Maximum Cruise Velocity[7]

Only 80% of available engine horsepower was assumed to be used at maximum cruise velocity. It is defined as the velocity where power available (P_A) equals power required (P_R) for a level flight at a desired cruise altitude. The power required is given as:

[7] (Anderson, 1989)

$$P_A = 0.8 \cdot 550 \cdot \eta_p \cdot hp \cdot \sigma \tag{3.59}$$

$$P_R = \frac{1}{2}\rho\, V^3 SC_{D0} + \frac{K \cdot TOGW^2}{\frac{1}{2}\rho\, VS} \tag{3.60}$$

Figure 3.22 demonstrates a plot of the power available and the power required curve over a range of velocities. The velocity at the intersection of the two curves is an indicated maximum velocity.

3.7.5 Stall Velocity[8]

The stall velocity for an airplane is determined by its takeoff gross weight and maximum lift coefficient, which varies with the choice of an airfoil section, the use of a high-lift device, as well as the altitude. In this performance comparison, all results would be calculated at true air speed as shown:

$$V_s = \sqrt{\frac{2 \cdot TOGW}{\rho\, SC_{L\max}}} \tag{3.61}$$

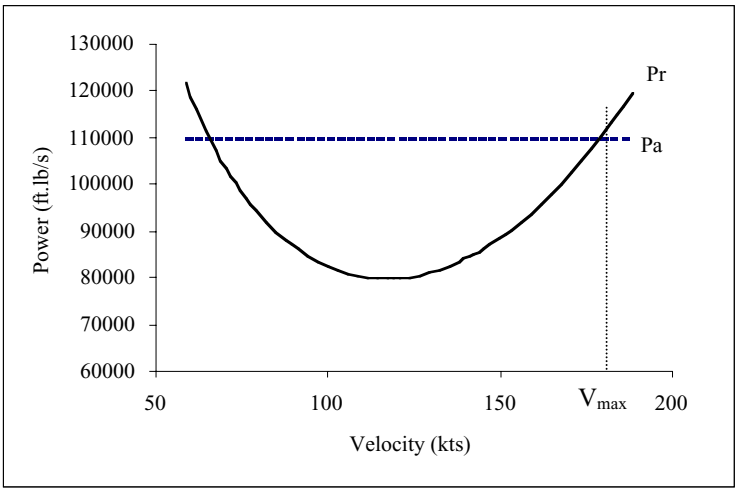

Figure 3.22 Power-required and available curve

[8] (Anderson, 1989)

3.7.6 Service and absolute ceiling[9]

From FAR part 23, a service ceiling implies an altitude that a maximum rate of climb is 100 fpm, while an absolute ceiling means the maximum rate of climb equals to zero. By applying the rate of climb equation, Eqn. (3.35), densities corresponding to the rate of climb conditions of 0 and 100 fpm can be determined in order to verify standard atmospheric altitudes of the conditions.

The performance estimation of these comparator aircraft helps specify advantages and disadvantages of the inboard-winglet application to the Pegasus II since the comparison was based on the other reliable existing designs. A sensitivity study was performed by varying 5 design parameters, maximum lift coefficient, profile drag coefficient, empty weight, specific fuel consumption, and engine horsepower. The study was observed for an effect to the aircraft performance when decreasing maximum lift coefficient, profile drag coefficient, empty weight for 10% and increasing specific fuel consumption, and engine horsepower for the same amount.

[9] (Roskam and Chuan-Tau, 1997)

Chapter 4

Results and Discussion

4.1 Experimental Data Analysis

To analyze flow characteristics of the wing with the inboard-winglet concept, the pressure coefficients measured from the wind tunnel testing were plotted along chordwise and spanwise positions for every angle of attack and freestream velocity. Both the power-off and power-on cases were separately discussed before making a comparison later. The experimental spanwise pressure distributions of the conventional wing were examined as a reference. Besides a comparison to the conventional wing, the 2D theoretical estimation from "Eng Applets: Vortex Panel Method[10]" was also run to better define the physical behavior of the flow. It is a computational tool, based on JAVA, using a vortex panel method to examine the aerodynamics of an airfoil section in ideal flows (Devenport and Vadapalli, 1998). The resulting numerical data, computed in terms of the normal and axial forces on the main wing and winglet model, were used to determine lift and drag.

4.1.1 Pressure Coefficients at Power-Off Condition

The first stage of the experiment was to determine the characteristics of the flow over the wing upper surface and the inboard winglet structures without any influence from propeller-induced flow. The pressure coefficients were plotted against x/c for the chordwise positions and y/b for the spanwise position as shown in Figure 4.2 – 4.45. Having all velocity data in the same graph provides an observation of the effect of Reynolds number on the pressure distribution. Besides the experimental results, the theoretical

[10] Java applets for engineering education, Virginia Tech

pressure coefficient of a two-dimensional NACA0012 was also plotted as solid lines. The wing sections discussed in this pressure distribution analysis are in Figure 4.1.

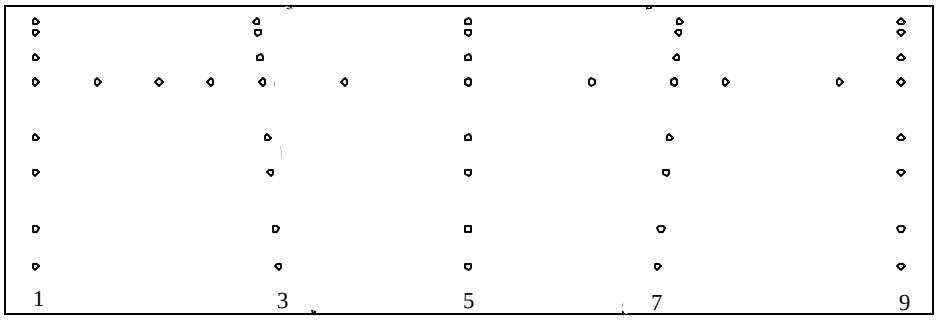

a) Conventional wing pressure taps

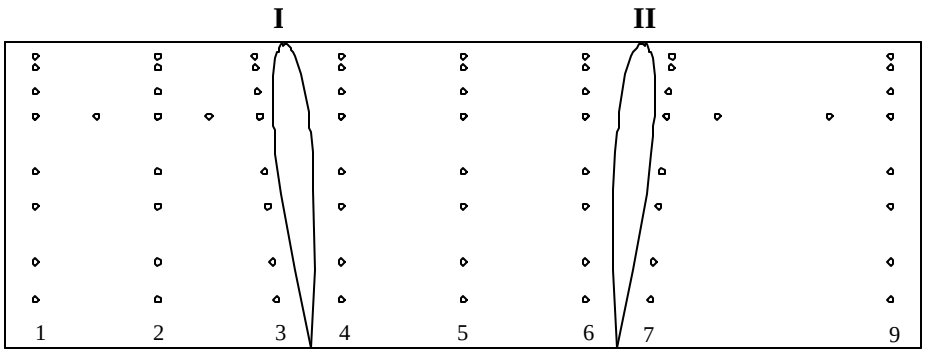

b) Inboard-winglet pressure taps

Figure 4.1 Pressure tap locations for various models

Plots of pressure coefficient at the outmost location on the upper surface of the main wing, section 1, indicated a similar pattern of experimental pressure distribution to the theoretical curve as shown in Figure 4.2, 4.10, 4.18 and 4.26 for angles of attack of –5 to 10 degree. A three-dimensional effect plays a common role as anticipated. At 0-degree angle of attack (AOA) (Figure 4.10), the dissimilarity between the experimental and theoretical curve was barely noticed due to the fact that the non-cambered wing section supposedly produces no lift or downwash; on the other hand, at negative and positive angle of attack, it indicated

the sign of upwash and downwash effect respectively. The flow remained attach to the wing surface throughout the entire angle of attack variation without experiencing any separation.

For the next wing section inboard, section 2, the presence of winglet structure becomes more significant. Figure 4.19 shows that the pressure distribution of the 0-degree AOA slightly changes, having higher absolute values when compared to that of the section 1. As a matter of fact, the pressure coefficients tend to increase in the negative direction for every angle of attack as also presented in Figure 4.3, 4.11 and 4.27. The lowest test speed, at a dynamic pressure of 0.2 inches of water, had a laminar separation around 0.1-0.2 x/c at 10-degree AOA while the rest of the plot for this section established a comparable distribution.

At section 3, the pressure distribution pattern as shown in Figure 4.4, 4.12, 4.20 and 4.28 seems to disagree with the theoretical one. The pressure taps, align to a winglet chord line on the adjacent outboard part, measured a jump in the pressure coefficient around 0.2 x/c at the low angles of attack, -5 and 0 degree. A similar pattern was also seen in the 5 and 10-degree AOA curve, with the jump moving forward to around 0.1-0.2 x/c. The upper surface pressures were less than expected and all experimental pressure distribution curves are outside the 2D envelopes. For a dynamic pressure of 0.2 inches of water, a separation bubble started to have an effect when the curve is flat near the leading edge at 5-degree AOA (Figure 4.20). It is possible that a separation occurred over the entire section at 10 degree AOA (Figure 4.28) since the experimental pressure coefficients were completely unrelated to the theory.

The inboard part of the wing located between the two winglets experiences a somewhat different flow field from the outboard part. The results from this part of the wing, given from 3 columns of chordwise pressure taps as well, indicated that the distribution pattern reasonably followed the theoretical data without a large jump like in section 3. The presence of the winglets seems to have less effect to this part of the main wing than on the outboard part. In Figure 4.5, 4.13, 4.21, and 4.29, the experimental data of section 4 was somewhat close to that of section 2 if separations were excluded. It appears that laminar separations may have occurred on this section as a consequence of a winglet location. The 0.2-inch-of-water dynamic pressure condition still produced evidence of separation bubbles near the leading edge. They are generated around 0.1-0.2 x/c in the low AOA case and move further downstream to 0.2-0.3 x/c in the higher AOA case (5,10 degree).

For the middle section, section 5 (Figure 4.6, 4.17, 4.22, and 4.30), the flow seems barely affected by the presence of the winglets as indicated in Figure 4.14 of the 0-degree AOA case. The curves in that plot correspond more similar to the 2D reference due to the fact that there is theoretically no downwash at the zero lift condition. Flow passing this section appears to be smoother than that for section 4 with the only exception at 10 degree AOA (Figure 4.30), which seem to have leading edge separation at 0.05-0.2 x/c in all velocity ranges. Section 6, shown in Figure 4.7, 4.18, 4.23, and 4.31, is similar to section 4 with smoother flow field. Since there is no evidence of separation from the pressure distribution curve, it could be assumed that unlike winglet I, the interaction between the main wing and winglet II flow field caused fewer disturbances to excite a laminar separation.

The other outboard part of the wing, connected to the mounting structure, was examined for only 2 columns of chordwise pressure taps since it provides little flow information due to tunnel wall and other interference factors around that area. However, those factors seem to have no effect to the flow between the winglets and beyond. The data of Section 7 was similar to that of section 3 as shown in Figure 4.8, 4.19, 4.24, and 4.32. Separation bubbles at low speed moved forward as the angle of attack increased. For section 9 (Figure 4.9, 4.20, 4.25, and 4.33), the pressure distributions do not follow the theoretical patterns very well. At the 5 and 10-degree AOA case, they even appeared to have too much disturbance for the flow appears to be separated.

The spanwise pressure distribution experimental data at the wing quarter chord, as plotted in Figure 4.34-4.37, was measured from 12 pressure taps described in chapter 3 and shown in Figure 4.1. A set of data from a conventional wing was used as a comparing reference. It is clearly visible that the extra structures cause an extreme change to the pressure coefficients near them with an exception at the mid-span, and there is only a slight variation at the tips of the main wing. The points (point 5 and 9) located next to the winglets on the outboard side are affected the most. The possible explanation is that the circulation producing lift on the winglets interacts with the main wing flow field causing velocity increase on the winglet suction side; thus, the pressure on that side greatly decreases from the reference giving higher negative pressure coefficients. A different between the reference and the inboard-winglet wing also varies with a change in an angle of attack. At 0-degree

AOA (Figure 4.35), the wing without circulation seems to have the biggest different range while the range becomes smaller as the circulation strength increases (both positive and negative side).

Figure 4.38 through 4.45 show the pressure coefficient data of both sides of the winglets. They were plotted together and compared with the 2D data of 5 and –5-degree AOA in winglet I and winglet II respectively. The results indicate that there are remarkable change between them and the 2D data due to 3D effect of the small aspect ratio finite wing. The separations on the main wing affected the pressure measurement on winglet I at 5 and 10 degree AOA for the freestream dynamic pressure of 0.2 inches of water (Figure 4.40 and 4.41). Additionally, The sidewash velocity component from the main wing alters the effective angle of attack for the winglets, creating a shift of the pressure coefficients to the more negative direction as the wing angle of attack increases. The same phenomenon also appears on winglet II (Figure 4.44 and 4.45). Since there was no severe separation on wing section 7, the flow seems smoother pass the winglet at this location.

Generally with no propulsive force, the experimental results indicate that the circulation of the winglets induced a flow velocity on the wing surface to increase both inboard and outboard section presence. However, a greater effect occurs on the outboard side because a velocity component has a higher magnitude on the winglet suction side. The main wing circulation also alters the winglet flow field when its sidewash changes the envelope of the winglet pressure coefficient by altering a winglet effective angle of attack. That change has a reverse effect on the wing pressure distribution, which varies with circulation strength. The variation in Reynolds number proved to have greater effect only when dealing with a laminar separation at low Reynolds number of 145879.

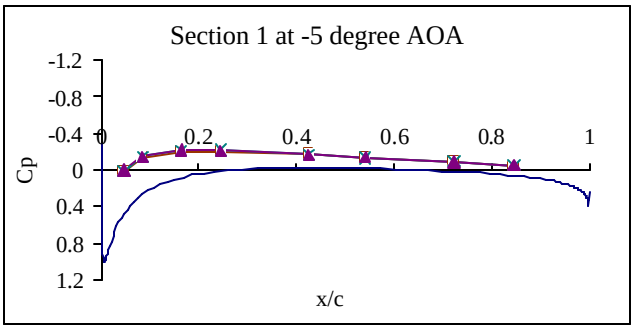

Figure 4.2

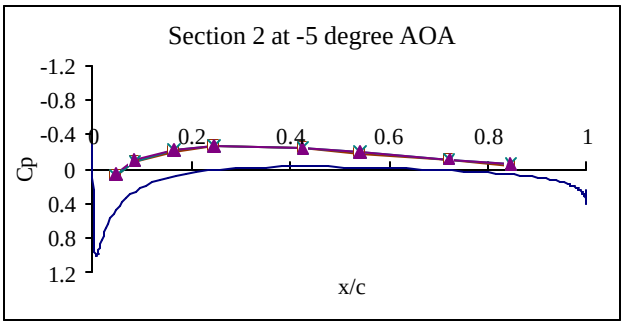

Figure 4.3

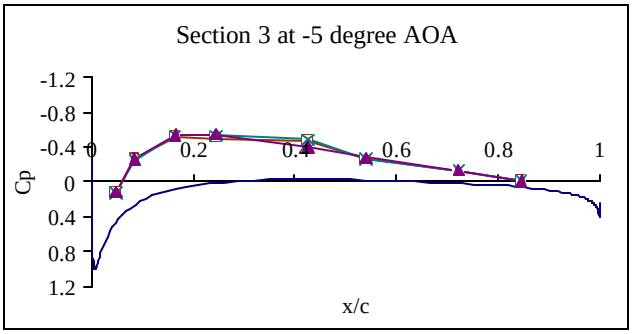

Figure 4.4

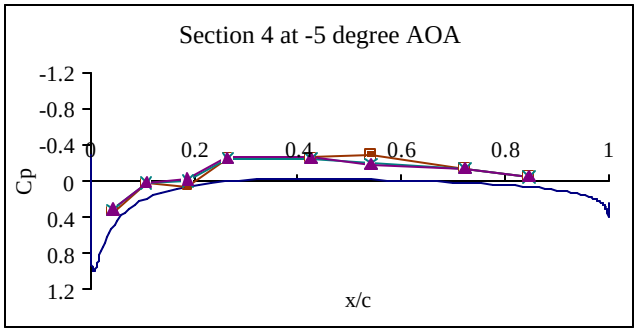

Figure 4.5

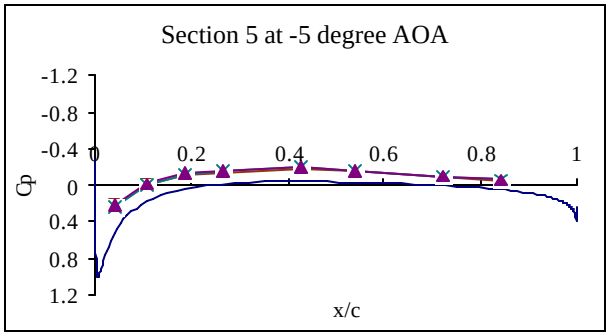

Figure 4.6

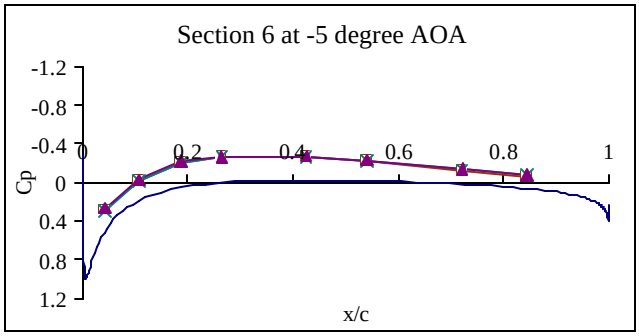

Figure 4.7

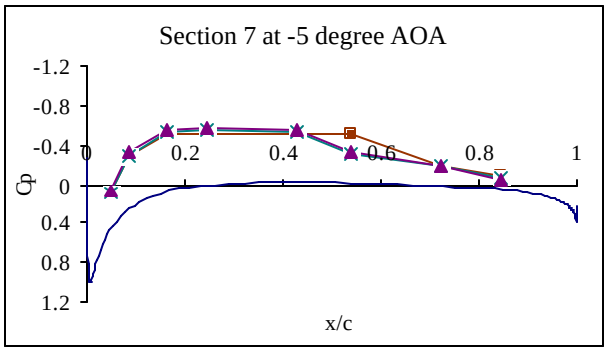

Figure 4.8

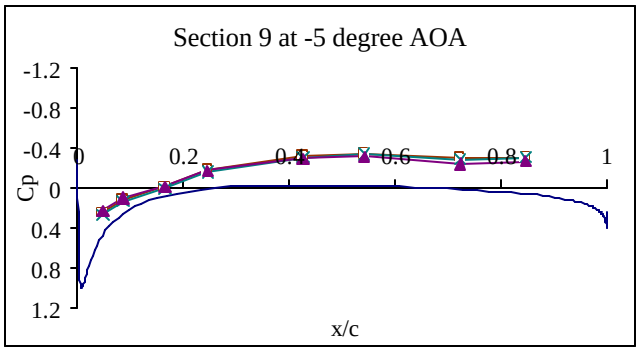

Figure 4.9

Figure 4.2-4.9 The pressure distributions of the inboard-winglet wing at -5 degree angle of attack

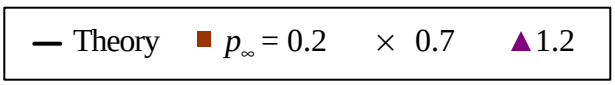

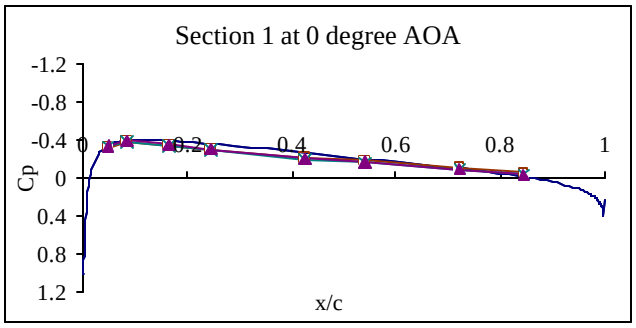

Figure 4.10

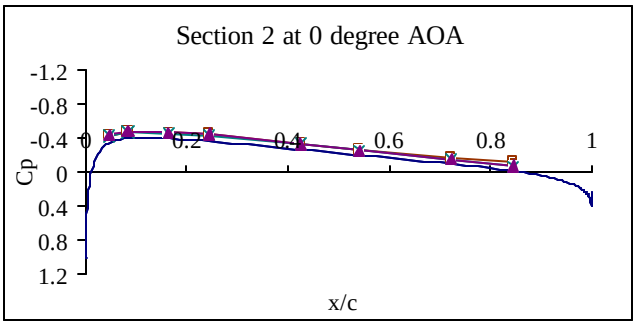

Figure 4.11

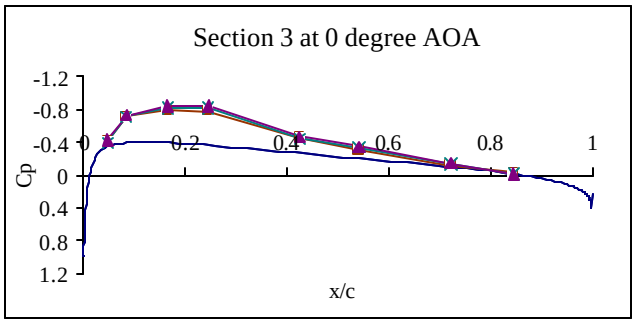

Figure 4.12

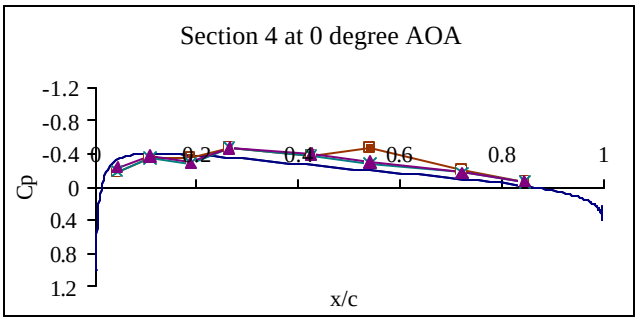

Figure 4.13

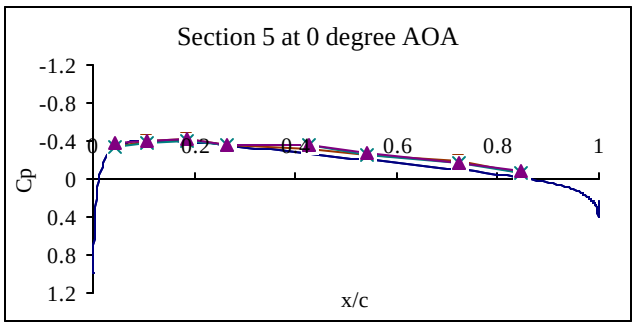

Figure 4.14

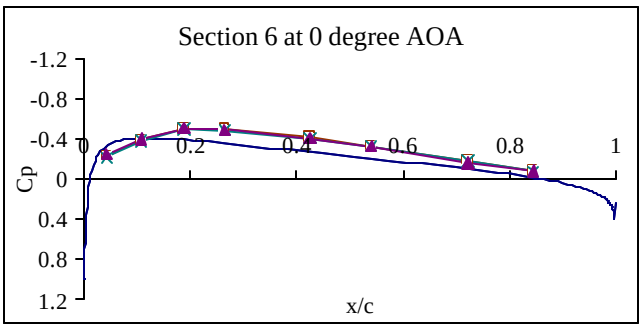

Figure 4.15

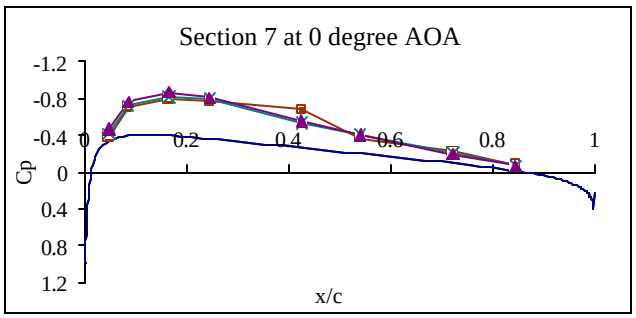

Figure 4.16

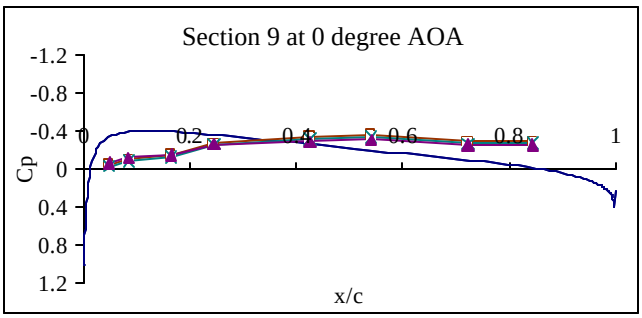

Figure 4.17

Figure 4.10-4.17 The pressure distributions of the inboard-winglet wing at 0 degree angle of attack

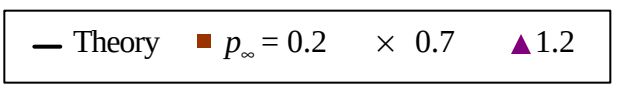

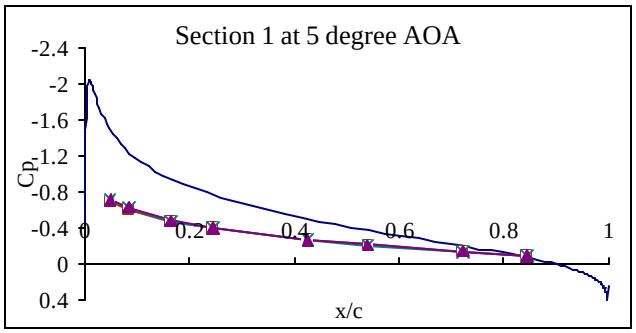

Figure 4.18

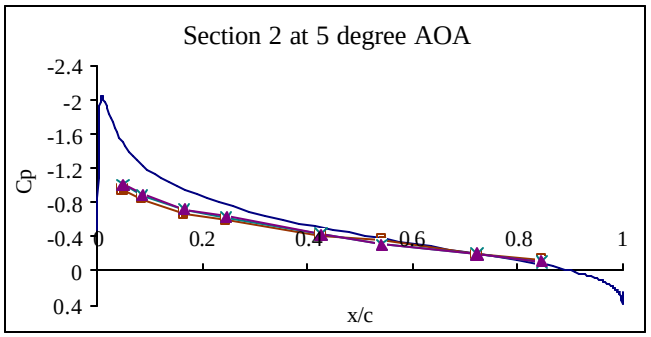

Figure 4.19

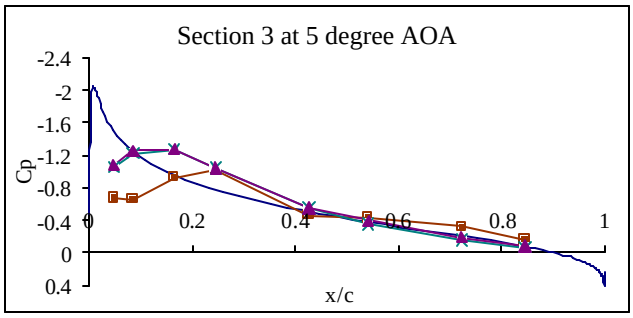

Figure 4.20

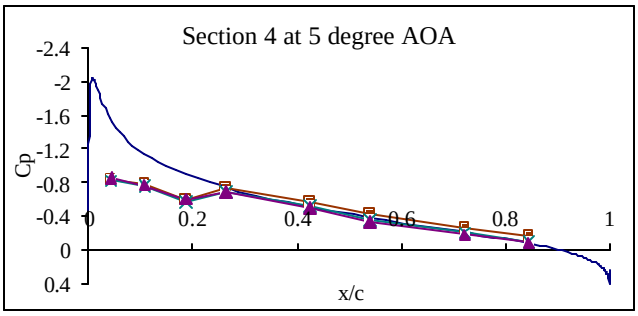

Figure 4.21

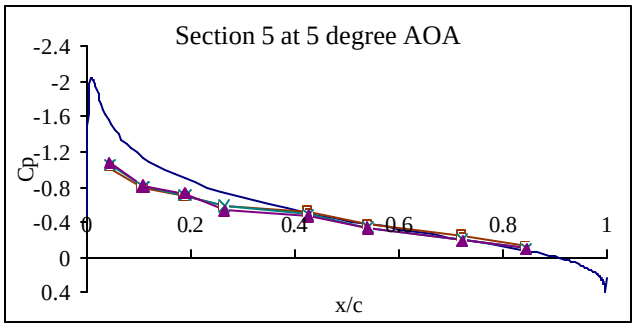

Figure 4.22

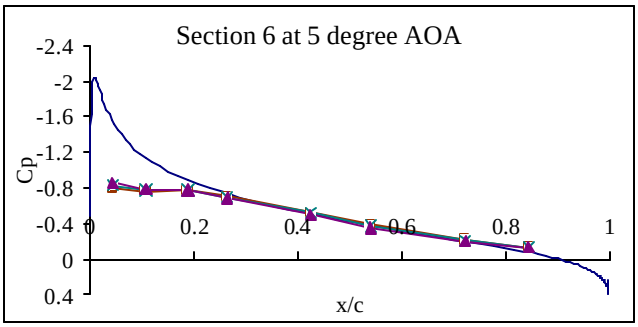

Figure 4.23

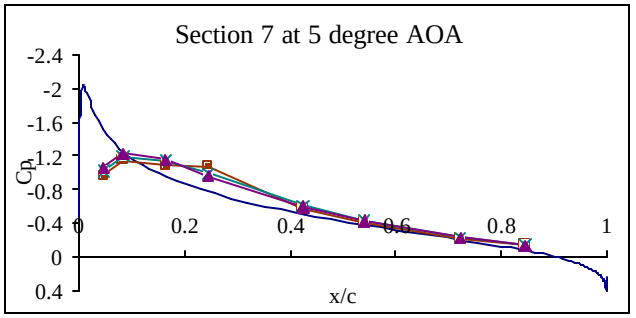

Figure 4.24

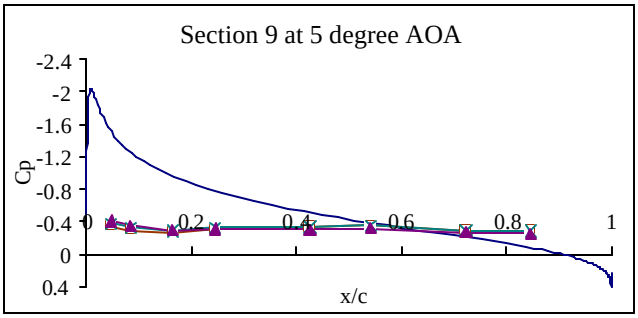

Figure 4.25

Figure 4.18-4.25 The pressure distributions of the inboard-winglet wing at 5 degree angle of attack

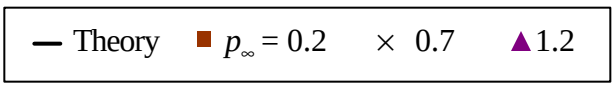

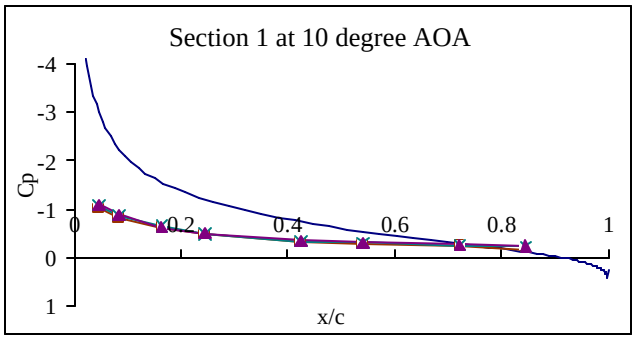

Figure 4.26

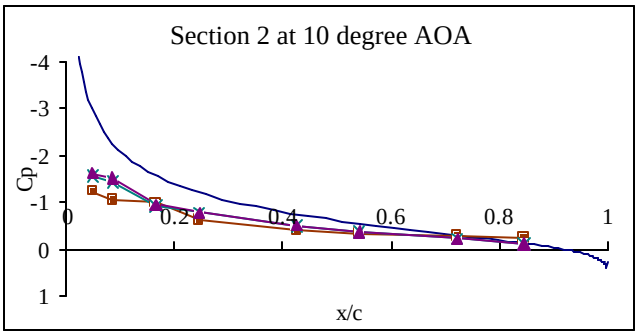

Figure 4.27

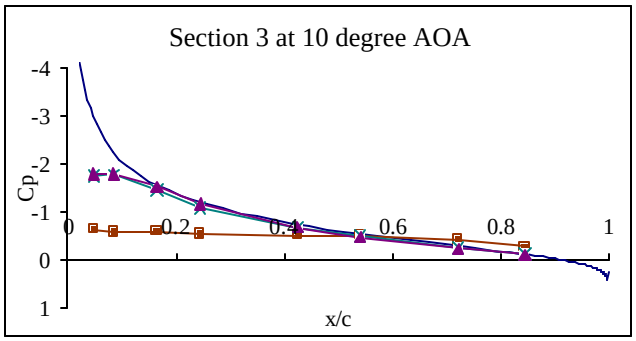

Figure 4.28

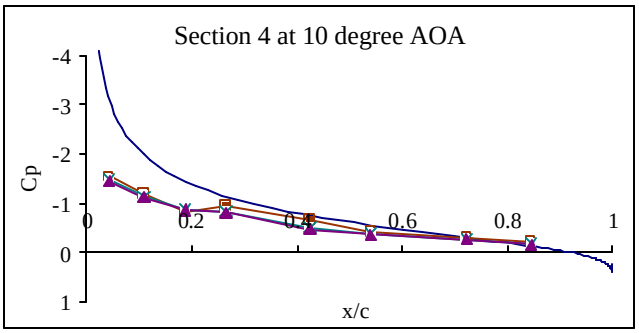

Figure 4.29

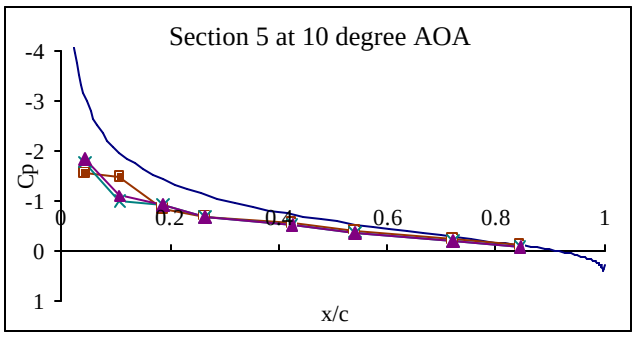

Figure 4.30

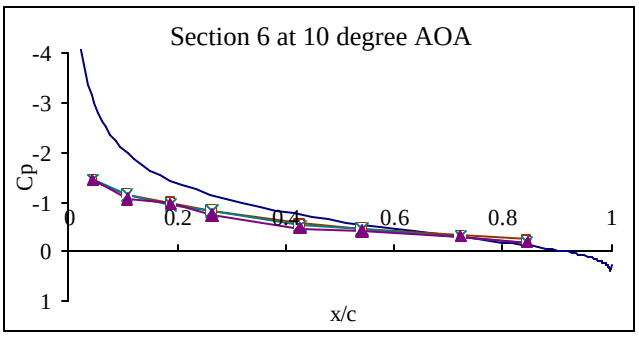

Figure4.31

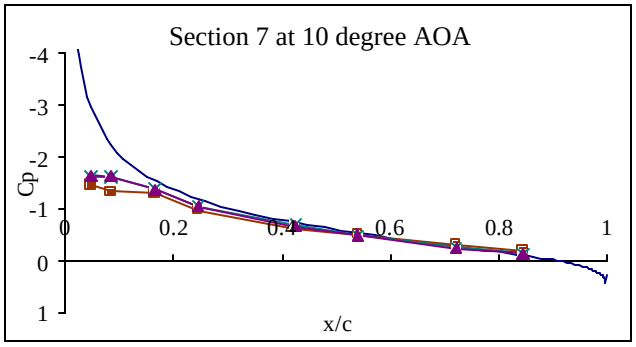

Figure 4.32

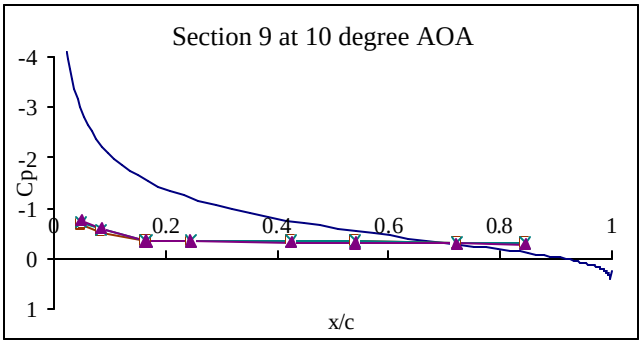

Figure 4.33

Figure 4.26-4.33 The pressure distributions of the inboard-winglet wing at 10 degree angle of attack

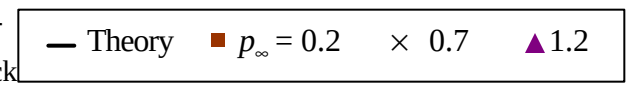

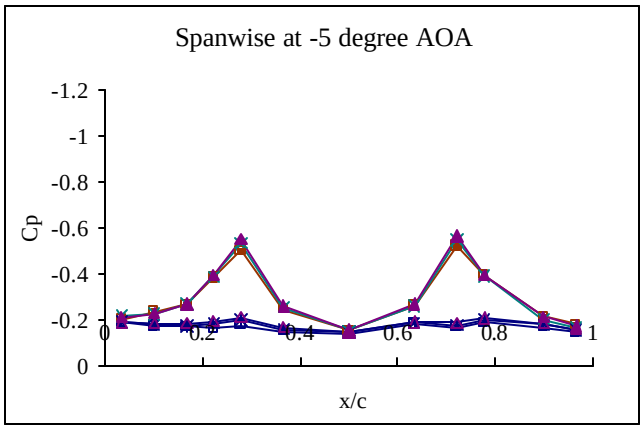

Figure 4.34

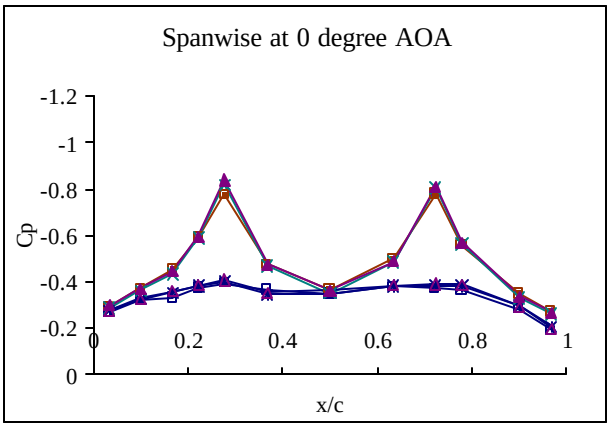

Figure 4.35

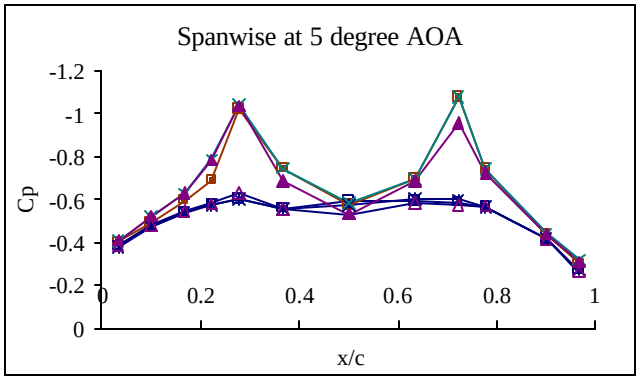

Figure 4.36

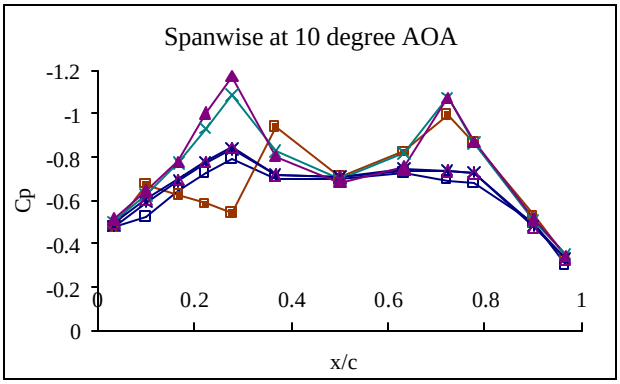

Figure 4.37

Inboard-winglet wing	■ p_∞ = 0.2	* 0.7	▲ 1.2
Conventional wing (ref)	□ p_∞ = 0.2	× 0.7	△ 1.2

Figure 4.34-4.37 Pressure distribution of the wing in the spanwise direction

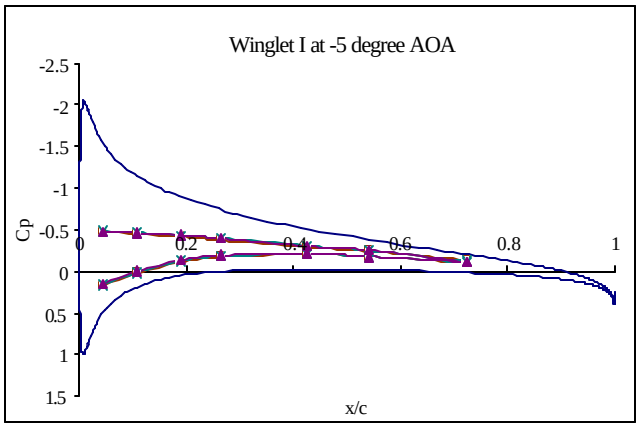

Figure 4.38

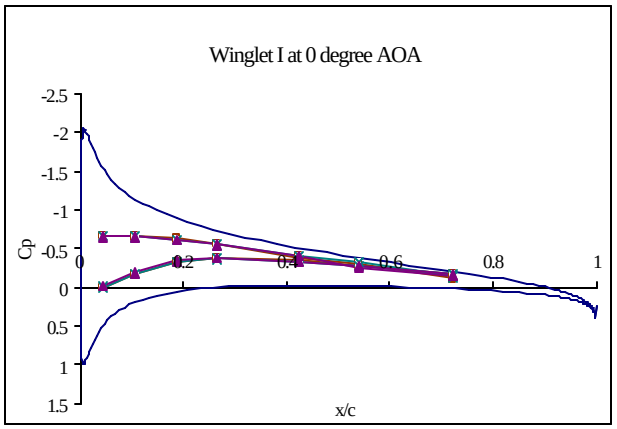

Figure 4.39

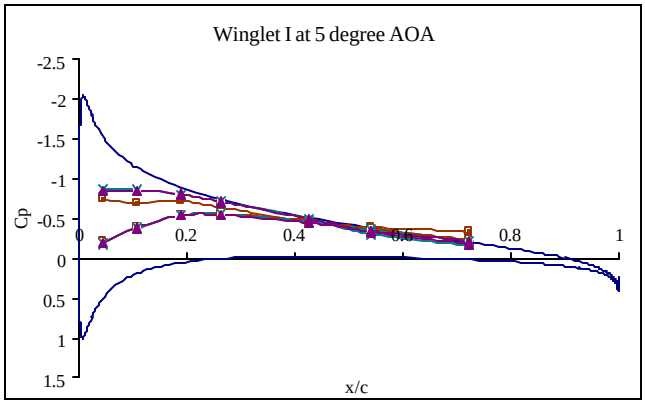

Figure 4.40

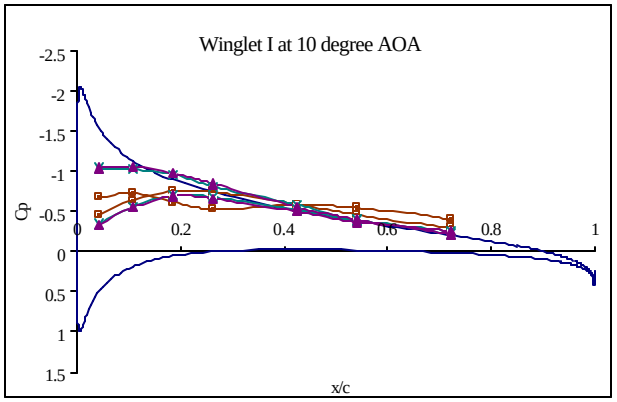

Figure 4.41

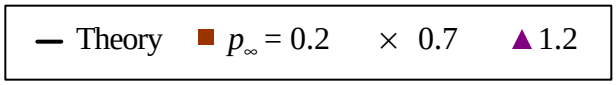

Figure 4.38-4.41 The pressure distributions of the inboard winglet I

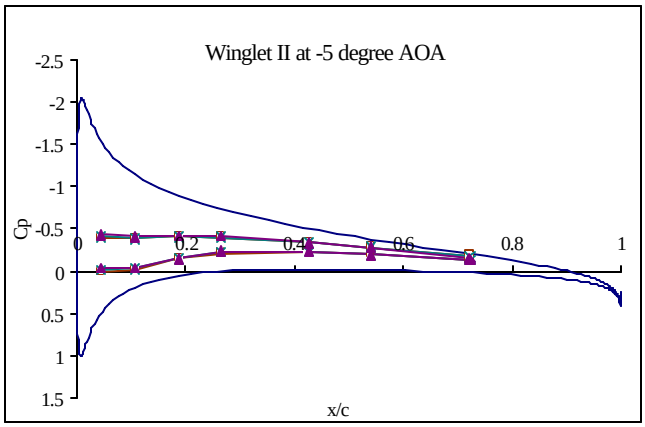

Figure 4.42

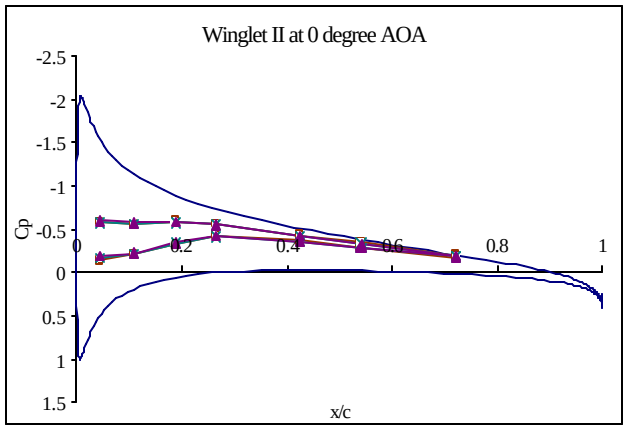

Figure 4.43

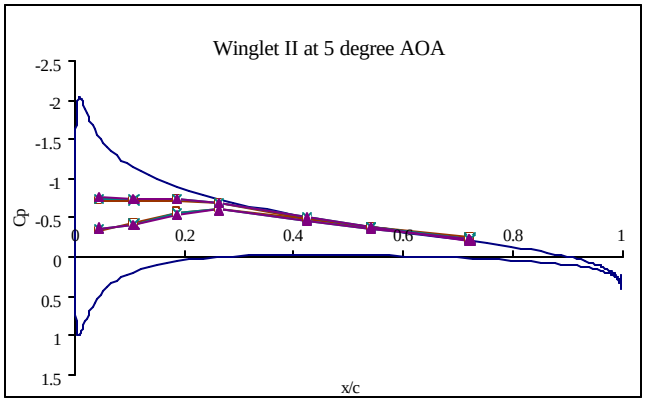

Figure 4.44

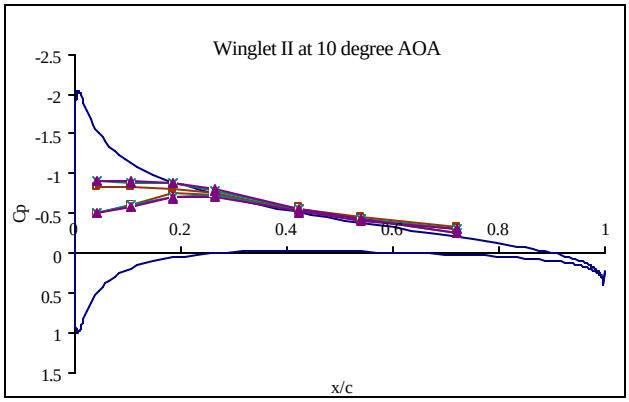

Figure 4.45

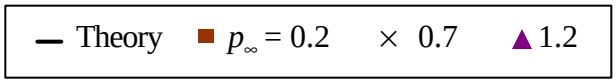

Figure 4.42-4.45 The pressure distributions of the inboard winglet II

4.1.2 Pressure Coefficients at Power-On Condition

To investigate the influence of propeller-induced flow on an inboard-winglet flow field, a second set of experiments was conducted with a similar procedure to the first one for both inboard-winglet and conventional wings. Results were plotted as pressure coefficients versus both chordwise (x/c) and spanwise (y/b) directions to examine any variation in induced flow creating for inboard and outboard sections of the wing as well as any effect caused by the presence of the winglets. The experiment was run at 3 freestream velocity conditions, and at a static condition to observe the propeller flow pattern. In addition to a comparison with the vortex panel estimation for a NACA0012 airfoil (solid lines in the plots), the results from the power-off condition were used to demonstrate the induced-flow effect in some sections. Experimental aerodynamic coefficient data by Grissom and Henry (Grissom and Henry, 2000) was also studied to assist in the pressure coefficient data interpretation.

When considering the pressure coefficient over the wing at a static condition, it could be seen as two separate parts, the outboard and inboard sections. The outboard pressures showed little effect from the small-induced flow inside the winglet channel. On the other hand, the inboard results present interesting pressure distribution formation on the influence of the propeller over the symmetric sections 4 and 6 as shown in Figure 4.46 – 4.49. Having opposite signs for the pressure coefficient values on section 4 and 6 could be a result of unsymmetrical flow from the propeller creating reverse flow in one side. This data varies with angles of attack since the sign of the pressure coefficients for these sections is inconsistent. The pressure coefficients show a positive sign for section 4 at 5 and 10-degree AOA and a negative sign at 0-degree AOA. However, both sections have negative pressure coefficients at the –5 degree AOA as shown in Figure 4.48. For the middle section (section 5), at –5 and 0 degree AOA, the pressure coefficient decreases along the line whereas at 5 and 10 degree AOA, it increases. It may result from the fact that at higher angle of attack the motor mounting structure became an obstacle and decelerated the flow.

Figures 4.54-4.85 show the plots of pressure distributions for the same eight wing sections in the power-off condition. Some examples for the pressure coefficient comparison between the inboard-winglet wing with and without propeller effect were shown in Figures

4.50-4.53. They indicate that the pressure coefficients barely change from those of the non-propulsive force model for the outboard area far from the winglets for all angles of attack and freestream velocities. Figure 4.54, 4.55, 4.62, 4.63, 4.70, 4.71, 4.78 and 4.79 show the pressure distributions on the left outboard part of the wing (section 1 and 2). The distribution comparison to 2D theory is similar to the power-off condition comparison. A possible explanation is that the flow induced by a propeller was blocked by the winglet; hence the flow in an outboard neighbor experienced no propeller-induced effects. Noted in Figures 4.56, 4.65, 4.72 and 4.80 of section 3, dissimilarity in the pressure distribution at different dynamic pressures slightly appears in the plot at 5 and 10-degree AOA when the dynamic pressure of 0.2 inches of water plots somewhat vary from the rest. There was a separation bubble at a quarter chord of the plot of a dynamic pressure of 0.2 inches of water at 5 degree AOA. The entire separation at 10-degree AOA follows the pattern that occurred in the power-off condition with a difference seen later in the spanwise pressure distributions. Hypothetically, a generation of lift on the wing in propeller-induced flow can cause an alternation to the winglet flow field providing higher flow speed over section 3 and even a separation flow.

Inside the winglet channel, the pressure distribution formations are still similar to those of the power-off condition with an exception at the dynamic pressure of 0.2 inches of water. Apparently, an increase in absolute value of pressure coefficients for that condition appeared in all three sections of the inboard part as shown in Figures 4.57-4.59 for –5 degree AOA, Figure 4.65-4.67 for 0 degree AOA, Figure 4.73-4.75 for 5 degree AOA and Figure 4.81-4.83 for 10 degree AOA. The plots also show that the pressure coefficients were equally changed in every measurement point along a chord line giving the same amount of velocity increase over the wing surface due to the propeller-induced flow. At higher freestream dynamic pressures, the effect of the induced flow was barely visible in the chordwise distribution plots. According to the momentum conservation theory, the induced velocity decreases as the freestream velocity is increased at specific thrust (Roskam, 1997). This implied that the velocity change from the propeller induced-flow at dynamic pressure of 0.7 and 1.2 inches of water is too low to impact the pressure coefficient over the wing. When considering the middle section 5, the shift located around 0.2-0.3 x/c in chordwise pressure distribution only appeared at -5 and 0-degree AOA (Figures 4.58 and 4.66). The

possible explanation comes from the plots at static conditions (Figures 4.46-4.49) when they show that the propeller significantly increased the flow velocity at the rear of the wing at low angles of attack as mentioned above. Comparing to the power-off condition, the laminar separations reduce as a result of increasing flow velocity magnitude.

Resembling the left outboard part of the wing, the right outboard part was also blocked from the influence of propeller-induced flow by the winglet as shown in Figures 4.60, 4.61, 4.68, 4.69, 4.76, 4.77, 4.84 and 4.85 for both section 7 and 9. Hence there was no serious difference in the pressure distributions at the 0.2 inches of water freestream condition from the rest or the power-off condition. However, it is interesting to see that at section 7 (Figures 4.60, 4.68, 4.76 and 4.84), a laminar separation bubble of the low speed plot moves forward as an angle of attack increases similar to the power-off condition.

The effect of propeller-induced flow on the different parts of the wing is definitely more emphasized when examined from the spanwise pressure distribution in Figures 4.86-4.89. A slight difference inside the winglet channel between the dynamic pressures of 0.7, and 1.2 inches of water condition is more visible on these plots, which indicated evidence of a small-induced flow at the dynamic pressure of 0.7 inches of water condition. The plots show the significant effect of the winglets since the conventional wing's pressure distribution varies in all sections whereas the inboard-winglet's wing only varies inside the channel. The difference of pressure distributions due to the effect of induced flow inside the channel varies very little to the variation of angle of attack. In addition, the comparisons between the power-on and off condition from Figure 4.90-4.93 shows that the pressure coefficients at the dynamic pressure of 1.2 inches of water, seem to experience no induced flow, which somewhat varies by a presence of a propeller-driving unit. For the 10-degree AOA plot (Figure 4.93), the flow characteristics at section 3 (5^{th} spanwise tap from the left), while still separating, were enhanced by the effect of propeller-induced flow to the winglet.

The pressure distributions over the winglet surface support a remark on the winglet effect that the variation in flow characteristics due to propeller-induced flow is only restricted to a wing area inside the winglet channel. Similar to the wing pressure distributions, Figures 4.94-4.97 show the data on winglet I equally shift at every inside-surface point (lower curves) for the pressure measurement at the dynamic pressure of 0.2 inches of water. The only difference is at 10-degree AOA when the outboard surface shows

an effect from the wing flow separation. The shape of the winglet II pressure distribution in Figure 4.98-4.101 are the same as winglet I without separation. Therefore, besides the change at the lowest flow speed conditions, the distribution patterns are approximately same as the power-off condition.

The existence of propulsive force on the inboard-winglet wing improves the lift characteristic of the wing (Grissom and Henry, 2000). For the pressure measurement data, the high mounting of the pusher propeller produces additional suction on the upper surface; as a result, the lift force on the wing area inside the winglet increases depending on the freestream velocity and thrust setting. Moreover, from the plots, the flow on the outboard part of the wing is likely to stall before an inboard part with its sensitivity to low Reynolds number of the outboard area near the winglets. This gives an unusual stall characteristic that, instead of smoothly dropping off at maximum lift coefficient, the lift curve is almost flat at its peak before gradually declining (Grissom and Henry, 2000). However the change in pressure distribution also gains a greater pressure drag and greater skin friction drag due to the additional structure. A setting of the winglet at zero deflection gains no advantage to the concept as it can be seen that the conventional wing with a propeller will also provide additional suction pressure similar to the inboard-winglet wing. A 5-degree deflection of the winglets helps generate a negative drag to counter those extra drags, which also vary with the wing angle of attack. The lift to drag ratio of the inboard-winglet wing is more enhanced and closer to that of the channel wing when having the 5-degree deflection than the one without (Grissom and Henry, 2000).

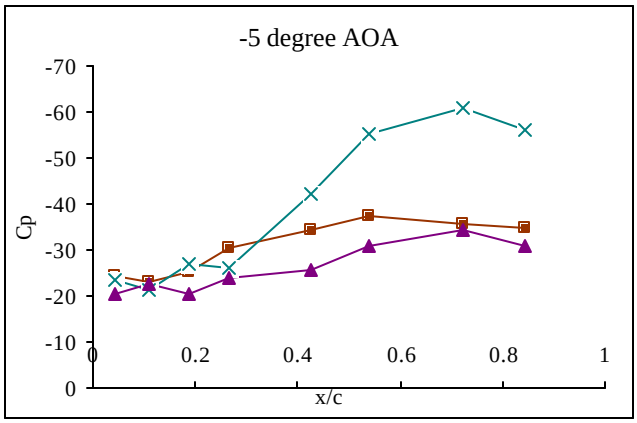

Figure 4.46

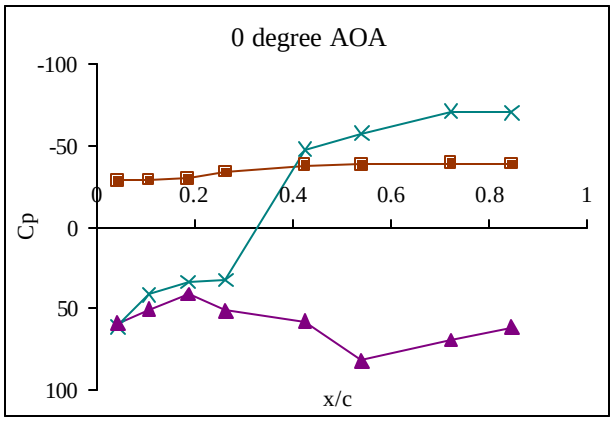

Figure 4.47

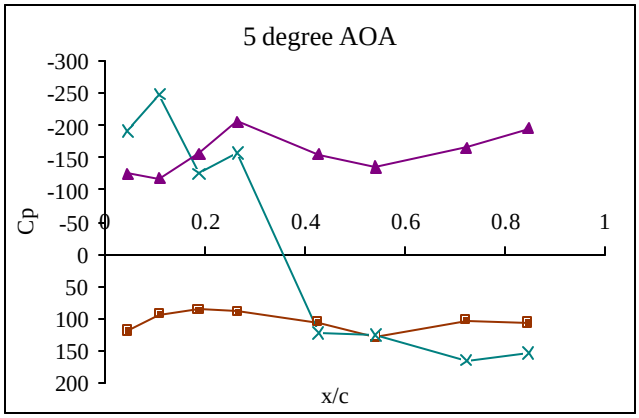

Figure 4.48

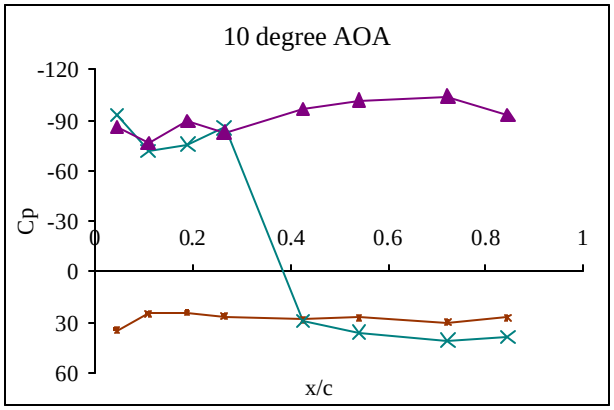

Figure 4.49

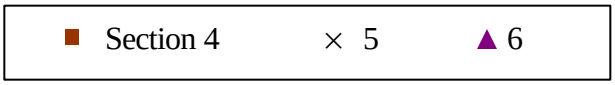

Figure 4.46-4.49 The pressure distributions of the inboard wing sections at static condition

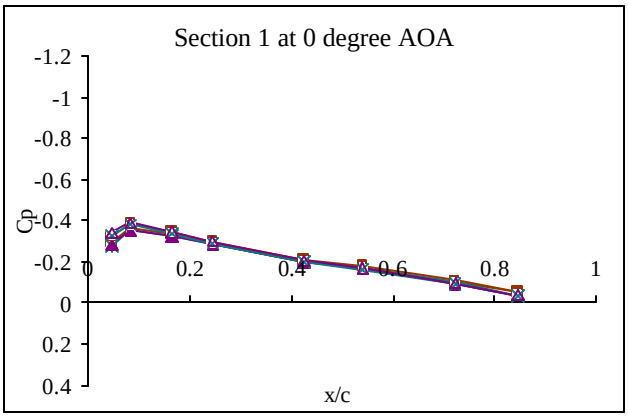

Figure 4.50

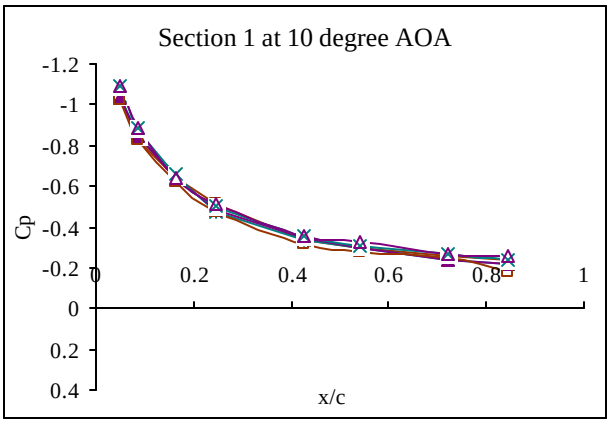

Figure 4.51

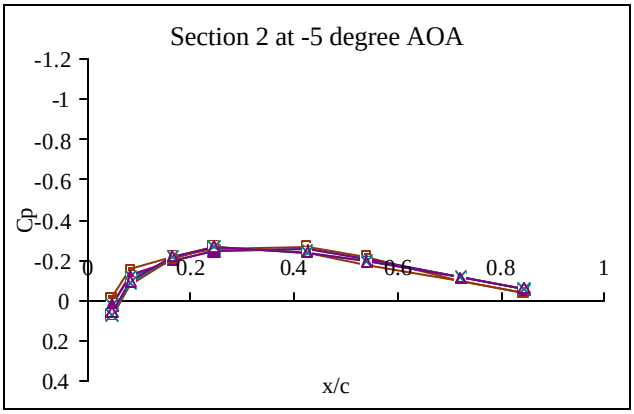

Figure 4.52

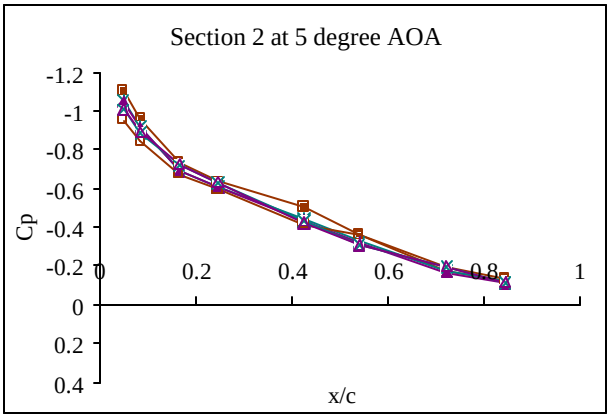

Figure 4.53

Inboard-winglet wing (power-on)	■ p_∞ = 0.2	* 0.7	▲1.2
Inboard-winglet wing (power-off)	□ p_∞ = 0.2	× 0.7	△1.2

Figure 4.50-4.53 The comparison of the pressure distributions at a power-on and off condition

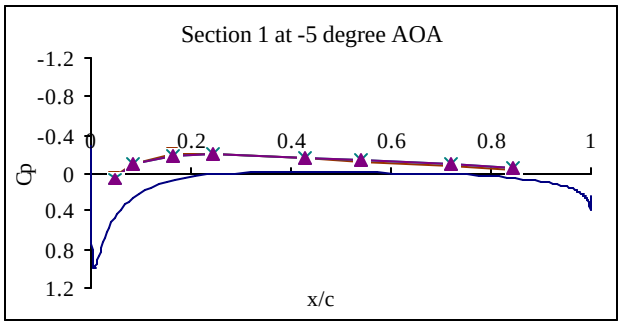

Figure 4.54

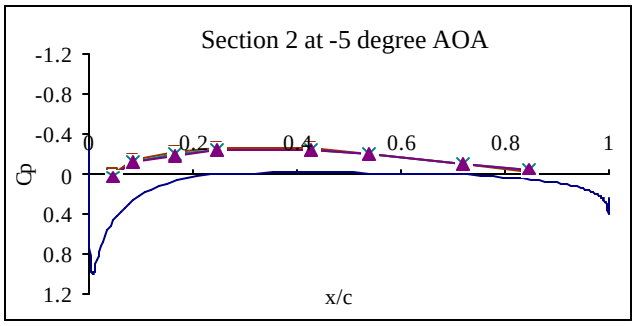

Figure 4.55

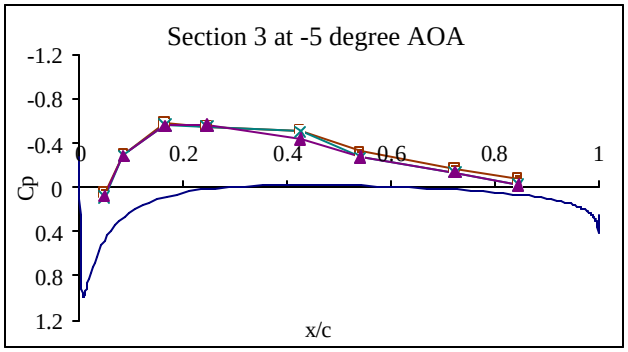

Figure 4.56

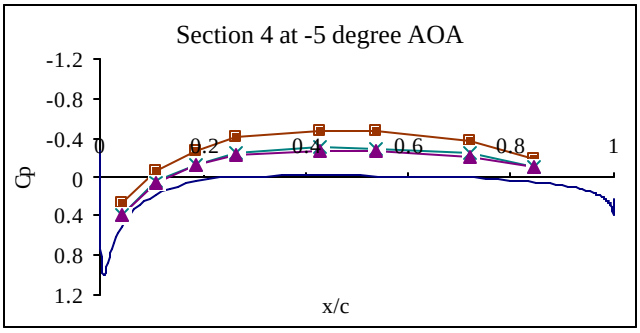

Figure 4.57

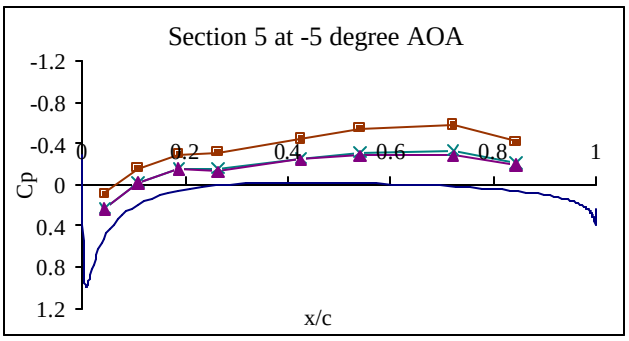

Figure 4.58

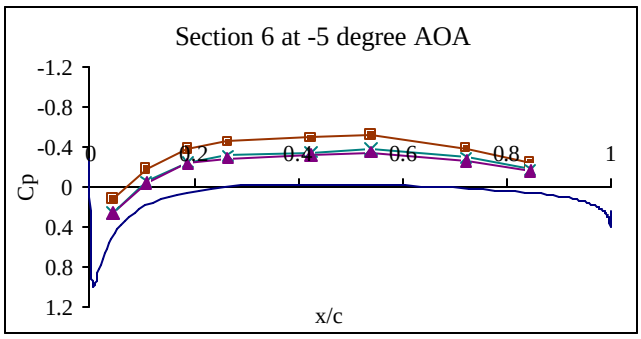

Figure 4.59

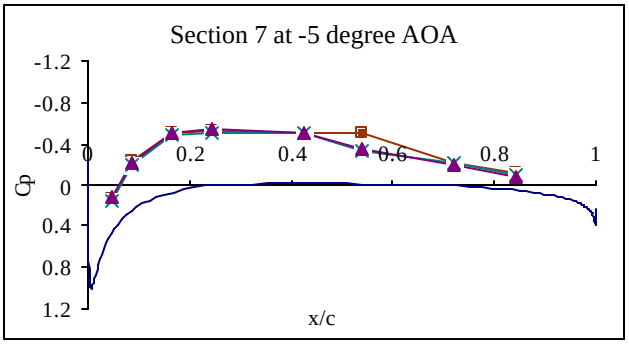

Figure 4.60

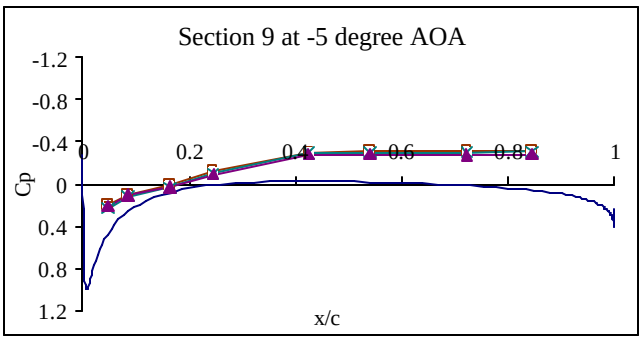

Figure 4.61

Figure 4.54-4.61 The power-on pressure distributions of the inboard winglet wing at -5 degree angle of attack

— Theory ■ p_∞ = 0.2 × 0.7 ▲1.2

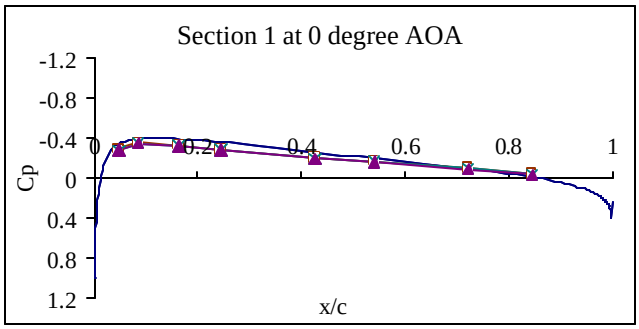

Figure 4.62

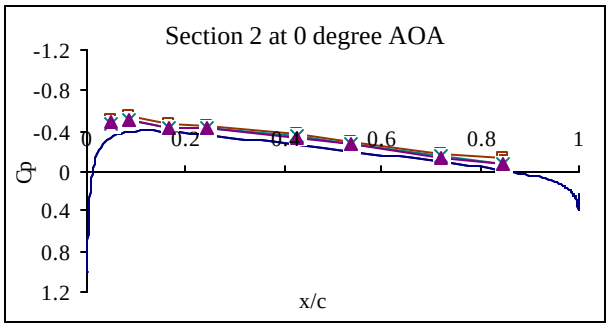

Figure 4.63

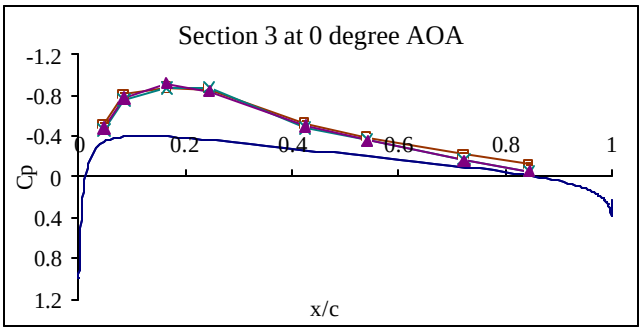

Figure 4.64

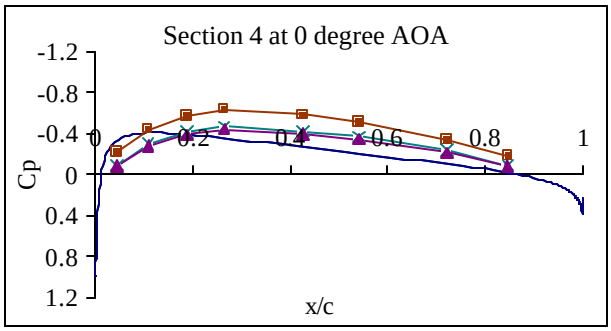

Figure 4.65

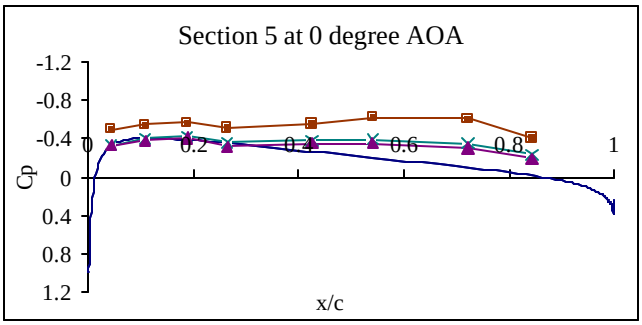

Figure 4.66

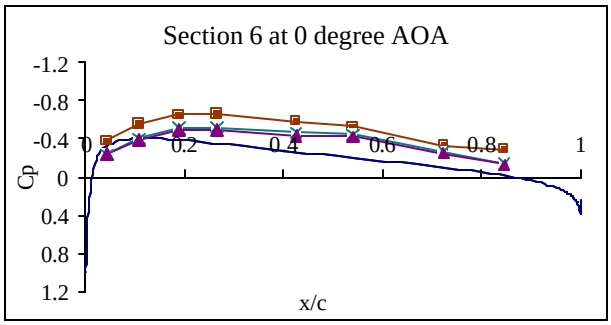

Figure 4.67

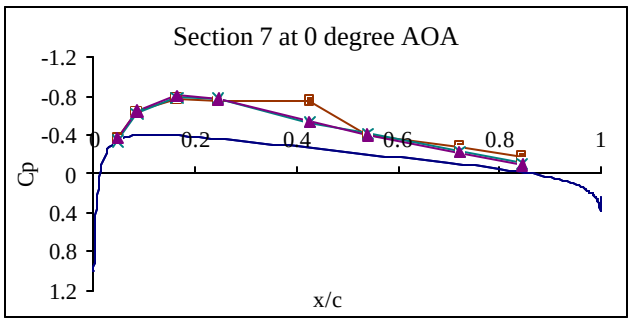

Figure 4.68

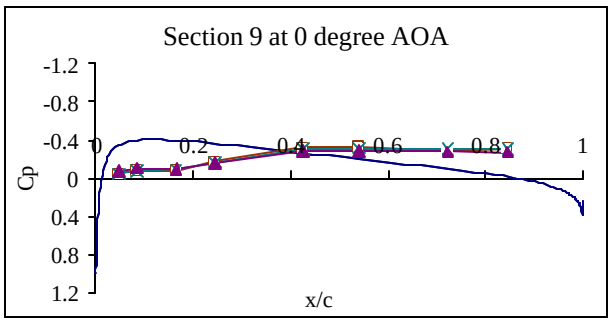

Figure 4.69

Figure 4.62-4.69 The power-on pressure distributions of the inboard winglet wing at 0 degree angle of attack

— Theory ■ p_∞ = 0.2 × 0.7 ▲1.2

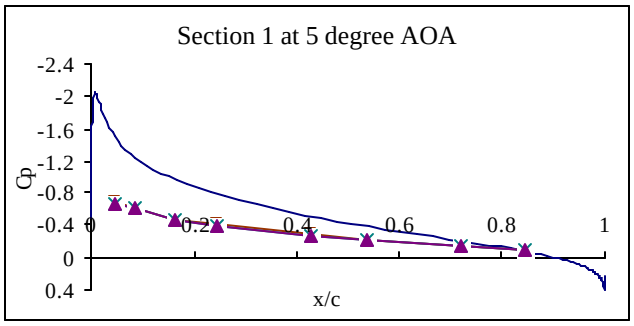

Figure 4.70

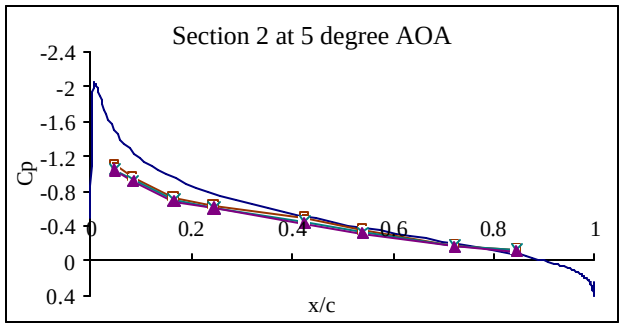

Figure 4.71

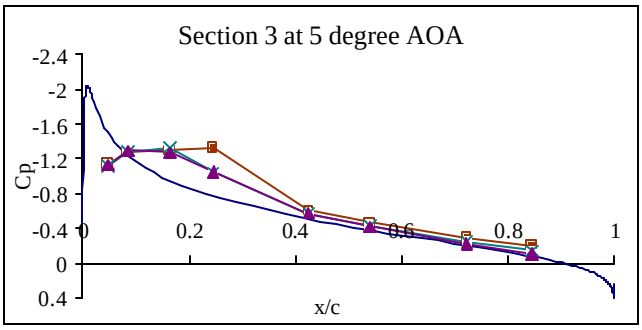

Figure 4.72

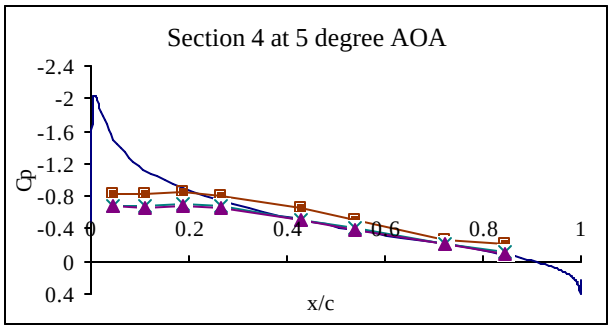

Figure 4.73

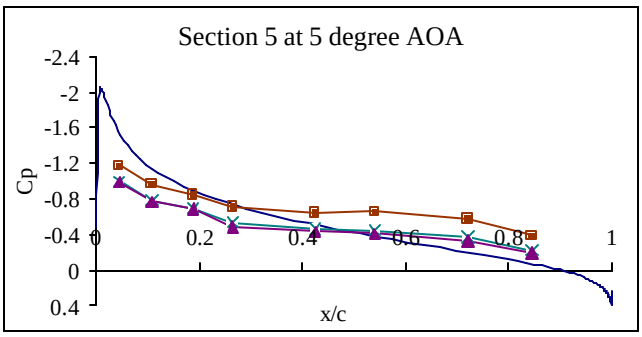

Figure 4.74

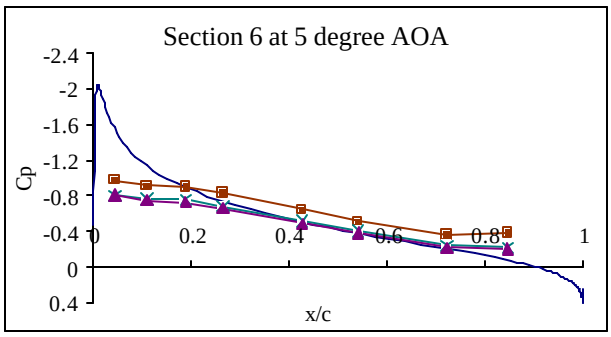

Figure 4.75

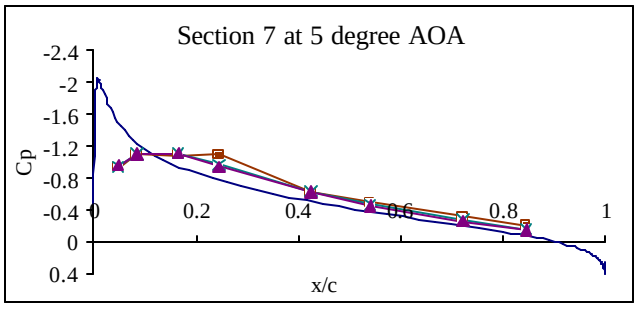

Figure 4.76

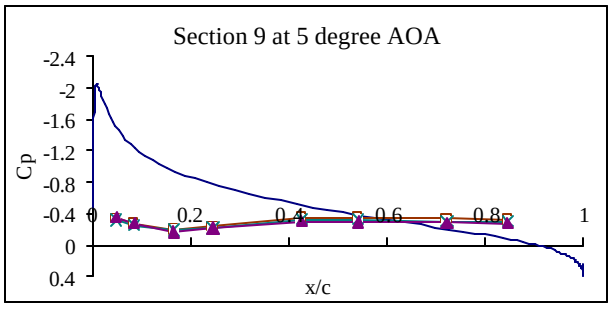

Figure 4.77

Figure 4.70-4.77 The power-on pressure distributions of the inboard winglet wing at 5 degree angle of attack

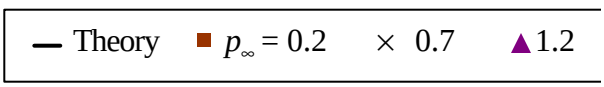

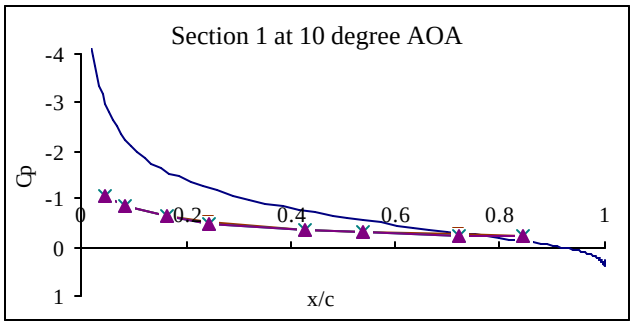

Figure 4.78

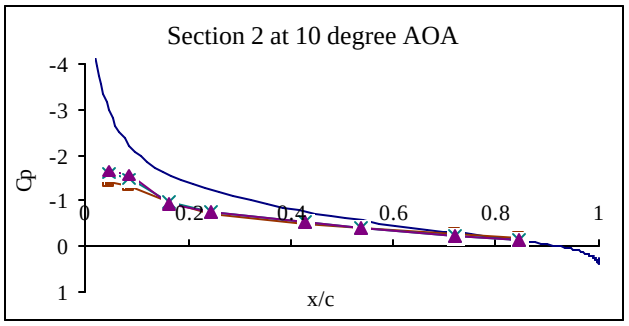

Figure 4.79

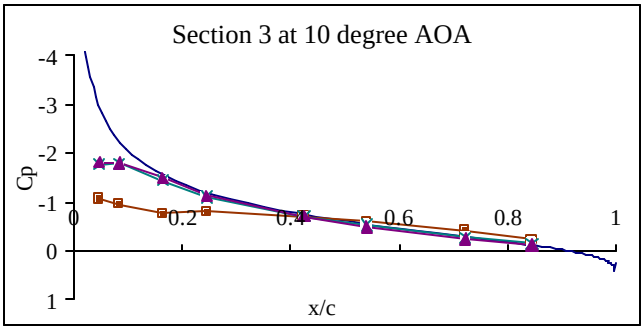

Figure 4.80

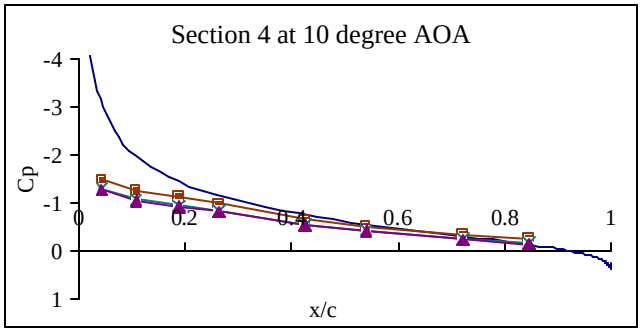

Figure 4.81

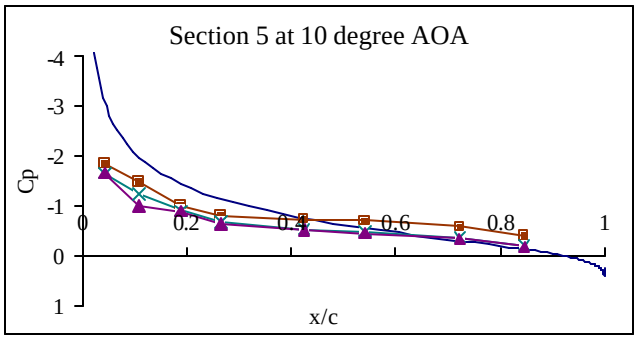

Figure 4.82

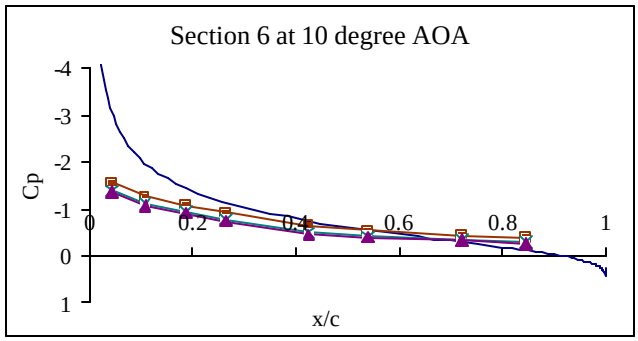

Figure 4.83

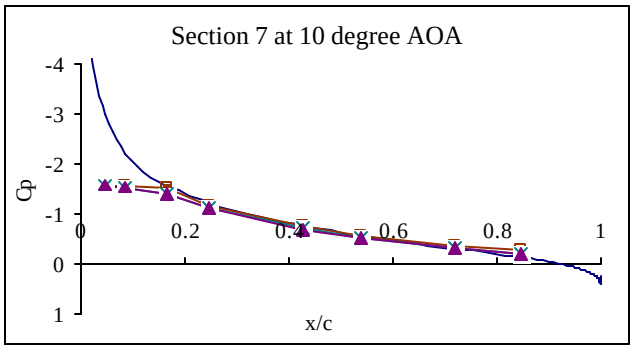

Figure 4.84

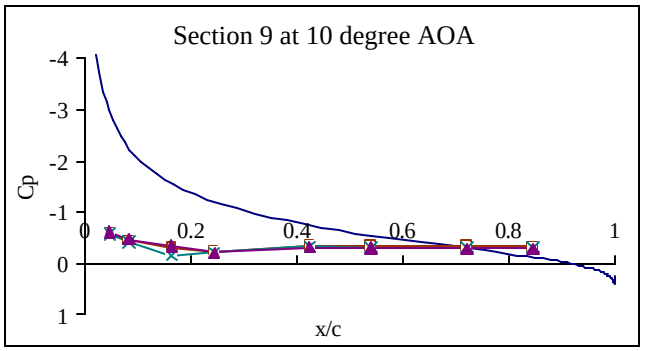

Figure 4.85

Figure 4.78-4.85 The power-on pressure distributions of the inboard winglet wing at 10 degree angle of attack

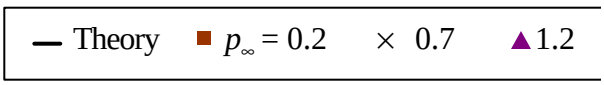

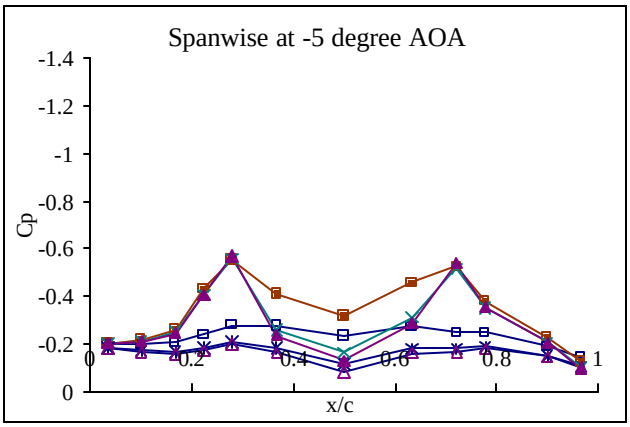

Figure 4.86

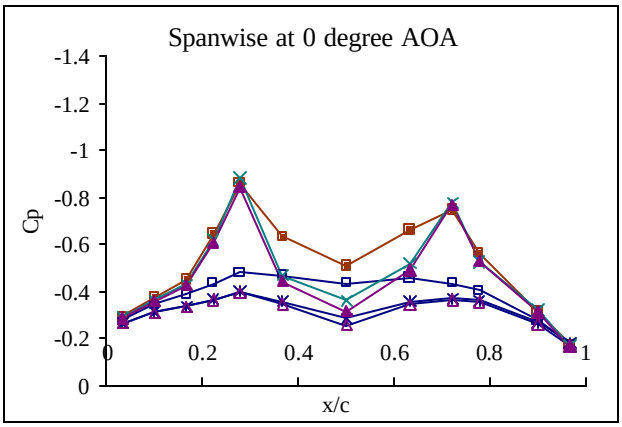

Figure 4.87

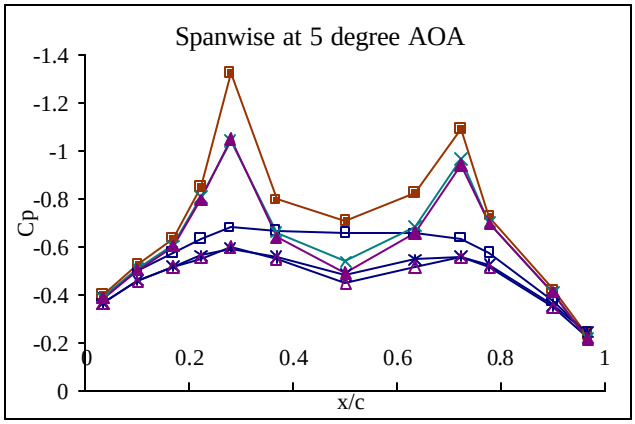

Figure 4.88

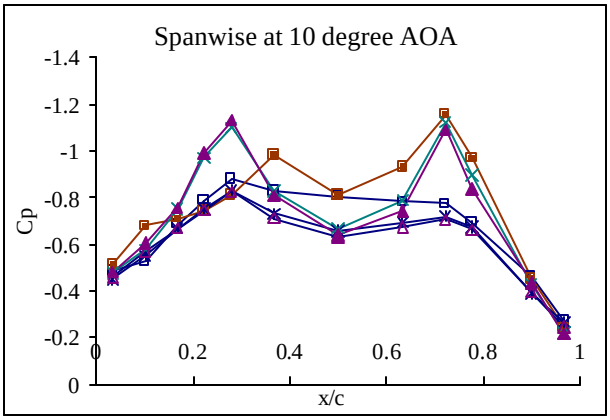

Figure 4.89

Inboard-winglet wing	■ p_∞ = 0.2	* 0.7	▲1.2
Conventional wing (ref)	□ p_∞ = 0.2	× 0.7	△1.2

Figure 4.86-4.89 The spanwise pressure distributions of the inboard-winglet and conventional wing at the power-on condition

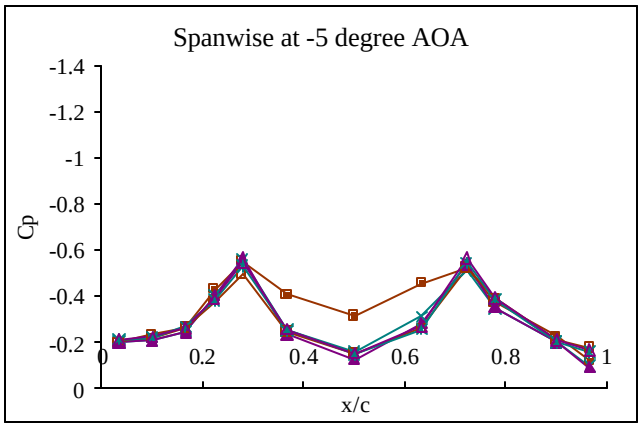

Figure 4.90

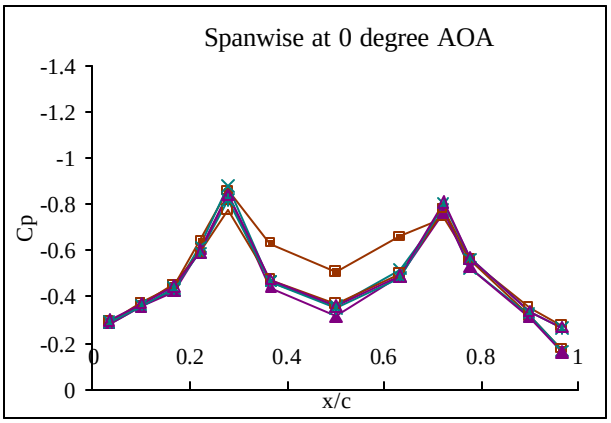

Figure 4.91

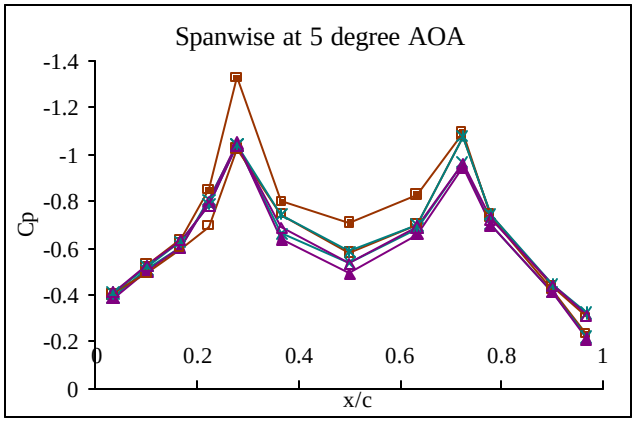

Figure 4.92

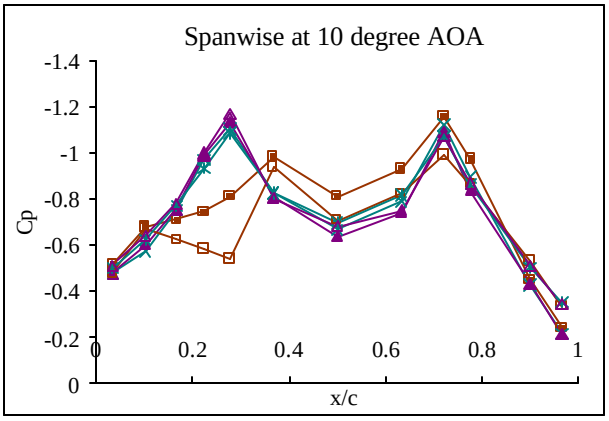

Figure 4.93

Inboard-winglet wing (power-on)	■ p_∞ = 0.2	* 0.7	▲ 1.2
Inboard-winglet wing (power-off)	□ p_∞ = 0.2	× 0.7	△ 1.2

Figure 4.90-4.93 The comparison of the spanwise pressure distributions of the inboard-winglet wing for the power-on and off condition

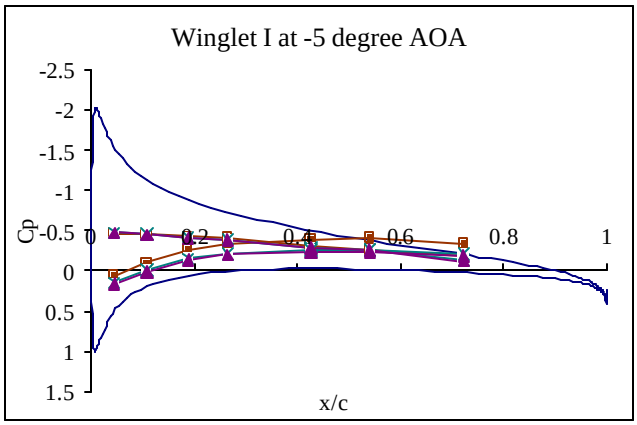

Figure 4.94

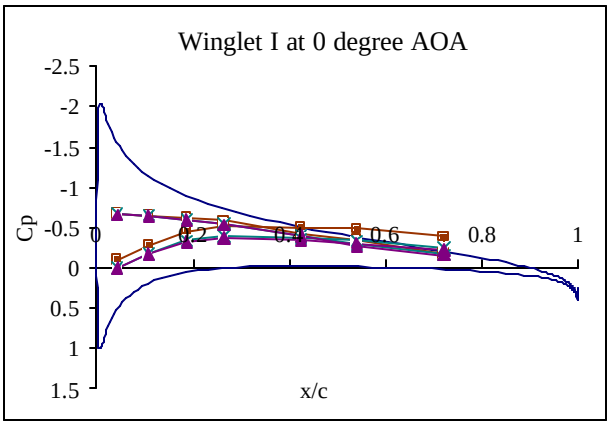

Figure 4.95

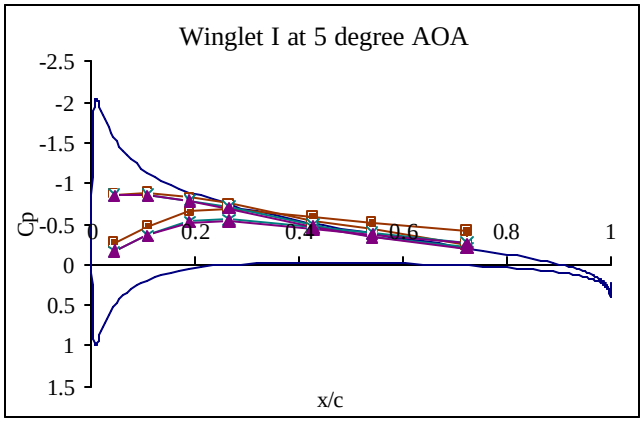

Figure 4.96

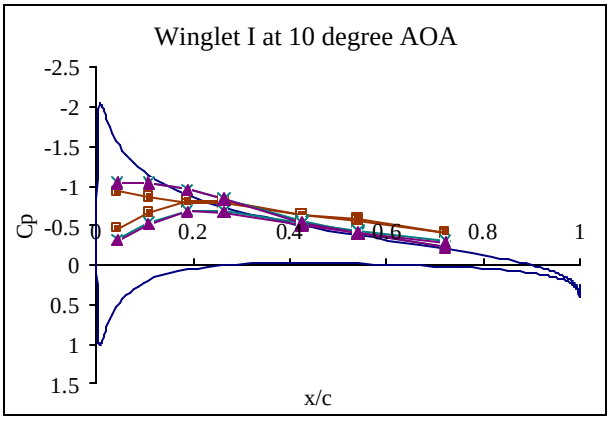

Figure 4.97

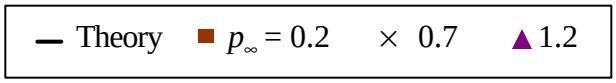

Figure 4.94-4.97 The power-on pressure distributions of the inboard winglet I

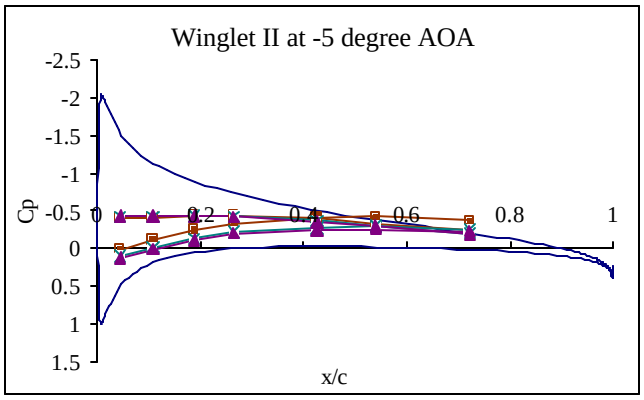

Figure 4.98

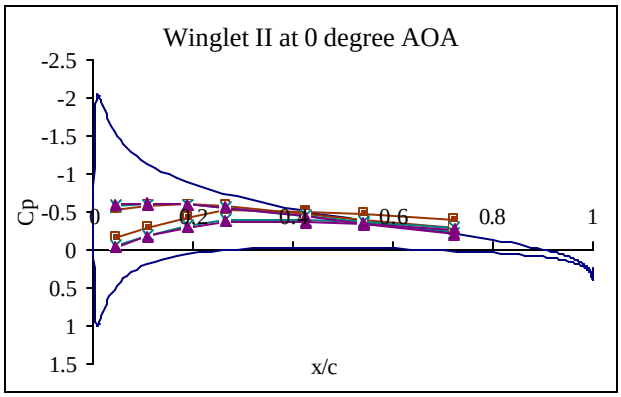

Figure 4.99

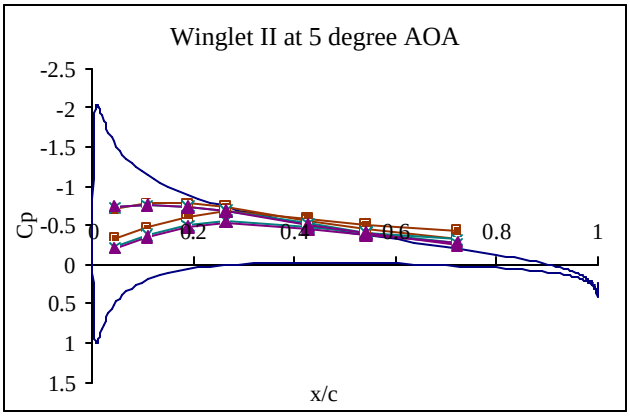

Figure 4.100

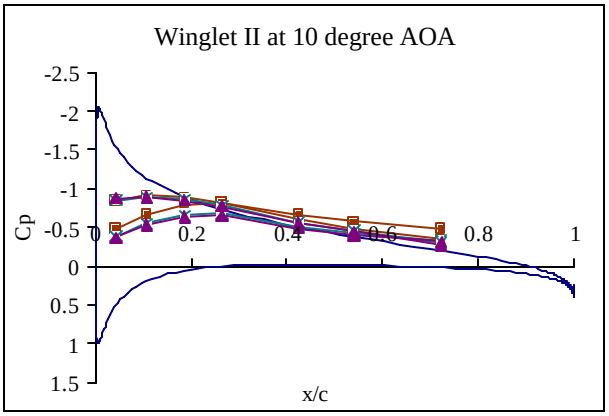

Figure 4.101

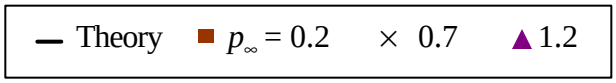

Figure 4.98-4.101 The power-on pressure distributions of the inboard winglet II

4.1.3 Numerical Analysis of Experimental Data for Thrust on the Winglets

To examine quantitative change of inboard-winglet wing characteristics due to the propeller-induced flow effect, the pressure coefficients from the experiment were numerically integrated to find normal and axial force acting on a winglet section. These forces provided a comparable drag component that when pointing to a negative direction, became useful for the wing performance. In a presence of a propulsive force, flow inside a winglet channel was induced without interfering the outboard part; thus a flow field around the winglets was altered, giving a variation in the drag component that improved inboard-winglet utilization.

In the previous discussions, the pressure coefficient plots indicate, by displaying a variation in the plots on an inboard side of the winglets, that the effect of the induced flow only occurred in a case of 0.2-inches-of-water freestream dynamic pressure. The data were calculated for drag coefficients as shown in Table 4.1 at the power-on condition. A minus sign of the results presents a forward direction of the drag component, which is thrust direction. When a wing angle of attack was in a negative lift position, –5 degree, the drag coefficients were positive meaning that the model gained unwanted drag instead of thrust from the winglets. Whereas when the wing had positive lift, the angle of attack of 0, 5, and 10 degree, the winglets produced a thrust component giving the minus sign for the drag coefficients. From the results, the drag coefficients at the dynamic pressure of 0.2 inches of water are smaller than the other two conditions with the only exception at the 10-degree angle of attack of Winglet I because of a separation. This indicates that the propeller-induced flow tends to enhance the thrust created by the winglets and provide better wing performance.

Differences in the results of the increasing thrust, when comparing to average results of non-effected conditions, are variable ranging from 4.4 to 82.3 percent. Therefore, besides a lift distribution over the wing, a defected angel of the winglets clearly has an influence on the thrust variation as well since they did not only vary with the change in the angle of attack. To gain a best advantage from the induced flow in the experiment, the 5 degree deflection in this experimental model is likely more appropriated to the wing at 0 degree angle of attack than the rest as it provided the greatest enhancement. However, without the

induced flows effect, the higher the angle of attack, the larger the thrust component became. Thus, an optimal design of a winglet deflection requires both factors to achieve the better operation of the inboard-winglet.

Table 4.1 Drag coefficients of the winglets at the power-on condition

Wing angle of attack –5 degree		
Freestream dynamic pressure (in. of water)		C_d
Winglet I	0.2	0.00182
	0.7	0.00479
	1.2	0.00435
Winglet II	0.2	0.01121
	0.7	0.01403
	1.2	0.01287
Wing angle of attack 0 degree		
Freestream dynamic pressure (in. of water)		C_d
Winglet I	0.2	-0.01953
	0.7	-0.01108
	1.2	-0.01034
Winglet II	0.2	-0.00420
	0.7	-0.00319
	1.2	-0.00363

Wing angle of attack 5 degree		
Freestream dynamic pressure (in. of water)		C_d
Winglet I	0.2	-0.03327
	0.7	-0.02608
	1.2	-0.02707
Winglet II	0.2	-0.01961
	0.7	-0.01839
	1.2	-0.01917
Wing angle of attack 10 degree		
Freestream dynamic pressure (in. of water)		C_d
Winglet I	0.2	-0.03553
	0.7	-0.04268
	1.2	-0.04338
Winglet II	0.2	-0.03647
	0.7	-0.03267
	1.2	-0.03442

4.1.4 Uncertainties

Since pressure coefficients obtained from primary voltage measurements of two pressure transducers, an approximation of uncertainties in experimental results was developed from parameters of pressure/voltage linear conversion, a slope of a line (m) and a y-intercept (b).

$$C_p = \frac{\Delta P_{measurement}}{\Delta P_{reference}} \tag{4.1}$$

$$C_p = \frac{m_1 V_m + b_1}{m_2 V_{ref} + b_2} \tag{4.2}$$

By given uncertainties in liner parameters, $d\,m_1$, $d\,m_2$, $d\,b_1$ and $d\,b_2$, the uncertainties were calculated from:

$$d\,C_p = \sqrt{d\,m_1^{\,2} + d\,m_2^{\,2} + d\,b_1^{\,2} + d\,b_2^{\,2}} \tag{4.3}$$

The uncertainties presented in Table 4.2 were estimated based on the pressure measurement of the inboard-winglet wing at x/c = 0.425 of the mid-span section for the different freestream dynamic pressures and angles of attack.

Table 4.2 Uncertainties in C_p for the different conditions at x/c=0.425 of the mid-span section

q_∞	C_p uncertainty at AOA = -5°	C_p uncertainty at AOA = 0°	C_p uncertainty at AOA = 5°	C_p uncertainty at AOA = 10°
0.2	0.030	0.035	0.036	0.041
0.7	0.011	0.014	0.017	0.019
1.2	0.010	0.013	0.016	0.019

Apparently, the uncertainties are larger at the low Reynolds number (the freestream dynamic pressure of 0.2 inches of water) whereas approximately are the same at the higher Reynolds numbers. The percent differences range from 3-6%.

An uncertainty of the drag coefficient calculation from the experimental data was evaluated for the pressure coefficient uncertainties at the wing angle of attack of 5 degree

and the freestream dynamic pressure of 0.7 inches of water for winglet I section. A result is 0.0019, which is approximately 7.2%, while the uncertainty approximation of the pressure coefficient measurement at this condition is only 3.6%

4.2 Discussion of the Inboard Winglet Application on the Pegasus II

By examining the experimental data, the calculated thrust indicates that the application of the inboard winglet as a channel for a propeller-induced flow has a potential to enhance an aircraft performance when setting at an appropriate configuration. In the performance estimation of the Pegasus II, a presence of vertical stabilizers at the tips of an inboard wing, acting like the inboard winglets, has an unconventional influence on 2 performance parameters, wing lift and induced drag, which is normally unable to approximate the influence by a standard approach on conceptual design phase. Thus, for a more accurate approximation for the Pegasus II's performance, a lift coefficient and an effective aspect ratio, considered as two essential data input in performance equations, were determined by the approaches prior discussed in chapter 3 to include a change in the lift and the drag from the inboard-winglet application, respectively.

4.2.1 Numerical Analysis of the Wing Lift Coefficient from the Experimental Data

Similar to the numerical analysis of the winglet for the thrust, a calculation to determine a proportion of increasing lift was the numerical integration of a pressure distribution over the wing's mid-span section, section 5. Since the experiment only provided the pressure distribution of the upper surface, resultant forces acting on the wing were calculated based on the data at 5-degree angle of attack to represent the distribution over the upper surface while the data from the power-off conventional wing at –5-degree angle of attack was considered as the lower surface data of the 5-degree angle of attack with an assumption that the flow characteristic on the lower side was unaltered by the high-mounting propeller. Also, the pressure distributions at these conditions were somewhat complete without any severe separation to limit the use of the data for a precise result.

Table 4.3 shows calculated lift coefficients on both power-off and on conditions with percentage differences of the results. The lift coefficient at the freestream dynamic pressure of 0.2 inches of water for the power-on condition is 0.59356687, which rather close to 0.541052 of a 2D-lift coefficient for the NACA0012 airfoil (Abbot and Doenhoft, 1959).

This helps verify the assumption made in the simplified lift coefficient calculation for the Pegasus II that the inboard section lift coefficient could be approximated as a 2D-lift coefficient of its airfoil.

The percentage differences between the power-off and on condition decreased as the propeller induced flow effect became less important at the higher freestream velocity. At the dynamic pressure of 0.2 inches of water, the difference was used for predicting the change in the lift coefficient inside the winglet channel in order to apply it to the approximation of additional thrust from the inboard winglets as mentioned in section 3.3. The thrust coefficients (T_c) were calculated by the so-called propeller performance charts for the experimental model at the 0.2 inches of water dynamic pressure condition and the Pegasus II at takeoff condition as shown in Table 4.4. Assumed constant, the upper surface lift fraction, given from calculating the experimental percentage different of 53.71 and the thrust coefficient in Eqn. (3.13), provide the 73.2 % increase in the lift coefficient at the thrust coefficient of the Pegasus II. This result would be used in the next section.

Table 4.3 Lift coefficients of the mid-span section at the power-off and on condition

Dynamic pressure (in. of water)	C_l		Percent difference
	Power-off condition	Power-on condition	
0.2	0.386	0.594	53.71
0.7	0.350	0.399	14.24
1.2	0.333	0.357	7.28

Table 4.4 Calculation of the thrust coefficients for the experimental model and the Pegasus II

Input:	**Experimental model**	**Pegasus II**
Freestream velocity (ft/s)	31.07	86.184
Shaft horsepower	0.804	359.232
Propeller rpm	6820	2700
Number of blades	2	3
AF [11]	100	100
C_{L_i}	0.5	0.5
Output:		
T_c	2.729	3.854

4.2.2 Results of Thrust Approximation from the Winglets

According to the Pegasus II design, the vertical stabilizers were also utilized as the inboard winglets. The additional thrust at an optimal winglet configuration was estimated based on a takeoff condition since the inboard-winglet concept is more effective in a low-speed and high-thrust region. From section 4.2.1, the lift coefficient of the inboard wing, $C_{l,1}$, in Eqn. (3.16) had 73.2% increase from a regular 2D lift coefficient providing strong energy vortices needed for the winglets. To acquire maximum thrust due to the winglets, a twist-angle distribution of the winglets relative to the free stream should be similar to Figure 4.102. However, this analytical approximation excluded real viscous effect such as stall phenomena given that a local effective angle of attack in the calculation could go beyond an actual stall angle. Thus, the twist angle was restricted by the stall angle of the NASA0008 airfoil, which is 14.8 degree. Thrust calculated from this approach for each winglet was equaled to 18.1 lbs providing a total additional thrust of 36.2 lbs from both side. An effect of

[11] For typical light aircraft, the blade activity factor is 100. (Raymer, 1989)

this thrust would be applied to the performance estimation via an effective aspect ratio of the wing, which could be estimated by a variation in a lift to drag ratio, L/D. Without the optimized winglets, the Pegasus II's L/D was approximated to be 2.69 while the application of the inboard winglets provided the L/D of 2.83. This enabled the improvement of 5.2% in the L/D, which is less than 20% improvement of typical winglets (Raymer, 1989).

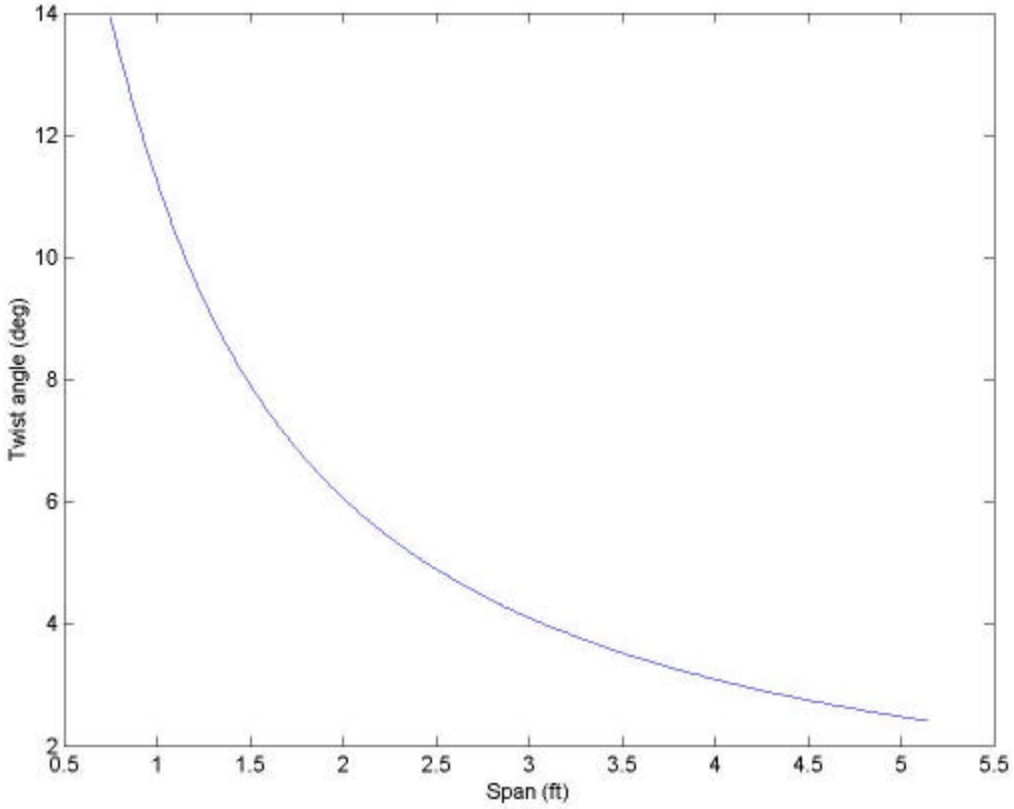

Figure 4.102 Optimal twist angles of an inboard winglet relative to the freestream velocity

4.2.3 Result of the Simplified Lift Coefficient Approximation for the Pegasus II

To obtain the wing maximum lift coefficients for the Pegasus II performance estimation, the wing was considered as a combination of 2 separate wings, the 2D inboard wing of the GA(W)-1 airfoil and the 3D outboard wing of the GA(W)-2 airfoil. In this approximation, the maximum lift coefficients for 3 flight conditions, stall, takeoff, and cruise speed were required for the estimation since they varied with Reynolds numbers and high-lift device's configurations.

For the outboard wing of 10-feet span and 5.2-feet chord, its lift coefficient would be improved by an application of a high-lift device during takeoff and landing. Maximum 2D lift coefficients of the GA(W)-1 as listed in Table 4.5 were used in the calculation for 3D analysis from Nicolai's approach shown in Appendix A. When higher lift was needed, a plain flaperon was employed to the outboard section with an airfoil chord ratio of 0.5 and a flapped wing area ratio of 0.65. Three deflected angle of the flaps, 10, 20 and 40 degree were examined from the stall condition for the maximum lift coefficients and maximum angles of attack applied during takeoff and landing as given in Table 4.6.

Table 4.5 2D maximum lift coefficient of the GA(W)-2 (McGhee, et.al., 1977)

Flight condition	Max 2D lift coefficient
Cruise	2.08
Takeoff	1.97
Stall speed	1.84

Table 4.6 Maximum 3D lift coefficients and angles of attack for various flap deflections

Flap deflection (degree)	Max. 3D lift coefficient	Max angle of attack (degree)
0	1.656	18.68
10	1.995	17.48
20	2.238	16.37
40	2.356	14.10

The maximum angle of attack for the outboard wing restricted the maximum angle of attack for the inboard wing since the entire wing was originally designed without any twist. A flap deflection for takeoff was selected to be 20 degree while full flap deflection, 40 degree, was for landing. The 2D lift coefficients of the GA(W)-1 airfoil at the same angles of attack as the outboard wing were listed in Table 4.7.

Thus, the total maximum lift coefficients, calculated based on Eqn. (3.23), are presented in Table 4.8. These lift coefficients would be used in for the Pegasus performance estimation in the next section.

Table 4.7 2D lift coefficient of the GA(W)-1 at selected angles of attack (McGhee, et.al., 1980)

Flight condition	Angle of attack (degree)	2D lift coefficient
Cruise	18.68	2.02
Takeoff	16.37	1.76
Stall speed	14.10	1.68

Table 4.8 Total maximum lift coefficients for different flight conditions

Flight condition	Flap deflection	Max 3D lift coefficient
Cruise	0	1.850
Takeoff and landing	20	1.982
Stall speed	40	1.995

4.3 Comparator Aircraft Performance and Sensitivity Study

Representing diverse design objectives, 4 selected models of dual and single-mode vehicles, Pegasus II, LaBiche FSC-1, Cessna 182 and Cirrus SR22, were evaluated based on the requirements from the PAVE program for their aircraft performance. The resulting comparison and a sensitivity analysis of the Pegasus II comparing it to the Cirrus SR22 would enable a better understanding of the inboard-winglet application to the roadable aircraft and the effect of the predictions of the design parameters, such as lift coefficient of the inboard-winglet concept, to the performance.

The results, listed in Table 4.9, indicate that all models meet the PAVE and FAR constraints and that the Pegasus II performs comparably to the others. Wing loadings of the dual-mode vehicles are slightly higher than those of the conventional aircraft since the size limitation in them essentially dictates a low wing area. Thus, the stall speeds are also higher and nearer to the FAR limit. The dual-mode vehicle also has a lower power loading compared to the Cessna 182. The high rate of climb and cruise speed of the LaBiche indicate the results of its considerably larger engine power. For the Pegasus II, even though its rate of climb is high due to the same reason as the LaBiche, its cruise speed is lower because of a drag penalty; both profile drag and induced drag from its low aspect ratio wing. However, in the comparison between the 2 dual-mode vehicles, a severe weight penalty of the roadable aircraft in the Pegasus II, unlike the LaBiche, was somewhat reduced by a utilization of the new uncomplicated wing concept.

Table 4.9 Aircraft performance results of 4 comparator vehicles

Description		Constraints	Pegasus II	LaBiche	Cessna 182	Cirrus22
Dimension	Length (ft)	22	20	10.5 (wheel base)	29	26
	Height (ft)	7	6.96	-	9.33	9.2
	Roadable width (ft)	7	7	6.67	-	-
	Wing span (ft)	-	17	32.13	36	38.5
	Wing Area (ft^2)	-	111.5	130.34	174	144.9
Takeoff gross weight (lbs)		-	2766	3440	2945	3285
Engine HP			359.232	445	230	310
Fuel weight (lbs)		-	372	185	248	235
Wing loading (lb/ft^2)		-	24.8	26.4	16.9	22.7
Power loading (lb/hp)		-	7.7	7.7	12.8	10.6
Takeoff ground roll (ft)		2000	474	667	501	786
Takeoff with 50 ft clear (ft)		3000	1034	1272	975	1380
Landing ground roll (ft)		2000	731	720	464	668
Landing with 50 ft clear (ft)		3000	1732	1511	1096	1451
Service ceiling (ft)		-	18378	34039	25416	30688
Absolute ceiling (ft)		-	19337	35838	27589	32769
Max speed at 80% HP (kts)		100	180	258	137	185
Stall speed w/flap at SL (kts)		61	60	61	48	58
Stall speed clean at cruise (kts)		-	71	87	61	77
Max rate of climb (fpm)		-	2254	2638	1522	2002

For the sensitivity analysis 5 design parameters; maximum lift coefficient, profile drag coefficient, empty weight, specific fuel consumption, and engine horsepower, were studied for their effect on aircraft performance by varying each of these parameters. They were decreased by 10% in the first three parameters and increased by the same amount in the last two to examine positive performance results. Percentage differences in takeoff distance, a stall speed, a cruise speed, and a maximum rate of climb at sea level are displayed in Figures 4.103 – 4.106. It is common to see that the empty weight is the most vital parameter for the takeoff distance (Figure 4.103). Also, the same can be said for maximum lift coefficient, while the profile drag coefficient variation barely affects the takeoff performance. The variation in the maximum lift coefficient also influences the drag due to lift and this has more influence than the profile drag. In the Pegasus II, the new wing concept is likely to enable a significant benefit to its performance since it helps reduce the empty weight and increase the maximum lift coefficient. Apart from a sensitivity of specific fuel consumption, the Pegasus II takeoff distance is less sensitive to variations in the rest of the parameters than the Cirrus SR22.

Figure 4.104 indicates that the stall speed sensitivity only varies with the empty weight and the maximum lift coefficient. However, the gain of the lift coefficient in the Pegasus II is less important to the stall speed than the Cirrus SR22 since the wing area of the Pegasus II was limited.

Obviously, the cruise speed is unchanged by the variation of the maximum lift coefficient as shown in Figure 4.105. Unlike the takeoff and stall speed sensitivity, the Pegasus II's cruise speed is more sensitive to some of these parameters than the Cirrus SR22's. The most important parameters, as expected, are the profile drag coefficient and the engine power. It is interesting to see the major improvement in the Pegasus II's cruise speed due to the variation of the empty weight while it only slightly affects the Cirrus SR22's.

Similarly, maximum lift coefficient also has no effect in the maximum rate of climb as shown in Figure 4.106. The rate of climb tends to be more sensitive to the variation of the other parameters in the Pegasus II than in the Cirrus SR22. The two critical parameters are empty weight and engine power.

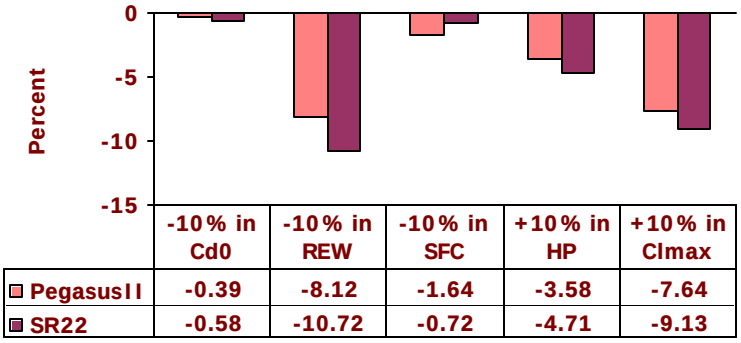

	-10% in Cd0	-10% in REW	-10% in SFC	+10% in HP	+10% in Clmax
PegasusII	-0.39	-8.12	-1.64	-3.58	-7.64
SR22	-0.58	-10.72	-0.72	-4.71	-9.13

Figure 4.103 Takeoff distance sensitivity

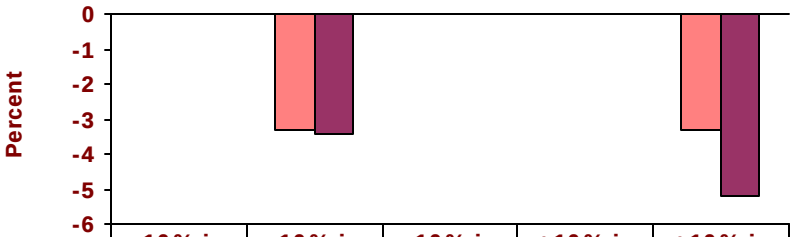

	-10% in Cd0	-10% in REW	-10% in SFC	+10% in HP	+10% in Clmax
PegasusII	0.00	-3.33	0.00	0.00	-3.33
SR22	0.00	-3.45	0.00	0.00	-5.17

Figure 4.104 Stall speed sensitivity

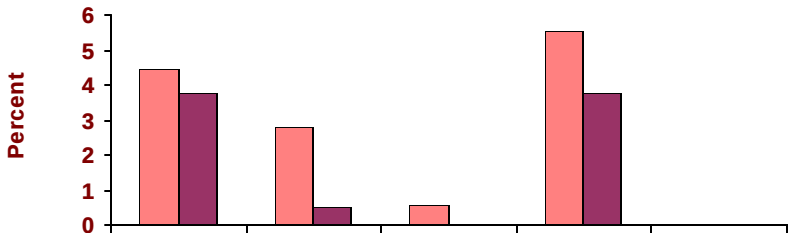

	-10% in Cd0	-10% in REW	-10% in SFC	+10% in HP	+10% in Clmax
Pegasus II	4.44	2.78	0.56	5.56	0.00
SR22	3.78	0.54	0.00	3.78	0.00

Figure 4.105 Cruise speed sensitivity

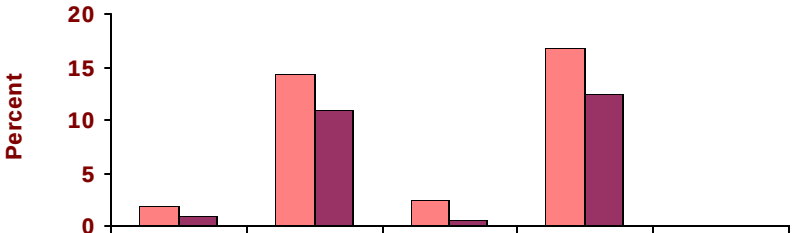

	-10% in Cd0	-10% in REW	-10% in SFC	+10% in HP	+10% in Clmax
Pegasus II	1.91	14.42	2.44	16.77	0.00
SR22	0.95	10.89	0.65	12.44	0.00

Figure 4.106 Maximum rate of climb sensitivity

The differences in sensitivities between the Pegasus II and the Cirrus SR22 are primarily caused by the smaller wing span of the former vehicle. The unique wing concept of the Pegasus II enhanced its supposedly critical performance due to the dimension restriction by reducing its empty weight and improving its lift coefficient. It enables the Pegasus II to competitively operate with respectable general aviation aircraft like the Cessna 182 or the Cirrus SR22. A lift augmentation from the inboard-winglet concept clearly has an effect on the takeoff performance almost as great as the empty weight has. While the effect of the additional thrust due to the winglets is not very noticeable since the overall empty weight dominates most of the sensitivity analysis, the results show that the winglets' thrust is more valuable in the takeoff condition than in cruise.

Chapter 5

Conclusions and Recommendations

5.1 Conclusions

An investigation of the inboard-winglet concept on a roadable aircraft is primarily concentrated on the study of flow characteristics around the concept model and analytical application of that knowledge in a design approach of an actual aircraft. The flow characteristics were studied in the wind tunnel by measuring the pressure coefficients over the wing and the winglet surface. The change in aerodynamic characteristics observed in the experiment was modeled to find their relevant design parameters, and were used in the performance estimation of the Pegasus II.

Without the added flow from the propeller, the inboard winglets act like typical wingtip winglets causing an induced flow over the wing for both inboard and outboard sections by their circulations. The induced flow is stronger in the outboard side because it is connected to the winglet suction side. The main wing lift distribution also produces sidewash that alters the winglet effective angle of attack. The outboard sections near the winglets were very sensitive to laminar separation, which consistently appears in the test at low Reynolds number.

Spanwise pressure distributions and winglet pressure distribution indicate that, unlike a conventional wing-propeller arrangement, a presence of the propeller only induced the flow inside the rectangular channel of the wing and the winglets. It improves the lift characteristics of the wing depending on a freestream velocity and thrust setting. A difference in pressure distribution due to the propeller barely varied with a change in an angle of attack Thus, only a thrust coefficient influences a change in wing lift coefficient. The wing likely has a separation first at the outboard location near the winglets because of the winglet circulation while the inboard section separation is delayed by the propeller-

induced flow. This gives an unusual stall characteristic that the lift curve is almost flat at its peak before gradually declining.

By integrating the pressure distribution over the winglets, drag coefficients indicate that a deflection of the winglets produce a thrust component depending on the lift distribution and power setting. For the negative lift configuration, the winglets tend to create additional profile drag instead of thrust. The optimal deflection must design by considering both factors. In an integration of the wing section pressure distribution, it shows that a propeller-induced lift coefficient inside the channel is slightly higher than a 2D lift coefficient. Thus it is possible to assume it equal to the 2D data in the Pegasus II performance estimation.

The calculation for the maximum thrust produced by the winglets in the Pegasus II shows that the additional thrust would increase the wing lift to drag ratio by 5.2% giving an effective aspect ratio to be 1.052 of the geometric aspect ratio.

With the estimated wing lift coefficient and thrust, the performance of the Pegasus II proves to be competitively acceptable, even with its restricted wing area, since the new wing concept considerably reduces the vehicle empty weight and enhances the lift coefficient. The additional thrust from the inboard-winglets hardly is a major influence on the performance since it improves the effective aspect ratio is less than typical winglets.

Without a doubt, the inboard-winglet concept provides another possible option for lift augmentation with no complicated structures or moving parts. The unique integration of the concept to a general aircraft design, such as its merging into vertical stabilizers in the Pegasus II, can offer its advantages to the design without adding more drag penalty.

5.2 Recommendations for Future Work

Even though a potential of the inboard-winglet concept to enhance the lift coefficient was obviously visible in this experiment, there are other issues that should be dealt in a future study for better understanding and firmly proving a utilization of the concept in an aircraft design.

With time limitation, only one thrust setting was performed in this experiment. It was showed both experimentally and analytically that the thrust setting highly influenced the flow in the inboard-winglet wing. Thus, an effect of a thrust-setting variation on flow characteristics should be cautiously evaluated with a more accurate thrust measurement.

The experimental data, especially at the static condition, indicated unsymmetrical pressure distributions for the spanwise direction. They could be an effect of a propeller-swivel flow that alters the induced flow over the wing. Therefore, an effect of the swivel flow to the inboard-winglet wing should be investigated in order to create a more accurate analytical approximation for the additional lift.

A stall characteristic shown in the experimental data is a concern for an application of the inboard-winglet wing in an actual aircraft. A detailed study to determine an explanation for its relation to a winglet deflection or a swivel flow is necessary.

Also, given from this research that the additional thrust due to winglets varied with strong vortices on the wing which means a wing high-induced drag for the winglets to generate high thrust. An analysis for an optimized design point will help confirm advantages and disadvantages of the concept.

References

Abbot and Von Doenhoff, *Theory of Wing Sections*, 1959

Anderson, J. D., JR., *Introduction to Flight*, International 3rd edition, McGraw-Hill Book Company, Singapore, 1989

Blackwell, J. A., Jr., *Numerical Method to Calculate the Induced Drag or Optimum Loading for Arbitrary Non-Planar Aircraft*, NASA SP — 405, 1976

Blick, E. F., *A Special Report on an Aerodynamic Evaluation of the Channel Wing Concept*, Defense Advanced Research Programs Agency, Washington, D.C., May 1988

Czajkowski, M., Clausen, G., and Sarh, B., *Telescopic Wing of an Advanced Flying Automobile*, AIAA (#975602), 1997

Devenport, W. J., *Uncertainty (or, How to Estimate Experimental Error)*, AOE 3054-class 6 handout, Aerospace and Ocean Engineering Department, Virginia Tech, 2002

Devenport, W. J. and Vadapalli, B., *Panel Method Applet: Instructions*, http://www.engapplets.vt.edu/, Virginia Tech, 1998

Durongphant, N. and Withayawinit, A., *Investigation of Channel Wing Variations*, Aerospace Engineering Senior Project Report, Aerospace Engineering Department, Kasetsart University, February 2001

Freiherr, G., *What Has Four Wheels and Flies? The Dream of a Roadable Airplane Continues*, http://www.airspacemag.com/ASM/Mag/Index/1996/DJ/ccsf.html, Air & Space /Smithsonian, December 1995/January 1996

Gassler, R, et.al., *Pegasus, A report to the AGATE NASA/FAA General Aviation Design Competition*, Virginia Tech Aerospace & Ocean Engineering Department, May 2000

Grissom, D. and Henry, L., *Investigation of Channel Wing Variations*, Undergraduate Research Summer-Fall 2000, Aerospace and Ocean Engineering Department, Virginia Tech, 2000

Gunther, C. L., *Comparison of Channel Wing Theoretical and Experimental Performance*, 1999 in Honors Degree Requirement Undergraduate Research Thesis, Virginia Tech, May 1998

Jacobs, E. N., Ward, K. E., and Pinkerton, R., *The Characteristics of 78 Related Airfoil Section from Tests in the Variable-Density Wind tunnel*, Report No. 460, National Advisory Committee for Aeronautics, 1933

LeCompte, T., *Highway in the Sky: The Age of a Flying Car in Every Garage Maybe Dawning*, http://www.hartfordadvocate.com/articles/skycar.html, New Mass. Media Inc., 1999

Marchman, J. F., III, Intaratep, N., Skelton, C. E., and Mason, W. H., *An Investigation of CTOL Dual-Mode PAVE Concepts*, NASA grant NAG-1-01100, January 2002

McGhee, R. J., Beasley, W. D., and Somers, D. M., *Low-Speed Aerodynamic Characteristics of A 13-Percent-Thick Airfoil Section Designed for General Aviation Applications, NASA TM X-72697*, Langley Research Center, Hampton, VA, May, 1977

McGhee, R. J. and Beasley, W. D., *Low-Speed Aerodynamic Characteristics of a 17-Percent-Thick Medium Speed Airfoil Designed for General Aviation Applications*, NASA-TP-1786, 1980

Mish, P. F., *Mean Loading and Turbulence Scale Effects on the Surface Pressure Fluctuations Occurring on a NACA 0015 Airfoil Immersed in Grid Generated Turbulence*, Master thesis, Virginia Tech, May 2001

Nicolai, L. M., *Fundamentals of Aircraft Design*, Domicone Printing Services, Fairborn, Ohio, 1975

Pasamanick, J., *Langley Full-Scale-Tunnel Tests of the Custer Channel Wing Airplane*, NACA RM L53A09, 1953

Rae, W. H., and Pope, A., *Low-Speed Wind Tunnel Testing*, second edition, John Wiley & Sons, Canada, 1984

Raymer, D. P., *Aircraft Design: A Conceptual Approach*, American Institute of Aeronautics and Astronautics, Inc., Washington, D.C., 1989

Roskam, J., *Airplane Design Part 1: Preliminary Sizing of Airplanes*, DARcorporation, Lawrence, Kansas, 1997

Roskam, J., Lan, Chuan-Tau E., *Airplane Aerodynamics and Performance*, DARcorporation, Lawrence, Kansas, 1997

Scott, J, http://www.aerospaceweb.org, 2002

Stiles, P., *Roadable Aircraft: From Wheels to Wings,* Custom Creativity, Inc., Melbourne, FL, August 1994

Young, D. W., *Test of 1/3-Scale Powered Model of Custer Channel Shaped Wing*, Army Air Forces Technical Report No. 5142, 1944

Young, D. W., *Test of Two Custer Channel Wings Having a Diameter of 37.2 Inches and Lengths of 43 and 17.5 Inches*, Army Air Forces Technical Report No. 5568, 1947

http://www.aoe.vt.edu/aoe/physical/tunnel_descrip.htm

http://www.dual-use.com

http://www.labicheaerospace.com

http://www.maam.org/ccw5.html

Appendix A

3D Lift Coefficient Approximation of the Pegasus II

To acquire a better solution for a wing design in the Pegasus II, a new method of stowing outboard wing components inside an inboard wing was applied instead of a telescoping wing concept. Since a 17-percent thick of GA (W)-1 barely provide sufficient space for a wing with a thick airfoil, an outboard wing airfoil was replace by a 13-percent thick airfoil section, GA (W)-2, similarly having a high maximum lift coefficient. According to a combination of 2 different airfoil sections, the maximum lift coefficient of the Pegasus II was varied from the original model. There are 2 assumptions for this calculation:

1. The lift distribution of the inboard section was considered to resemble that of a 2D airfoil due to the effect of vertical stabilizers at the tip of the section.
2. The lift distributions of the outboard wings were calculated by merging the 2 outboard section sides of wing and considering them to act as one continuous wing.

For the outboard sections, their 3D characteristics were evaluated by an approach from Nicolai (Nicolai, 1975) starting from examining 2-D maximum lift coefficients of GA(W)-2. They were varied with Reynolds Numbers for different flight conditions as shown in Table A.1.

Table A.1 2-D maximum lift coefficients of the GA(W)-2 (McGhee, et.al., 1977)

Flight condition	Max 2-D lift coefficient
Cruise	2.08
Takeoff and landing	1.97
Stall speed	1.84

3-D maximum lift coefficients were estimated from:

$$C_{L\max} = \left(\frac{C_{L\max}}{C_{l\max}} \right) C_{l\max} \tag{A.1}$$

where $\left(\frac{C_{L\max}}{C_{l\max}} \right)$ was given in Figure A.1, which was 0.9 for 0 swept angle, Λ_{LE} .

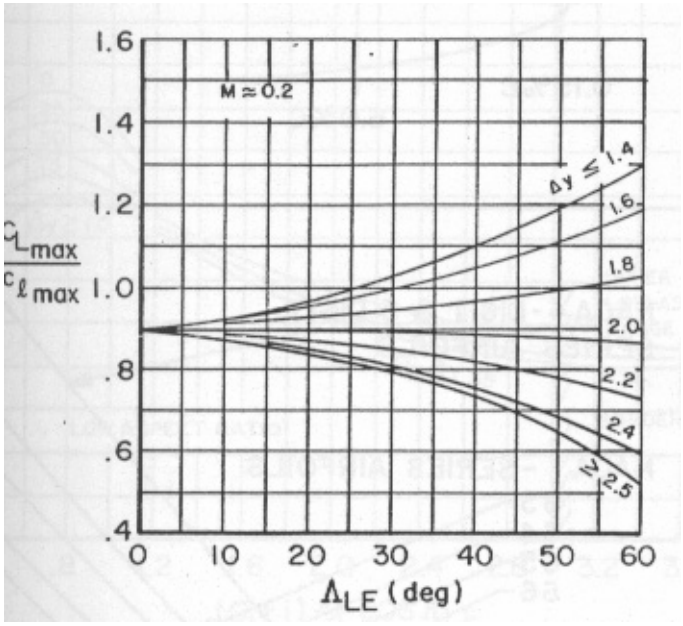

Figure A.1 Variation of $\left(\frac{C_{L\max}}{C_{l\max}} \right)$ with Λ_{LE} (Nicolai, 1975)

As a result, an estimation of 3-D maximum lift coefficients was found in Table A.2.

Table A.2 3-D maximum lift coefficients of GA(W)-2 for different flight conditions

Flight condition	Max 3-D lift coefficient
Cruise	1.872
Takeoff and landing	1.773
Stall speed	1.656

A construction of 3D lift curve was achieved by applying this equation the wing design of the outboard section to find a lift curve slope.

$$\frac{dC_L}{d\alpha} = \frac{2\pi\ AR_e}{2 + \left[4 + \frac{AR^2\beta^2}{\eta^2}\left(1 + \frac{\tan^2\Lambda_t}{\beta^2}\right)\right]^{0.5}} \frac{S_{\exp}}{S} F \qquad \text{(A.2)}$$

In this case, an effective aspect ratio was assumed to be that of a straight outboard wing with 17-feet span and 5.2-feet chord since some of a lift distribution from the inboard section should affect the total lift curve slope of the outboard section. Hence, AR_e equaled 3.269. With 3.7 ft of a fuselage width, F was calculated to be 1.5865 and $S_{\exp}$ was 69.16 ft^2. The 3-D lift curve slope of GA (W)-2 section was approximated to be 0.0764 per degree.

The following equation was applied to obtain a 3D stall angle of attack of the outboard section:

$$\alpha_{stall} = \frac{C_{L\max}}{C_{L_\alpha}} + \alpha_{0L} + \Delta\alpha_{C_{L\max}} \qquad \text{(A.3)}$$

A relationship of $\Delta\alpha_{C_{L\max}}$, taper ratio and Δy is shown in Figure A.2

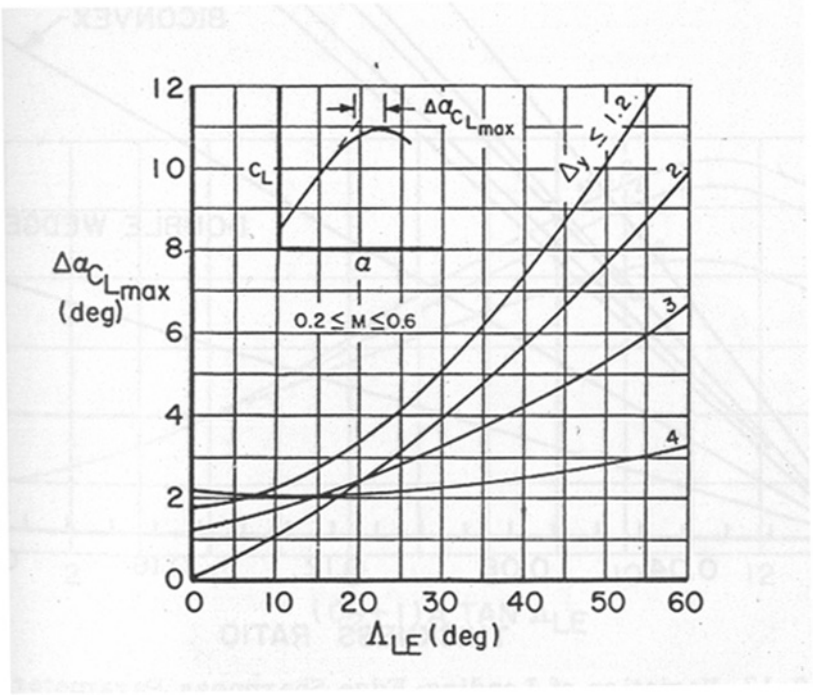

Figure A.2 Variation of $\Delta\alpha_{C_{L\max}}$ with Λ_{LE} (Nicolai, 1975)

Moreover, an application of high-lift devices was evaluated. The Pegasus II employed flaperons of a plain flap type to enhance its wing lift characteristic during takeoff and landing. A flap chord ratio ($\frac{c_f}{c}$) is 0.2 and a flap span ratio ($\frac{S_{wf}}{S_w}$) is 0.65.

A change in zero-lift angle of attack (α_{0L}) was found by:

$$\Delta\alpha_{0L} = -\frac{dC_l}{d\delta_f}\frac{1}{C_{l_\alpha}}\delta_f K' \tag{A.4}$$

Figure A.3 indicates a variation of K', which is 1, 0.87, 0.6 for a 10, 20, and 40-degree flap deflection respectively. Also, Figure A.4 shows that $\frac{dC_l}{d\delta_f}$ approximately is 3.65 for the flap chord ratio of 0.2.

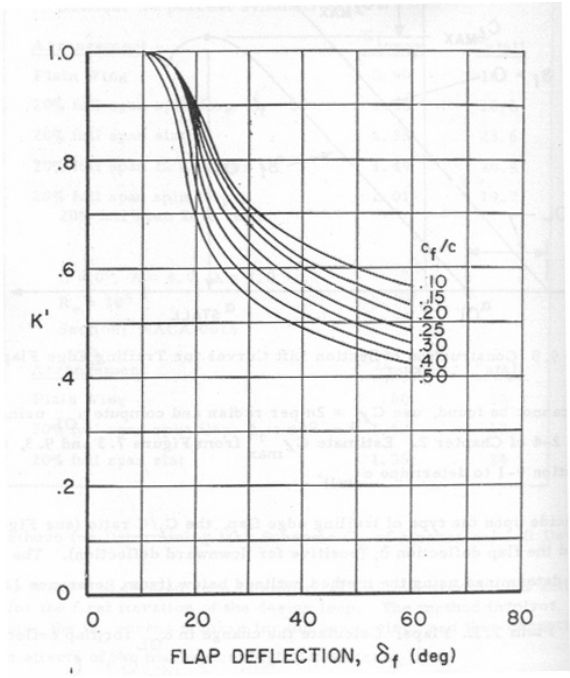

Figure A.3 Non-linear correction for plain trailing edge flaps (Nicolai, 1975)

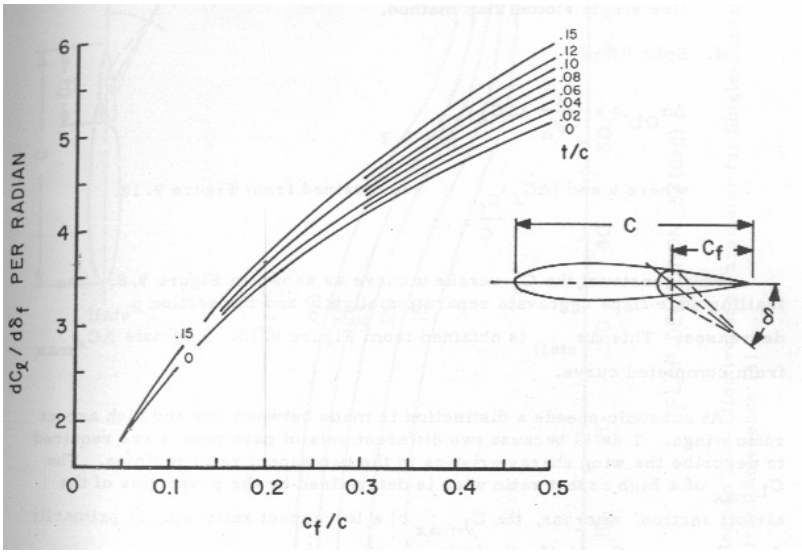

Figure A.4 Variation of $\frac{dC_l}{d\delta_f}$ with a flap chord ratio (Nicolai, 1975)

A variation of a 2D stall angle of attack with a δ_f flap deflection was obtained from Figure A.5 for a desired flap chord ratio. Afterward, A 2D lift curve with flap deflection was constructed following Figure A.6 based on a lift curve from experimental data of GA (W)-2 airfoil (McGhee, et.al., 1977).

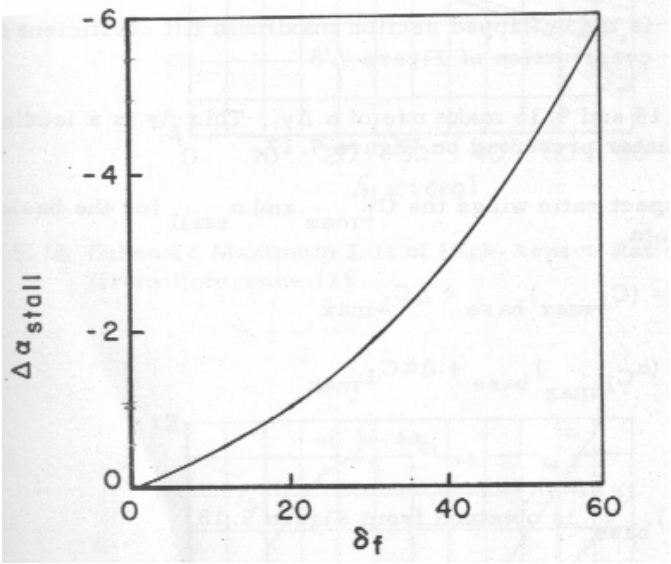

Figure A.5 Decrease in Stall Angle with Flap Deflection (Nicolai, 1975)

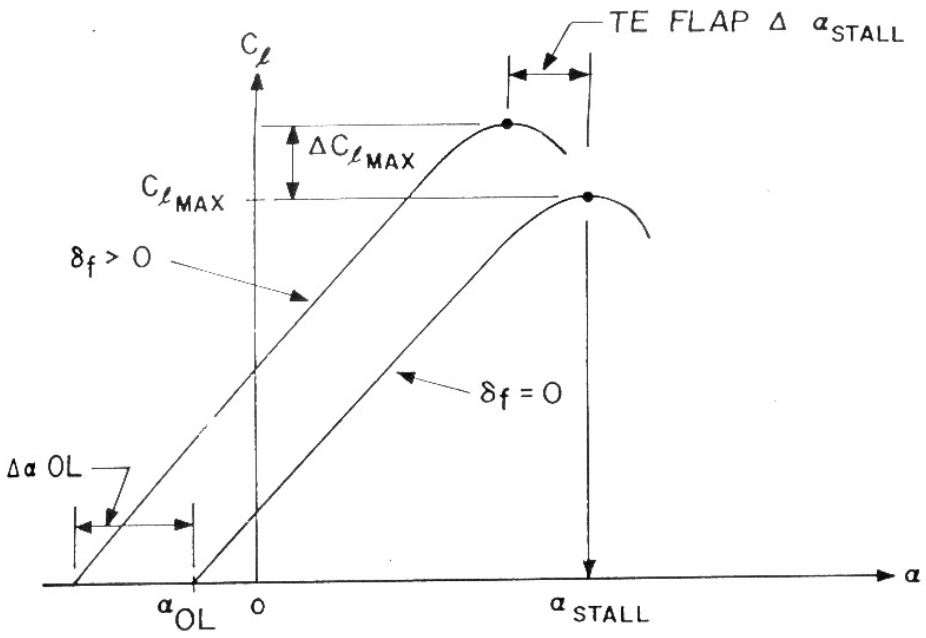

Figure A.6 Construction of a section lift curves for trailing edge flaps (Nicolai, 1975)

The previous calculations of $C_{L\max}$, $\frac{dC_L}{d\alpha}$ and α_{stall} provided a 3D lift curve of the outboard section without flap deflection. An effect of plain flap deflection on the 3D lift curve is a change in a zero-lift angle of attack, which equaled to a change in that of the 2D lift curve. However, there was an increase in $C_{L\max}$.

$$\Delta C_{L_{\max}} = \Delta C_{l\max} \frac{S_{Wf}}{S_w} K_\Lambda \qquad \text{(A.5)}$$

For non-taper wing, K_Λ equals 0.92

This calculation was used in the construction of 3D lift curve with flap deflection, having the same lift curve slope as the one without the application of flaps. It is shown in Figure A.7 for a plot of GA (W)-2 lift curves

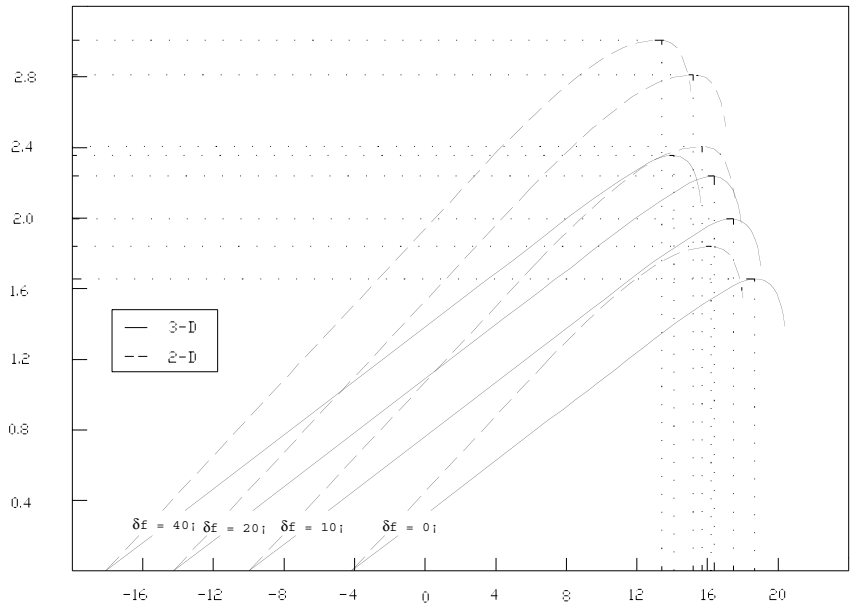

Figure A.7 Plot of lift curves for the GA (W)-2 as 2D and 3D

The $C_{L\max}$ and α_{stall} for flap deflections of 10 — 40 degrees are shown in Table A.3

Table A.3 3D maximum lift coefficients of the GA(W)-2 for different flight conditions

Flap deflection	$C_{L\max}$	α_{stall}
10	1.9952	17.48
20	2.2378	16.37
40	2.3563	14.09

Both set of results would be applied to find total wing lift coefficients of the Pegasus II as the stall angles of attack of the outboard wing would also considered to be a stall limit of the inboard wing since they are smaller than 2D stall angle of attack of the GA(W)-1.

Appendix B

Input Data of Comparator Aircraft

Comparator models	Cessna 182	Cirrus SR22	LaBiche FSC-1	Pegasus II
Range (nm)	400	400	400	400
Loiter (mins)	45	45	45	45
Cruise altitude (ft)	10000	8000	10000	8000
Wing span (ft)	36	38.5	32.13	17
Wing area (ft^2)	174	144.9	130.34	111.5
Effective aspect ratio	7.45	10.23	7.92	2.02
Engine/HP	253	310	445	359.232
Propeller efficiency	0.80	0.80	0.74	0.88
SFC (lb/hp-hour)	0.4500	0.4500	0.2970	0.5032
Cd0 cruise	0.02500	0.01811	0.01000	0.02410
Cd0 takeoff	0.07100	0.05000	0.06000	0.07176
Cd0 landing	0.08200	0.06000	0.07000	0.08297
Clmax cruise	1.80470	1.41450	1.40000	1.85024
Clmax takeoff	1.90000	1.60000	1.80000	1.98283
Clmax landing	2.19180	1.99000	2.10000	1.99540
Cl setting angle	0.29946	0.27213	0.25000	0.42275
Oswald efficiency factor	0.83	0.75	0.81	0.98
Require empty weight (lbs)	1897	2250	2455	1594
Payload (lbs)	800	800	800	800

Appendix C

Performance Estimation Codes

Performance estimation of comparator aircraft was calculated in MATLAB release 12. The following codes were developed using the approach in Chapter 3.

1. Input Data Collecting

```
% Input data and calculated configuration
% Written by: Nanyaporn Intaratep
% Last update: 09-19-01

% INPUT

clear
clc
name = input('Enter airplane''s character: ','s');  %for these conditions
matname = input('Enter an input file name: ', 's'); %mat-file name
cruise = input('Enter cruise range(nm): ');        %nm
cruise = cruise*1.15;                              %miles
loiter = input('Enter loitering time(mins): ');    %mins
loiter = loiter/60;                                %hours
cruisealt = input('Enter cruise altitude(ft): ');  %feet
[Talt, Palt, rhoalt, Aalt, MUalt, TSalt, RRalt, PPalt, RMalt, QMalt,
getanswer]=stdprop(cruisealt,1);
if getanswer == 0
   disp(sprintf('Error calculating matched air density, data out of table'))
   break
end
```

```
toalt = 0;          % take-off altitude            feet
rhoSL = .002377;    %air density at sea level       slug/ft^3
b = input('Enter wing span(ft): ');                 %feet
S = input('Enter wing area(ft^2): ');               %feet^2
hp = input('Enter engine hp: ');                    %horsepower
etap = input('Enter propeller efficiency: ');       %propeller near engine
% T0 = input('Enter static thrust: ');              %calculate in note
cp = input('Enter specific fuel consumption: ');    %lb/hp-hour
Cd0 = input('Enter Cd0 for cruise: ');              %at cruise
Cd0TO = input('Enter Cd0 for takeoff: ');
Cd0land = input('Enter Cd0 for landing: ');
Clcruise = input('Enter Clmax for cruise speed: '); %flap up
ClmaxTO = input('Enter Clmax for takeoff: ');       %takeoff configuration
Clmaxland = input('Enter Clmax for landing: ');     %landing configuration
Clgr = input('Enter Cl at setting angle: ');
e = input('Enter Oswald efficiency factor: ');      %e=1.78(1-0.045AR^0.68)-0.64
add = input('Additional factor for effective aspect ratio: ');
rew = input('Enter requirement empty weight(lbs): ');     %lbs
Wpay = input('Enter payload(lbs): ');               %payload (lbs)

% Calculated configuration

AR = b^2/S*add;             %efficiency aspect ratio, winglet factor of 5.5%
K = 1/(pi*AR*e);            %induced drag factor
LDmax = 1/(2*sqrt(Cd0*K));
sigmaSL = rhoSL/rhoSL;      %density ratio @ sea level
sigmaalt = rhoalt/rhoSL;    %density ratio @ altitude

save(matname);
```

2. Main Code

```
% Main program

% Written by: Nanyaporn Intaratep
% Last update: 8-28-01

% Procedure

% 1. Run 'data file' or datainput.m to enter required data
%    or
%    Run datainput.m to enter inputs and save as mat-file (variable file)

clear
clc
matname = input('Enter an input file name: ','s');
load(matname)          % call back data inputs

% Save to file

writetofile = 0;

if input('\nWould you like to creat output file?(y,n)\n?','s')=='y'
   filename=input('Enter a file name: ','s');
   wholename=strcat(filename,'.dat');
        fid=fopen(wholename,'w');
   writetofile = 1;
end

% Show data input
```

```
clc
disp('AIRCRAFT SIZING FOR SINGLE ENGINE PROPELLER DRIVEN AIRPLANE');
disp(sprintf('\n'));
disp(sprintf('DEFINED INPUT FOR: %s',name));
disp(sprintf('\n'));
disp(sprintf('Mission specification:'));
disp(sprintf('Cruise range for %5.0f nm plus 45 mins loiter\n', cruise/1.15));
disp(sprintf('Weight data:'));
disp(sprintf('Required empty weight          %-10.0f lbs', rew));
disp(sprintf('Payload                        %-10.0f lbs', Wpay));
disp(sprintf('Plus, %1.0f %% reserve and %1.0f %% trapped fuel \n', 5, 1));
disp(sprintf('Fuel fraction assumption:'));
disp(sprintf('Start and warmup %4.3f, taxi %4.3f, takeoff %4.3f',.995,.997,.998));
disp(sprintf('Decent %4.3f, landing taxi and shutdown %4.3f \n',.933,.993));
disp(sprintf('Aerodynamic data:'));
disp(sprintf('Efficiency aspect ratio        %-10.2f', AR));
disp(sprintf('Oswald efficiency factor       %-10.2f', e));
disp(sprintf('Cd0 @ cruise                   %-10.4f', Cd0));
disp(sprintf('Cd0 @ takeoff                  %-10.4f', Cd0TO));
disp(sprintf('Cd0 @ landing                  %-10.4f', Cd0land));
disp(sprintf('Clmax @ cruise                 %-10.4f', Clcruise));
disp(sprintf('Clmax @ takeoff                %-10.4f',ClmaxTO));
disp(sprintf('Clmax @ landing                %-10.4f', Clmaxland));
disp(sprintf('Cl @ setting angle             %-10.4f \n', Clgr));
disp(sprintf('Engine data:'));
disp(sprintf('Engine horsepower              %-10.0f', hp));
disp(sprintf('Propeller efficiency           %-10.2f', etap));
% disp(sprintf('Static thrust                %-10.0f', T0));
disp(sprintf('Specific fuel consumption      %-10.2f', cp));
disp(sprintf('\n'));
disp(sprintf('Waiting for the results...'));
```

```
disp(sprintf('\n'));

if writetofile

   fprintf(fid,'AIRCRAFT SIZING FOR SINGLE ENGINE PROPELLER DRIVEN AIRPLANE\n');
   fprintf(fid,'\n');
   fprintf(fid,'DEFINED INPUT FOR: %s\n',name);
   fprintf(fid,'\n');
   fprintf(fid,'Mission specification: \n');
   fprintf(fid,'Cruise range for %5.0f nm plus 45 mins loiter\n', cruise/1.15);
   fprintf(fid,'\n');
   fprintf(fid,'Weight data: \n');
   fprintf(fid,'Required empty weight          %-10.0f lbs\n', rew);
   fprintf(fid,'Payload                        %-10.0f lbs\n', Wpay);
   fprintf(fid,'Plus, %1.0f %% reserve and %1.0f %% trapped fuel \n', 5, 1);
   fprintf(fid,'\n');
   fprintf(fid,'Fuel fraction assumption: \n');
   fprintf(fid,'Start and warmup %4.3f, taxi %4.3f, takeoff %4.3f \n',.995,.997,.998);
   fprintf(fid,'Decent %4.3f, landing taxi and shutdown %4.3f \n',.933,.993);
   fprintf(fid,'\n');
   fprintf(fid,'Aerodynamic data: \n');
   fprintf(fid,'Efficiency aspect ratio        %-10.2f \n', AR);
   fprintf(fid,'Oswald efficiency factor       %-10.2f \n', e);
   fprintf(fid,'Cd0 @ cruise                   %-10.4f \n', Cd0);
   fprintf(fid,'Cd0 @ takeoff                  %-10.4f \n', Cd0TO);
   fprintf(fid,'Cd0 @ landing                  %-10.4f \n', Cd0land);
   fprintf(fid,'Clmax @ cruise                 %-10.4f \n', Clcruise);
   fprintf(fid,'Clmax @ takeoff                %-10.4f \n',ClmaxTO);
   fprintf(fid,'Clmax @ landing                %-10.4f \n', Clmaxland);
   fprintf(fid,'Cl @ setting angle             %-10.4f \n',Clgr);
```

```
    fprintf(fid,'\n');
    fprintf(fid,'Engine data: \n');
    fprintf(fid,'Engine horsepower                %-10.0f \n', hp);
    fprintf(fid,'Propeller efficiency             %-10.2f \n', etap);
    % fprintf(fid,'Static Thrust                  %-10.0f \n', T0);
    fprintf(fid,'Specific fuel consumption        %-10.2f \n', cp);
    fprintf(fid,'\n');

end


% 2. Run TOWeight.m to estimate take-off weight

TOWeight;


% 3. Run function todist.m to estimate take-off distance

%[Sg, Sto, TOP] = todist(WoS, WoP, sigmaSL, Clflap60);
[Sg, Sto] = takeoff(ClmaxTO,Clgr,TOGW,rhoSL,S,AR,K,Cd0TO,hp,etap);


% 4. Run function ldist.m to estimate landing distance

%[Sl,Slg] = ldist(Vstallwf*.869);
[Sl,Slg]=landing(TOGW,S,Clmaxland,Clgr,Cd0land,rhoSL,K);


% 5. Run function ceiling.m to estimate absolute and service ceiling
%    (under varifying)
```

```
[rhoabs, absceil] = ceiling(0, etap, WoS, WoP, Clmp, Cdmp);
[rhoser, serceil] = ceiling(100, etap, WoS, WoP, Clmp, Cdmp);


% 6. Run function Vel.m to estimate stall speed w/ and w/o flaps

[Vstallflapdown] = Vel(TOGW, rhoSL, S, Clmaxland);
[Vstallflapup] = Vel(TOGW, rhoalt, S, Clcruise);


% 7. Run function maxcruise.m to estimate maximum cruise speed at 80* power

[Vcmax] = maxcruise(hp,etap,rhoalt,S,Cd0,TOGW,K);


% 8. Display results

disp('============================================================')
disp(sprintf('\n'));
disp(sprintf('FINAL PERFORMANCE RESULTS FOR: %s',name));
disp(sprintf('\n'));
disp(sprintf('Take Off Gross Weight              %-10.0f lbs', TOGW));
disp(sprintf('Empty Weight                       %-10.0f lbs', rew));
disp(sprintf('Fuel Weight                        %-10.0f lbs',Wf));
disp(sprintf('                                   %-10.0f gals', gallon));
disp(sprintf('Wing loading                       %-10.1f lb/ft2', WoS));
disp(sprintf('Power loading                      %-10.1f lb/hp',WoP));
disp(sprintf('Range                              %-10.0f nm', cruise/1.15));
disp(sprintf('Take-off groundrun                 %-10.0f ft', Sg));
disp(sprintf('Take-off and 50 ft clear distance  %-10.0f ft', Sto));
disp(sprintf('Landing groundrun                  %-10.0f ft', Slg));
```

```
disp(sprintf('Landing and 50 ft clear distance      %-10.0f ft',Sl));
if ischar(serceil)==0
disp(sprintf('Service ceiling                    %-10.0f ft',serceil));
else
   disp('Error: service ceiling is out of table ');
end
if ischar(absceil)==0
disp(sprintf('Absolute ceiling                   %-10.0f ft',absceil));
else
   disp('Error: absolute ceiling is out of table ');
end
disp(sprintf('Maximum cruise speed at 0.8 power     %-10.0f kts', Vcmax*0.869));
disp(sprintf('Stall speed w/flap at sea level       %-10.0f kts', Vstallflapdown*.869));
disp(sprintf('Stall speed clean at cruise altitude  %-10.0f kts', Vstallflapup*.869));
disp(sprintf('Maximum rate of climb                 %-10.0f fpm\n', RoCSL));
save(filename);


if writetofile

disp(sprintf('Created output file %s \n', wholename));


fprintf(fid,'============================================================\n'
);
   fprintf(fid,'\n');
   fprintf(fid,'FINAL PERFORMANCE RESULTS FOR: %s\n',name);
   fprintf(fid,'\n');
   fprintf(fid,'Take Off Gross Weight               %-10.0f lbs\n', TOGW);
   fprintf(fid,'Empty Weight                        %-10.0f lbs\n', rew);
   fprintf(fid,'Fuel Weight                         %-10.0f lbs\n',Wf);
```

```
   fprintf(fid,'                          %-10.0f gals\n', gallon);
   fprintf(fid,'Wing loading                  %-10.1f lb/ft2\n', WoS);
   fprintf(fid,'Power loading                 %-10.1f lb/hp\n',WoP);
   fprintf(fid,'Range                        %-10.0f nm\n', cruise/1.15);
   fprintf(fid,'Take-off groundrun            %-10.0f ft\n', Sg);
   fprintf(fid,'Take-off and 50 ft clear distance   %-10.0f ft\n', Sto);
   fprintf(fid,'Landing groundrun             %-10.0f ft\n',Slg);
   fprintf(fid,'Landing and 50 ft clear distance    %-10.0f ft\n',Sl);
   if ischar(serceil)==0
   fprintf(fid,'Service ceiling               %-10.0f ft\n',serceil);
   else
      fprintf(fid,'Error: service ceiling is out of table \n');
   end
   if ischar(absceil)==0
   fprintf(fid,'Absolute ceiling              %-10.0f ft\n', absceil);
   else
      fprintf(fid,'Error: absolute ceiling is out of table \n');
   end
   fprintf(fid,'Maximum cruise speed at 0.8 power   %-10.0fkts\n', Vcmax*0.869);
   fprintf(fid,'Stall speed w/flap at sea level     %-10.0fkts\n', Vstallflapdown*.869);
   fprintf(fid,'Stall speed clean at cruise altitude  %-10.0f kts\n', Vstallflapup*.869);
   fprintf(fid,'Maximum rate of climb          %-10.0f fpm\n',RoCSL);
   fclose(fid);

end
```

3. Takeoff Gross Weight Calculation

```
% Program TOWeight.m

% Written by: BER SIDELL and NANYAPORN INTARATEP
% Last updated: 9-28-01

% Description:
% This program uses to define take-off gross weight for single engine airplane
% by applying fuel fraction method.
% The mission is to takeoff and climb to cruise altitude, cruise to destination
% and loiter 45min before descend and land.
% The fuel fraction is divided into 8 stages,
% 1. Engine start and warmup
% 2. Taxi
% 3. Takeoff
% 4. Climb and accelerate to cruise altitude
% 5. Cruise
% 6. Loiter
% 7. Decent
% 8. Landing, taxi and shutdown

% References:
% Jan Roskam, AIRPLANE DESIGN, PART 1: PRELIMINARY SIZING OF
AIRPLANES, 1997
% Chapter 2, section 2.1 and 2.4

%INPUT

   %cruise          Distance required by mission
   %loiter          loiter time required by mission
   %cruisealt       altitude for cruise
   %toalt           altitude at takeoff
   %b               wing span
   %S               wing area
   %hp              maximum engine horse power
   %Cd0             zero lift drag coefficient
   %Clmaxland       lift coefficient w/flap
   %e               Oswald efficiency factor
   %etap            Propeller efficiency
   %cp              specific fuel consumption
   %rhoalt          air density at altitude (slugs/ft^3)
   %rhoSL           air density at sea level (slugs/ft^3)
   %rew             required empty weight
   %Wpay            payload
```

```
   %LDmax          L/D max
   %AR             Aircraft aspect ratio
   %K              induced drag
   %sigmaSL        air density ratio at sea level, slug/ft^3
   %sigmaalt       air density ration at altitude, slug/ft^3


% OUTPUT

   %Wf             Fuel weight for aircraft during the mission
   %TOGW           Max TOGW, lbs
   %WoP            Power loading, lbs/horsepower
   %WoS            Wing loading, lbs/wing area (ft^2)
   %Vstallwf       stall speed for 60 degree flap down (takeoff, landing
   %                position), mph

% Using input data from input file

% Set fuel weight (Wf) as a symbolic

syms Wf


% Take-off gross weight equals summation of require empty weight, payload and
% Fuel weight.

TOGW = rew+Wpay+Wf;


% Calculate stall speed at takeoff w/flap 60 degree
% Use function Vel.m

[Vstallwf] = Vel(TOGW,rhoSL,S,Clmaxland);   %mph


% Calculate power and wing loading

WoP = TOGW/hp;
WoS = TOGW/S;


% Weight fractions are given as Wfinal/Winitial (Wfi)
% for each stage of the mission

% Wfi1 thru Wfi3 are taken from Table 2.1 in Roskam, single engine
```

```
Wfi1 = 0.995;                % Engine start, warmup
Wfi2 = 0.997;                % Taxi
Wfi3 = 0.998;                % Take off


% Wfi4 estimation: climb and accelerate
% Calculate by approximating climb time at maximum rate of climb to use in
% endurance equation.
% The engine is operated at the maximum constant power rating

% Use function minpwr.m to obtain minimum power require conditions

[Clmp, Cdmp, LDmp, Vmp] = minpwr(Cd0,TOGW,rhoalt,S,K);

% At minimum power require condition, use function RClimb.m to obtain maximum
% rate of climb, climb time and climb velocity.

[RoCSL,RCPSL] = RClimb(etap,WoP,WoS,Clmp,Cdmp,sigmaSL);
% RoCSL is maximum rate of climb at sea level, fpm
climbtime = (cruisealt-toalt)/RoCSL/60;
% climbtime is climb time, hrs
Vcl = 1.2*Vstallwf;
% Vcl is climb speed which is usually defined at 1.2 of stall speed, mph

% Use function fuelforendur.m to calculate fuel fraction

Wif4 = fuelforendur(climbtime, etap, cp, LDmp, Vcl);    %Wif=Wintial/Wfinal
Wfi4 = 1/Wif4;               % climb and acceleration


% Wfi5 estimation: cruise
% Use range equation, function fuelforrange.m

Wif5 = fuelforrange(cruise,etap,cp,LDmax);
Wfi5 = 1/Wif5;               % cruise


% Wfi6 estimation: loiter
% Use endurance equation for 45 minutes at minimum power require condition,
% function fuelforendur.m

Wif6 = fuelforendur(loiter, etap, cp, LDmp, Vmp);
Wfi6 = 1/Wif6;               % loiter


%Wfi7 and Wfi8 are taken from table 2.1 in Roskam
```

```
Wfi7 = 0.993;                % Decent
Wfi8 = 0.993;                % Landing, taxi and shutdown


%Calculate fuel weight, take-off gross weight, power loading and wing loading.

Mff = Wfi1*Wfi2*Wfi3*Wfi4*Wfi5*Wfi6*Wfi7*Wfi8;
% Mff is mission fuel fraction
Wfused = (1-Mff)*TOGW;
% Wfused is actual used fuel, lbs

% Solve for the solution of fuel weight

final = 'Wf=1.06*Wfused';
% actual used fuel plus 5% for reserve and 1% for trapped fuel, lbs
fueleqn = subs(final,{'Wfused'},Wfused);
Wf = solve(fueleqn,Wf);
Wf = numeric(Wf);
gallon = Wf/6;               % gallon of fuel
TOGW = subs(TOGW,{'Wf'},{Wf});
TOGW = numeric(TOGW);
WoP = subs(WoP,{'Wf'},{Wf});
WoP = numeric(WoP);
WoS = subs(WoS,{'Wf'},{Wf});
WoS = numeric(WoS);
Vstallwf = subs(Vstallwf,{'Wf'},{Wf});
Vstallwf = numeric(Vstallwf);
RoCSL = subs(RoCSL,{'Wf'},{Wf});
RoCSL = numeric(RoCSL);
```

4. Fuel Fraction for Required Endurance

```
% Program fuelforendur.m
% [Wif] = fuelforendur(endur, etap, cp, LD, V)

% Written by: BER SIDELL
% Last updated: 9-27-01

% Description:
% Calculate fuel fraction in the stage of loitering using endurance equation

% Reference:
% Jan Roskam, AIRPLANE DESIGN, PART 1: PRELIMINARY SIZING OF
AIRPLANES, 1997
% Chapter 2, equation 2.11

% INPUT

%   endur,      time needed to satisfy mission, hours
%   etap,       prop efficiency
%   cp,         specific fuel consumption, lb/(hp*hour)
%   LD,         lift to Drag ratio for max range
%   V,          velocity, mph

% OUTPUT

%   Wif,        fuel weight fraction Winitial/Wfinal

function [Wif] = fuelforendur(endur, etap, cp, LD, V)

Wif = exp(V*endur/357/LD*cp/etap);
```

5. Fuel Fraction for Required Range

```
% Program fuelforrange.m
% [Wif] = fuelforrange(range,etap,cp,LD)

% Written by: BER SIDELL
% Last updated: 9-28-01

% Description:
% This program is a function to define fuel fraction for required range

% References:
% Lan, Chuan-Tau Edward & Roskam, Jan, AIRPLANE AERODYNAMICS AND
PERFORMANCE
% p.455



% INPUT

%   range,      range needed to satisfy mission, miles
%   etap,       prop efficiency
%   cp,         specific fuel consumption, lb/(hp*hour)
%   LD,         lift to Drag ratio for max range

% OUTPUT

%   Wif,        fuel weight fraction Winitial/Wfinal

function [Wif] = fuelforrange(range,etap,cp,LD)

Wif = exp(range/375*cp/etap/LD);
```

6. Takeoff Distance Calculation

```
% Program takeoff.m
% [Sg, Sto] = takeoff(Clmax,Clgr,TOGW,rho,S,AR,K,Cd0TO,hp,etap)

% Written by: Nanyaporn Intaratep
% Last updated: 10-28-01

% Description:
% This program is a function to define take-off distance for ground roll
% and clear 50' obstacle. The calculation based on no ground effect
% assumption.

% References:
% Nicolai, Leland M., Fundamentals of Aircraft Design, 1975, Section 10.3

%INPUT

%   TOGW     takeoff gross weight, lbs
%   Clmax    Clmax at takeoff
%   Clgr     Cl at setting angle
%   rho      air density, slug/ft^3
%   S        wing area, ft^2
%   AR       Aspect ratio
%   K        induce drag factor
%   Cd0TO    zero-lift drag coefficient
%   hp       engine horse power
%   etap     propeller efficiency

%OUTPUT

%   Sg       Take-off ground roll distance, ft
%   Sto      Take-off & clear 50' distance, ft



function[Sg, Sto] = takeoff(Clmax,Clgr,TOGW,rho,S,AR,K,Cd0TO,hp,etap)

Clto = 0.8*Clmax;              % Vlof = 1.15Vstall
Cdgr = Cd0TO + K*Clgr^2;       % no ground effect
Vstall = (2*TOGW/rho/Clmax/S)^0.5;
Vto = 1.2*Vstall;              % takeoff speed
Vto07 = 0.7*Vto;               % 0.7 of takeoff speed
qto = rho*Vto^2/2;             % dynamic pressure for takeoff speed
```

```
qto07 = rho*Vto07^2/2;          % dynamic pressure for takeoff speed

Tto = etap*hp*550/Vto07;        % thrust at 0.7 takeoff speed
Dto = qto07*S*Cdgr;             % drag at 0.7 takeoff speed
Lto = qto07*S*Clgr;             % lift at 0.7 takeoff speed

mue = 0.025;                    % Concrere and Macadam
Sngr = 1.44*(TOGW/S)/32.17/rho/Clmax/(Tto/TOGW-Dto/TOGW-mue*(1-Lto/TOGW));
% distance when nose-wheel on the ground

Sr = Vto;                       % rotational distance, t-rotation = 1 s

Rtr = Vto^2/.15/32.17;          % transition radius
Ttr = etap*hp*550/Vto;
Dtr = (Cd0TO+K*Clto^2)*qto*S;
thetaCL = asin((Ttr-Dtr)/TOGW);
Str = Rtr*sin(thetaCL);
htr = Rtr*(1-cos(thetaCL));
if htr > 50
   SCL = 0;                     % climb distance for 50' obstacle
   gamma50 = acos(1-50/Rtr);
   Str = Rtr*sin(gamma50);
else
   SCL = (50-htr)/tan(thetaCL); % climb distance for 50' obstacle
end

Sg = Sngr+Sr;                   % takeoff groundrun
Sto = Sngr+Sr+Str+SCL;          % total takeoff distance
```

7. Landing Distance Calculation

```
% Program landing.m
% [Sl,Slg]=landing(Wland,S,Clmax,Clgr,Cd0land,rho,K)

% Written by: Nanyaporn Intaratep
% Last updated: 10-28-01

% Description:
% This program is a function to define landing distance for ground roll
% and clear 50' obstacle. The calculation based on no-ground-effect and
% no thrust assumption.

% References:
% Roskam, Jan and Lan, Chuan-Tau Edward, Airplane Aerodynamics and
%   Performance, 1997, Section 10.6.3

% INPUT

%   Wland          landing weight, lbs
%   S              wing area, ft^2
%   Clmaxland      landing lift coefficient
%   Clgr           Cl at setting angle
%   Cd0land        landing drag coefficient
%   rho            air density, slug/ft^3
%   K              induce drag factor

% OUTPUT

%   Slg,           Landing ground roll distance, estimated, ft
%   Sl,            Landing & clear 50' distance, estimated, ft
```

```
function[Sl,Slg]=landing(Wland,S,Clmaxland,Clgr,Cd0land,rho,K)

Vsl = (2*Wland/S/rho/Clmaxland)^0.5; % stall speed for landing configuration
Va = 1.3*Vsl;                % approch speed
Ta = 0;                      % thrust at approaching speed is neglect
Cla = Clmaxland/1.69;
Cda = Cd0land+K*Cla^2;
gamma_a = asin(-Ta/Wland+Cda/Cla);
Vfl = 0.95*Va;
nfl = 1.08;                  % steep angle
Rfl = Vfl^2/32.17/(nfl-1);
Sla = 50/tan(gamma_a) + Rfl*gamma_a/2;    % landing air distance
Vtd = 1.15*Vsl;
Slr = Vtd;                   % rotation distance
mue_b = 0.4;
mue = 0.025;
NW = 0.08;                   % ratio of nose-wheel friction and weight
Ttd = 0;
qtd = rho*Vtd^2/2;
Cdgr = Cd0land+K*Clgr^2;
Cd_Cl = Cdgr-mue_b*Clgr;
Slngr = (Wland/S/32.17/rho/Cd_Cl)*log(1+Vtd^2*rho*Cd_Cl*S/2/Wland/(mue_b-
Ttd/Wland-NW*(mue_b-mue)));
Sl = Sla+Slr+Slngr;          % total landing distance
Slg = Slr+Slngr;
```

8. Minimum Power Required Conditions

```
% Program minpwr.m
% [Clmp, Cdmp, LDmp, Vmp] = minpwr(Cd0,TOGW,rho,S,K)

% Written by: BER SIDELL
% Last updated: 9-28-01

% Description:
% This program is a function to define data at minimum power require

% References:
% Jan Roskam, AIRPLANE DESIGN, PART 1: PRELIMINARY SIZING OF
AIRPLANES, 1997
% Section 3.4.4.1

% INPUT

%   Cd0,            zero lift drag coefficient
%   TOGW,           aircraft weight, lbs
%   rho,            air density, slug/ft^3
%   S,              wing area, ft^2
%   K,              induced drag factor

% OUTPUT

%   Clmp,           lift coefficient at minimum power
%   Cdmp,           drag coefficient at minimum power
%   LDmp,           lift to drag ratio for minimum power
%   Vmp,            velocity at minimum power, mph




function [Clmp, Cdmp, LDmp, Vmp] = minpwr(Cd0,TOGW,rho,S,K)

Clmp = sqrt(3*Cd0/K);

Cdmp = 4*Cd0;

LDmp = Clmp/Cdmp;

Vmp = sqrt((2*TOGW)/(rho*S)*sqrt(K/(3*Cd0)))*0.68;      % mph
```

9. Maximum Rate of Climb Calculation

```
% Program RClimb.m
% [RoC,RCP] = RClimb(etap,WoP,WoS,Cl,Cd,sigma)

%Written by: BER SIDELL
%Last updated: 9-28-01

% Description:
% This program is a function to define rate of climb at different altitude

% References:
% Jan Roskam, AIRPLANE DESIGN, PART 1: PRELIMINARY SIZING OF
AIRPLANES, 1997
% Section 3.4.4.1

%INPUT

%   etap,       prop efficiency
%   WoP,        weight/HP, power loading, lb/hp
%   WoS,        weight/S, wing loading, lb/ft^2
%   Clmp,       lift coefficient
%   Cd,         drag coefficient
%   sigma,       air density ratio

%OUTPUT

%   RoC,        Rate of Climb in fpm
%   RCP,        Rate of climb parameter


%VERIFICATION
%correct when compared to hand calculation


function [RoC,RCP] = RClimb(etap,WoP,WoS,Cl,Cd,sigma)

RCP = (etap*sigma/WoP) - (sqrt(WoS)/(19*(Cl^1.5/Cd)*sqrt(sigma)));    %hp/lbs

RoC = 33000*RCP;                    % fpm
```

10. Maximum Cruise Speed Calculation

```
% Program maxcruise.m
% [Vc] = maxcruise(hp,etap,rho,S,Cd0,TOGW,K)

% Written by NANYAPORN INTARATEP
% Last updated: 9-27-01

% Description:
% This program is a function to define maximum cruise speed at 80% power from
% the point at power require equals power available.

% Reference:
% John D. Anderson, Jr., Introduction to flight, 3rd edition, 1989
% Equation 6.28

% INPUT

%   hp              maximum engine horse power, hp
%   etap            propeller efficiency
%   rho             air density at altitude, slug/ft^3
%   S               wing area, ft^2
%   Cd0             zero lift drag coefficient
%   TOGW            take off gross weight, lbs
%   K                induce drag coefficient

% OUTPUT

%   Vc          maximum cruise speed at 80% power, mph
```

```
function[Vc] = maxcruise(hp,etap,rho,S,Cd0,TOGW,K)

% Estimate power available at 80% and cruise altitude

Pa80 = hp*etap*550*0.8*rho/.002377;              %lb-ft/s



% Solve for maximum cruise speed when power require equals power available
% Pa80=(rho*(Vcmax^3)*S*Cd0/2)+(TOGW^2/(rho*Vcmax*S/2)*K)
% Find root of polynomial equation

coeff = [rho*S*Cd0/2 0 0 -Pa80 2*TOGW^2/rho/S*K];
Vcmax = roots(coeff);                            %ft/s
Vcmax = numeric(Vcmax);

% Pick positive real number for an answer of maximum cruise speed

Vc = 0;
for q=1:length(Vcmax),
    if (isreal(Vcmax(q))==1)&(Vcmax(q)>0)&(Vcmax(q)>Vc)
      Vc=Vcmax(q);
    end;
end;

Vc = Vc*0.68;                    %mph
```

11. Service and Absolute Ceiling Calculation

```
% Program ceiling.m
% [rho, Alt]=ceiling(RoC,etap,WoS,WoP,Cl,Cd)

% Written by Nanyaporn Intaratep
% last update 09-28-01

% Description:
% This program is a function to define absolute and service ceiling from
% maximum rate of climb equation.

% References:
% Jan Roskam, AIRPLANE DESIGN, PART 1: PRELIMINARY SIZING OF
AIRPLANES, 1997
% ection 3.4.4.1

% INPUT

%   RoC,        required rate of climb, fpm
%   WoS,        wing loading, lb/ft^2
%   WoP,        power loading, lb/hp
%   Cl,         life coefficient
%   Cd,         drag coefficient
%   etap,       propeller efficiency

% OUTPUT

%   rho,        air density, slub/ft^3
%   Alt,        altitude, ft
```

```
function [rho, Alt]=ceiling(RoC,etap,WoS,WoP,Cl,Cd)

X = sqrt(WoS);
Y = Cl^1.5;

% Solve for ceiling by setting equation in term of cubic polynomial equation
% RoC = 33000*((etap*sigma/WoP) - (X/(19*(Y/Cd)*sqrt(sigma))))
% Find root of polynomial equation


coeff =[33000*etap/WoP 0 -RoC -33000*(X/(19*(Y/Cd)))];

sigma12 = roots(coeff);                %sigma12=sqrt(sigma)

% Pick positive real number for an answer of sigma12

sigma = 0;
for q=1:length(sigma12),
    if (isreal(sigma12(q))==1)&(sigma12(q)>0)&(sigma12(q)>sigma)
      sigma=sigma12(q)^2;
    end;
end;

% Calculate air density by multiplying with air density at sea level

rho = sigma*0.002378;
[Alt] = rhoatm(rho);
```

1.2 Corresponding Altitude Calculation from Air Density

```
% program rhoatm.m
% [Alt] = rhoatm(rho)

% Written by Nanyaporn Intaratep
% last update 10-07-01

% Description:
% This program is a function to define corresponding altitude from air density

% Reference:
% Based on the 1976 standard atmosphere
% Altitude(km)      Temperature(K)     Lapse rate(K/km)
%    0-11           288.15-216.65          -6.5
%   11-20              216.55                0
%   20-32           216.65-228.65            1
%   32-47           228.65-270.65           2.8
%   47-51              270.65              0
%   51-71           270.65-214.65          -2.8

% INPUT

% rho          air density, slug/ft^3

% OUTPUT

% Alt          altitude, ft


function[Alt] = rhoatm(rho)
```

```
K = 34.163195;                % K = gravity(g)/Gas Constant(R)
rho = rho*515.3788;           % changing to SI unit, kg/m^3

if (rho >= 0.36392) & (rho < 1.225)          % Altitude 0-11,000 m

   a = -6.5;
   Tb = 288.15;
   rhob = 1.225;
   Hb = 0;
   T = Tb * (rho/rhob)^(-(1/(K/a+1)));
   H = Hb + (T-Tb)/(a*10^-3);
   Alt = H / (1-H/6356766);

elseif (rho >= 1.225) & (rho < 1.2251)       % sea level

   Alt = 0;

elseif (rho >= .08805) & (rho < .36392)      % Altitude 11,000-20,000 m

   Tb = 216.65;
   rhob = 0.36392;
   Hb = 11000;
   H = Hb - Tb/K*log(rho/rhob);
   Alt = H / (1-H/6356766);

elseif (rho >= .01323) & (rho < .08805)      % Altitude 20,000-32,000 m

   a = 1;
   Tb = 216.65;
   rhob = .08805;
```

```
    Hb = 20000;
    T = Tb * (rho/rhob)^(-(1/(K/a+1)));
    H = Hb + (T-Tb)/(a*10^-3);
    Alt = H / (1-H/6356766);

elseif (rho >= .00143) & (rho < .01323)        % Altitude 32,000-47,000 m

    a = 2.8;
    Tb = 228.65;
    rhob = .01323;
    Hb = 32000;
    T = Tb * (rho/rhob)^(-(1/(K/a+1)));
    H = Hb + (T-Tb)/(a*10^-3);
    Alt = H / (1-H/6356766);

elseif (rho >= .00086) & (rho < .00143)        % Altitude 47,000-51,000 m

    Tb = 270.65;
    rhob = 0.00143;
    Hb = 47000;
    H = Hb - Tb/K*log(rho/rhob);
    Alt = H / (1-H/6356766);

elseif (rho >= .00006) & (rho < .00086)        % Altitude 51,000-71,000 m

    a = -2.8;
    Tb = 270.65;
    rhob = .00086;
    Hb = 51000;
    T = Tb * (rho/rhob)^(-(1/(K/a+1)));
    H = Hb + (T-Tb)/(a*10^-3);
```

```
    Alt = H / (1-H/6356766);

elseif (rho >= .0000065) & (rho < .00006)       % Altitude 71,000-84,852 m

    a = -2;
    Tb = 214.65;
    rhob = .00006;
    Hb = 71000;
    T = Tb * (rho/rhob)^(-(1/(K/a+1)));
    H = Hb + (T-Tb)/(a*10^-3);
    Alt = H / (1-H/6356766);

else

    Alt ='Out of table, can not find the altitude';

end

if ischar(Alt) ==  0
    Alt = Alt*3.2808;                   % changing back to English unit, ft
end
```

1.3 Corresponding Altitude Calculation from Air Density

```
% Program stdprop.m
% [T, P, rho, A, MU, TS, RR, PP, RM, QM, getanswer]=stdprop(z,unit)

% Written by Nanyaporn Intaratep
% last update 10-07-01

% Description:
% This program is a function to define standard atmosphere properties

% References:
% W.H. MASON, BASIC AERODYNAMIC RELATION, in FORTRAN version, 1989



function[T, P, rho, A, MU, TS, RR, PP, RM, QM, getanswer]=stdprop(z,unit)

K = 34.163195;                  % K=g/R
getanswer = 1;

% unit = 0 metric units, otherwise english units

if unit==0
   TL = 288.15;
   PL = 101325;
   RL = 1.225;
   C1 = 0.001;
   AL = 340.294;
   ML = 1.7894e-5;
   BT = 1.458e-6;
```

```
else
    TL = 518.67;
    PL = 2116.22;
    RL = 0.0023769;
    C1 = 3.048e-4;
    AL = 1116.45;
    ML = 3.7373e-7;
    BT = 3.0450963e-8;
end

H = C1*z/(1+C1*z/6356.766);

if H < 11

    T = 288.15 - 6.5 * H;
    PP = (288.15/T)^(-K/6.5);

elseif (H >= 11) & (H < 20)

    T = 216.65;
    PP = 0.22336 * exp(-K*(H-11)/216.65);

elseif (H >= 20) & (H < 32)

    T = 216.65 + (H-20);
    PP = 0.054032 * (216.65/T)^K;

elseif (H >= 32) & (H < 47)

    T = 228.65 + 2.8 * (H-32);
    PP = 0.0085666 * (228.65/T)^(K/2.8);
```

```
elseif (H >= 47) & (H < 51)

    T = 270.65;
    PP = 0.0010945 * exp(-K*(H-47)/270.65);

elseif (H >= 51) & (H < 71)

    T = 270.65 - 2.8 * (H - 51);
    PP = 0.00066063 * (270.65/T)^(-K/2.8);

elseif (H >= 71) & (H < 84.852)

    T = 214.65 - 2 * (H-71);
    PP = 3.9046e-5 * (214.65/T)^(-K/2);

else

    getanswer = 0;
    RR = 0;
    PP = 0;
    MU = 0;
    TS = 0;
    A = 0;
    T = 0;
    rho = 0;
    P = 0;
    RM = 0;
    QM = 0;

end
```

```
if getanswer

    RR = PP/ (T/288.15);
    MU = BT * T^1.5 / (T+110.4);
    TS = T/288.15;
    A = AL * sqrt(TS);
    T = TL * TS;
    rho = RL * RR;
    P = PL * PP;
    RM = rho * A / MU;
    QM = 0.7 * P;

end
```

14. Stall Speed Corresponding to Cl_{max}

```
% Program Vel.m
% [V] = Vel(TOGW,rho,S,Cl)

% Written by Nanyaporn Intaratep
% last update 09-28-01

% Description:
% This program is a function to define stall speed at different conditions.
% Calculate velocity for level flight using lift coefficient.

% Reference:
% John D. Anderson, Jr., Introduction to flight, 3rd edition, 1989
% Equation 5.56

% INPUT

%   TOGW,    takeoff gross weight, lbs
%   rho,     air density, slug/ft^3
%   S,       wing area, ft^2
%   Cl,      lift coefficient at desired position

% OUTPUT

%   V,       velocity coresponding to Cl, mph


function[V] = Vel(TOGW,rho,S,Cl)

V=sqrt(2*TOGW)/sqrt(rho*S*Cl)*0.68;       %mph
```

Vita: Nanyaporn Intaratep

EDUCATION: **MS. Aerospace Engineering,** June 2002
Thesis: The Investigation of an Inboard-Winglet Applicaiont to a Roadable Aircraft
Virginia Tech, Blacksburg VA
GPA: 3.38/4.00
BS. Aerospace Engineering, March 1998
Kasetsart University, Bangkok, Thailand
GPA (in major): 3.11/4.00

EXPERIENCES: **Graduate Teaching Assistant**
Aerospace and Ocean Engineering Department, Virginia Tech, Blacksburg VA
August 2000 – Present

- Instructor in an undergraduate laboratory course, AOE3045 experimental methods

Lecturer
Department of Aerospace Engineering, College of Engineering, Kasetsart University, Bangkok, Thailand
June 1999 – August 2000

- Co-lecturer in undergraduate courses
- Analyzed and drafted the master plan of aircraft utilization, procurement and maintenance for Aviation Division, Bureau of Royal Rain Making and Agricultural Aviation, Ministry of Agriculture and Cooperatives with the departmental team
- Research assistant on a project, Visualization Techniques for Architectural study of Air Flow in The 60's Building

Design Engineer
Research and Development Institute of Industrial Production Technology, Kasetsart University, Bangkok, Thailand
December 1998 – May 1999

- Designed and developed commercial products by using Pro/ENGINEER and COSMOS/M
- Analyzed and evaluated the procedure of plastic injection

International Internship
Khujand, Republic of Tajikistan
Organized by International Association for Exchange of Student for Technical Experience (IAESTE)
August – October 1998

- Observed industries related to vodka, automobiles and bicycles

Summer Practical Training
Institute of Aeronautics and Astronautics (IAA), National Cheng Kung University (NCKU), Tainan, Taiwan, R.O.C.
April – June 1997

- Researched in a project, Visualization Study of High Angle of Attack Airfoil under Periodic Flapping Excitation

PUBLICATIONS:

Intaratep, N., *The Investigation of an Inboard-Winglet Application to a Roadable Aircraft, Master thesis*, Virginia Tech, May 2002

Marchman, J. F., III, Intaratep, N., Skelton, C. E., and Mason, W. H., *An Investigation of CTOL Dual-Mode PAVE Concepts*, NASA grant NAG-1-01100, January 2002

Chedchaiyapom, N., Intaratep, N. and Thipyopas, C., *2-D Analysis of Aerodynamic Loads on a Large-Roof Structure*, Senior project, Kasetsart University, Febuary 1998

COMPUTER SKILLS:

MATLAB	Mathcad	QBASIC
MATHEMATICA	COSMOS/M	ANSYS
Pro/ENGINEER	AutoCAD	Ms Office

ACTIVITIES:

TKD club member, Virginia Tech

Vice-president of TSA (2001-2002), Virginia Tech

Editor and treasurer of AeroClub Magazine (1996-1997), Kasetsart Univeristy

Vice-president of freshman engineering student committee (1994-1995), Kasetsart University